INAUGURAL - DISSERTATION
zur
Erlangung der Doktorwürde
der
Naturwissenschaftlich - Mathematischen
Gesamtfakultät
der Ruprecht-Karls-Universität
Heidelberg

Vorgelegt von
Dipl.-Phys. Aram Giahi Saravani
aus Gronau (Westf.)

Statistical de-lensing of galaxy ellipticities

Gutachter: Prof. Dr. Björn Malte Schäfer, Heidelberg
Prof. Dr. Eva Grebel, Heidelberg
Tag der mündlichen Prüfung: 26. Juli 2013

meinen Eltern

Choose Something Like a Star

O Star (the fairest one in sight),
We grant your loftiness the right
To some obscurity of cloud –
It will not do to say of night,
Since dark is what brings out your light.
Some mystery becomes the proud.
But to be wholly taciturn
In your reserve is not allowed.

Say something to us we can learn
By heart and when alone repeat.
Say something! And it says 'I burn.'
But say with what degree of heat.
Talk Fahrenheit, talk Centigrade.
Use language we can comprehend.
Tell us what elements you blend.

It gives us strangely little aid,
But does tell something in the end.
And steadfast as Keats' Eremite,
Not even stooping from its sphere,
It asks a little of us here.
It asks of us a certain height,
So when at times the mob is swayed
To carry praise or blame too far,
We may choose something like a star
To stay our minds on and be staid.

Robert Frost

Statistical de-lensing of galaxy ellipticities

Zunächst wird der Einfluss des Gravitationslinseneffektes auf statistische Eigenschaften von Galaxienelliptizitäten untersucht. Ausgehend von der Euclid Mission weisen Elliptizitätskorrelationen Veränderungen bei Multipolen von $\ell \gtrsim 1000$ auf, um $\sim 5\%$ bei E-Moden und um $\sim 30\%$ bei B-Moden, wobei der Effekt bei kleineren Rotverschiebungen ausgeprägter ist. Die Konversion von E- und B-Moden conversion, sowie die Möglichkeit, Korrelationen zwischen unterschiedlichen Multipolen zu beobachten, wird untersucht. Auch wenn der Shear-Effekt überwiegt, ist der Verschiebungseffekt signifikant bei kleinen Winkelskalen, mit einer Reihe von interessanten und möglicherweise beobachtbaren Effekte für zukünftige Beobachtungen. Das zweite Thema diese Arbeit ist die zeitliche Entwicklung intrischer Korrelationen von Galaxienelliptizitäten durch die Eigenbewegung der Galaxien. Die Größenordung und die charakteristische Skala des Einflusses von Pekuliarbewegungen wird im Zusammenhang mit der Euclid Mission untersucht. Korrelationen sind vermindert bei Multipolen über $\ell \gtrsim 1000$, über 10 Prozent für das E- und 60 Prozent für das B-Modenspektrum für $\ell \gtrsim 3000$. Eine E/B-Moden Umwandlung ist vorhanden aber klein. Auf großen Skalen und kleinen Rotverschiebungen können diese Effekte möglicherweise beobachtet werden. Ein weiterer Aspekt dieser Arbeit betrifft den Modellvergleich im Rahmen nicht-Gaußscher Inflationsmodelle. p-Wert und Bayesische Methoden werden vor dem Hintergrund der Beobachtung von Dreipunktkorrelationen im Galaxienelliptizitätsfeld verglichen.

Statistische Rekonstruktion von Galaxienelliptizitäten

First, changes in galaxy ellipticity statistics induced by weak gravitational lensing are studied. Ellipticity correlations are altered by lensing deflection on multipoles $\ell \gtrsim 1000$ by $\sim 5\%$ for the ellipticity E-modes and by $\sim 30\%$ for the B-modes, while a shallower survey would exhibit larger changes. The E/B-mode conversion is analyzed, the possibility of measuring correlations between different multipoles, induced by homogeneity breaking, is discussed. Although correlations generated by weak gravitational shear dominate, the shifting effect is significant on small angular scales, causing a number of interesting phenomena possibly observable by future surveys.

Second subject of this work is the time evolution of intrinsic correlations of galaxy ellipticities due to peculiar galactic motion. The magnitude and scale on which peculiar motions affect the ellipticity correlation is studied. Correlations are decreased on large multipoles $\ell \gtrsim 1000$, up to 10 per cent in the E-mode and up to 60 per cent in the B-mode spectrum at $\ell \gtrsim 3000$. E/B-mode conversion is present but small. Observational significance is concluded for larger scales for surveys at lower redshifts.

Another aspect of weak lensing statistics is explored in the context of Bayesian model comparison. Frequentist and Bayesian statistics are contrasted in the context of inflationary non-Gaussianity models.

Contents

1. Abstract

Statistical de-lensing of galaxy ellipticities

With future weak lensing surveys entering new levels of precision, understanding the implications of potential sources of contaminations and observable physical phenomena is of both practical and theoretical importance. The focus of this work is on the statistics of galaxy ellipticity correlators in the context of two distinct physical processes, weak gravitational lensing and peculiar motions of galaxies, with a supplementary study of inflationary non-Gaussianities.

Both weak graviational lensing and peculiar motions of galaxies have interesting implications on ellipticity statistics such as homogeneity breaking and gradient/curl (E/B)-mode mixing and are shown to be significant on small scales (high multipoles). Analytical methods from the cosmic microwave background (CMB) polarization formalism are applied on the basis of analogies between CMB polarization and spin-2 ellipticity fields. The final part of this thesis comprises an instructive comparison of Bayesian and Frequentist statistics in the framework of non-Gaussian inflationary model selection for which the parameter dependence of the respective models is linear. The statistical estimator applied for model selection is provided by the convergence bispectrum, which is the Fourier space analogue of the three-point correlation function in real space.

First, changes in measured galaxy ellipticity statistics induced by weak gravitational lensing are studied. Starting with a derivation of intrinsic ellipticity spectra by employing a tidal shearing model for the fluctuation statistics of galactic angular momenta galaxy ellipticities are modelled by assuming that the galactic disk forms perpendicularly to the host halo angular momentum direction. For EUCLID, ellipticity correlations are altered by lensing deflection on multipoles $\ell \gtrsim 1000$ by $\sim 5\%$ for the ellipticity E-modes and by $\sim 30\%$ for the B-modes, while a shallower survey would exhibit larger changes. In addition to the convolving effect of lensing on the ellipticity spectra the E/B-mode conversion is analyzed, and possibility of measuring correlations between different multipoles are discussed which is evoked by the homogeneity breaking effect of the lensing displacement. Although shape correlations generated by weak gravitational shear are dominant, the shifting effect due to lensing is shown to shape the ellipticity spectra on small angular scales and to cause a number of interesting phenomena which may be observable by future surveys.

The second subject addressed in this thesis is the time evolution of intrinsic correlations of galaxy ellipticities due to peculiar galactic motion. Analogies between the lensing potential in weak gravitational lensing and the displacement potential are explored in Lagrangian Perturbation Theory (LPT). The order of magnitude and the length-scales on which peculiar motions affect the ellipticity spectrum is explored. A model is used in which the galaxy ellipticities are determined from the angular momentum of their host haloes, which can be computed from the fluctuation statistics of a Gaussian random field. Subsequent peculiar motion distorts the ellipticity field and causes changes in the ellipticity correlations. Employing analogies between this problem of

shifted ellipticity tensors and the displacements of polarization tensors in gravitational lensing of the cosmic microwave background (CMB) the E-mode and B-mode spectra of the time-evolved ellipticity field are computed, where the displacements are modelled with first- and second-order Lagrangian perturbation theory. For EUCLID, ellipticity correlations are decreased on large multipoles $\ell \gtrsim 1000$, amounting to up to 10 per cent in the E-mode spectrum $C_E^\epsilon(\ell)$ and up to 60 per cent in the B-mode spectrum $C_B^\epsilon(\ell)$ at $\ell \gtrsim 3000$ due to the dispersing effect of peculiar motion. E/B-mode conversion in analogy to CMB lensing is present but small. The conclusion is derived that distortions of the ellipticity field due to peculiar motion do not affect the prediction of ellipticity models on the scales relevant for lensing in the case of EUCLID's galaxy distribution, but should affect larger scales for surveys at lower redshifts.

Another aspect of weak lensing statistics is explored in the context of Bayesian model comparison. Bayesian and p-value statistics are introduced for the comparison of inflationary non-Gaussianity models on the basis of future weak cosmic shear data (e.g. EUCLID). Calculations are performed for theoretical and experimental priors and qualitative and quantitative differences between Bayesian evidence and the p-value results are investigated. The potential of lensing tomography for model comparison of bispectrum configurations is discussed in the context of the predictive power of future surveys. Significant differences in the results between the Bayesian and Frequentist formalism are observed, as predicted by the Lindley paradoxon. In the light of non-tomographic weak lensing bispectra preference is always given to the local non-Gaussianity model, caused by its comparetively small prior volume arising from the specific normalization for f_{NL}. The observe the importance of Bayesian model comparison as a complementary view on model selection is observed and an estimate is given of the impact on model selection with more conclusive data that may be obtained by more sophisticated observational methods, such as weak lensing tomography. Since most of the calculations in this paper are analytical, this work provides an intuitive and instructive view on Bayesian methods for this class of models with linear parameter dependency.

2. Introduction and motivation

Cosmology, as a subject of the natural sciences, is a comparatively young discipline which emerged in the 20th century from a study of world models according to Einstein's general theory of relativity to an active field of observations with implications for fundamental questions of modern physics. Central problems of modern cosmology address the nature of dark matter and dark energy, their role in cosmic structure formation and the evolution of complex structures such as galaxies. Developments in experimental technologies yield increasingly precise data from cosmic phenomena such as the cosmic microwave background (CMB), supernovae, cosmic structure, weak gravitational lensing, and the expansion of the Universe, which are deeply connected to fundamental theoretical aspects of physics and provide constraints on the multitude of model universes. The standard model of cosmology aims at explaining the multitude of observational findings, such as Hubble's discovery of an expanding space, the CMB, and the large scale structure of the Universe. The cosmological principle which rules out any preferred position in space, and a dynamical space, allowing for an early state of the Universe densities and temperatures much higher than today, constitute the basis of the standard model. In this framework the CMB originates from the recombination of electrons and protons 400000 years after the Big Bang when the universe became transparent due to adiabatic cooling, allowing the formation of neutral hydrogen atoms and subsequently the decoupling of photons and electrons. The radiation from that epoch which reaches us today at redshift $z \sim 1100$ resembles a black body of a Temperature of 2.73 K with anisotropies only of the order of 10^{-5} first observed with the COBE satellite (Smoot 1999). The CMB radiation carries information about the seeds of cosmic structures and the physical state of the early Universe and has thus become an important subject of current research. Recent observations of type Ia supernovae extend the picture of an expanding space by cosmic acceleration. This discovery revived interest in the cosmological constant Λ, first introduced by Einstein as an extension to the dynamical field equations of his General theory of Relativity in order to support the model of a static Universe (steady state model). The cosmological constant, however, also supports an accelerated expansion of space, and, in addition to a homogeneous, isotropic dynamic metric leads to the widely accepted ΛCDM model. Other models introduce dark energy as a generalization which comprise the cosmological constant which represents the vacuum energy in space with negative pressure. The nature of dark energy remains still a mystery to modern cosmology which is particularly striking since it constitutes about 68% of the Universe (Ade et al. 2013). The equation of state of dark energy determines the expansion rate of the Universe and is subject of active research in cosmology. Alternative models to dark energy aim at explaining the accelerated cosmic expansion by modified laws of gravity. The observed large scale structure of the universe, the gravitational deflection of light, and the dynamics of galaxies is in conflict with small fraction of visible baryonic matter and highly isotropic CMB, which led to the postulation of another yet unknown form of matter which interacts only by gravity and is thus referred to as dark matter. The only gravitationally interacting dark matter allowed it to decouple from the thermal equilibrium of cosmic

plasma earlier than ordinary matter, enabling the early growth of initial density perturbations to the extent of the structures observed today. By nature, dark matter is only observable indirectly by gravitational interaction. Recent observations by the Planck mission indicate a dark matter density in the Universe of 26.8%, by far exceeding the fraction of ordinary baryonic matter of 4.9% (Ade et al. 2013). The observed thermal equilibrium between distant regions of the Universe, which would usually not be causally connected, motivated the postulation of an early epoch, known as inflation, of extremely rapid exponential cosmic expansion. Inflation explains important observations, such as the large scale structure of the Universe, the vanishing curvature of space, and the absence of magnetic monopoles. In form of the ΛCDM model, the standard model thus comprises the four cosmological fluids radiation, dark matter, baryonic matter, and dark energy. The individual density of these fluids changed throughout the evolution of the Universe, from an early radiation dominated epoch to the matter and dark energy driven Universe today.

Important insights into the evolution of the Universe have been obtained by the observation of the CMB and the distribution and dynamics of galaxies. Due to its simple geometrical relation to the gravitational fields induced both by the baryonic and dark matter distribution along the trajectory of observed photons, weak gravitational lensing has become a powerful tool in cosmology. As surveys such as Euclid and Planck are becoming increasingly precise, potential sources of systematics in weak lensing surveys are of growing importance and will be addressed in this thesis. Weak gravitational lensing provides information on small angular scales and often complements other cosmological observational methods. This motivated the application of weak gravitational lensing, in this work, to cosmological problems which are significant on small angular scales.

This work studies the influence of peculiar motions of galaxies and weak gravitational lensing on the statistics of lensed galaxy ellipticities and the applicability of weak gravitational lensing in inflationary non-Gaussianity model selection. The cosmological observable used throughout this thesis are the observed ellipticities of a galaxies. Because the symmetry axis of the galactic disc is related to the angular momentum direction of the host halo, correlated angular momenta give rise to correlated angles of inclination and hence correlated ellipticities (Heavens et al. 2000, Crittenden et al. 2001, 2002, Mackey et al. 2002, Heymans & Heavens 2003). However, the way in which the orientation of a galactic disc is linked to the angular momentum direction of the host halo is not very clearly cut. Furthermore, the observed ellipticities carry information about the intervening matter distribution between observer and galaxies through the gravitational deflection of light. According to Einstein's theory of General Relativity the deflection of light depends on the total matter distribution between source and observer, given by the sum of dark and baryonic matter in the non-relativistic case, regardless of its physical state. Inhomogeneous gravitational fields between observer and galaxy cause magnification and distortion of the galaxy ellipticity field. Due to its complete characterization by the total matter density, the deflection of light provides an unbiased tracer of the intervening total matter distribution, making this effect a useful tool in uncovering the structure and evolution of dark matter in the universe. In the framework of weak gravitational lensing these effects are statistical in nature (in the per cent regime) and generally observed in terms of ellipticity correlations between an ensemble of galaxies.

Correlations functions and their corresponding spectra in Fourier space are a powerful tool in cosmology since they enable, for instance, the detection of the subtle changes in observed

4

galaxy ellipticities as induced by weak gravitational lensing. These changes are only significant in observations of sufficiently large ensembles of galaxies and contain information about the evolution of structures in the Universe. By assuming uncorrelated intrinsic ellipticities, observed correlations in ellipticities are explained by common gravitational fields between observer and galaxies. However, intrinsic alignments of galaxies are neglected by assuming random ellipticity orientations. As will be discussed in the following, this approximation does not necessarily hold for neighbouring galaxies which emanated from a similar physical environment during their formation process. With the advent of high-precision measurements such as Euclid, intrinsic ellipticity correlations may well be within the scope of future observations. Hence, a thorough understanding of observed ellipticity correlations is required in order to disentangle contributions of intrinsic alignments from the lensing signal. The cosmological background relevant for this work is described in Chapter 3. Principles of the weak gravitational lensing formalism and Bayesian and frequentist statistics are introduced in Chapters 4 and 5. The physical processes that introduce systematics to cosmic shear measurements and which are addressed in this thesis also offer an interesting theme for future observations. Mathematical analogies between the formalism of weak gravitational lensing and the problem of peculiar motions of galaxies are explored, the relevant length scales are discussed. Statistical effects such as homogeneity-breaking and characteristic signatures in the ellipticity spectrum are investigated. Furthermore, higher order statistics of lensed ellipticity fields are studied in order to assess the constraining power of weak gravitational lensing on inflationary non-Gaussianity models in the context of Bayesian model selection.

The accuracy of today's observations of cosmic shear is limited by systematics such as the approximation of intrinsically uncorrelated galaxies in weak gravitational lensing surveys. This motivated the development of methods and techniques aiming to correct for these errors. The assumption of intrinsically uncorrelated galaxy ellipticities yields a reasonable approximation for sufficiently large separations between galaxies. It is not likely to be applicable, however, for neighbouring galaxies which have been subject to similar tidal gravitational fields during their formation process. Numerous models of galaxy formation thus predict non-vanishing intrinsic ellipticity correlations due to the influence of tidal gravitational fields on the dynamics of the collapsing host halo from which the galaxies originate. By now, intrinsic alignments of spiral galaxies have been measured in a number of data sets and have been found at the expected levels (Pen et al. 2000, Lee & Pen 2002, Mandelbaum et al. 2006, Hirata et al. 2007), although some studies doubt these claims (e.g. Andrae & Jahnke 2011, Mandelbaum et al. 2011). Observed ellipticity correlations are rich in information since they are not only sensitive to cosmological parameters but also to intrinsic alignments of the angular momenta of galaxies. Intrinsic ellipticity correlations are interesting in their own right since they provide insight into galaxy formation and dynamics and may, due to their alignment, serve as a tracer to reconstruct the large-scale tidal fields (Lee & Pen 2000, 2001, 2007). The standard model of angular momentum generation, building on the ideas of Hoyle and Bondi, is the so-called tidal torquing theory (Peebles 1969, Doroshkevich 1970, White 1984). This theory identifies (laminar) shear flows that surround and deform the protogalactic object as the generator of angular momentum of the halos prior to collapse (for a review on angular momentum models and intrinsic alignments, see Schäfer 2009). Further differentiation of correlations between galaxies that are positioned in different halos and correlations between neighbouring galaxies located in the same halo give rise to a so-called two-halo term and one-halo term, respectively. Schneider & Bridle (2010) introduce a model

that distinguishes between contributions of central and satellite galaxies, where two-halo contributions are mainly due to central-central correlations, and one-halo contributions arise only by satellite-satellite correlations. One-halo terms support the intrinsic alignment power spectrum on small scales. These predictions of non-zero intrinsic ellipticity correlations due to angular momentum alignments of the host halos of neighbouring galaxies motivated the development of methods that would allow to disentangle intrinsic correlations from correlations induced by weak gravitational lensing. The most straightforward method discards close galaxy pairs with small redshift difference, thus removing the effect of the short correlation length of intrinsic alignments from the observed signal (King & Schneider 2002, Heymans & Heavens 2003, Heymans et al. 2004). Similarly ellipticity correlation can be measured within different redshift slices (King & Schneider 2003). A more mathematical approach transforms the observed power spectra with a weighting function in order to downweigh or amplify the contributions by intrinsic alignments (Joachimi & Schneider 2008, 2010). Another way to observe intrinsic alignments is given by expanding the ellipticity field in gradient (E) and curl (B) modes. Since weak gravitational lensing, unlike intrinsic alignments is curl-free to first order, observed $B-$modes can be attributed to intrinsic alignments (Crittenden et al. 2002). An additional source of correlations is caused by tidal gravitational fields of a dark matter halo radially aligning nearby galaxies while the weak shear acting on background galaxies is preferrentially tangential to the matter concentration. This produces a net anti-correlation, denoted by the so-called gravitational-intrinsic (GI) term, which will be neglected in the following since in its simplest form, there are no gravitational-intrinsic correlation expected for the kind of tidal shear model used in this thesis. For elliptical galaxies, however, the GI correlation can be much greater than the intrinsic-intrinsic (II) correlation for broad redshift distributions (Hirata & Seljak 2004). In this thesis, calculations of angular momentum correlations are based on a tidal torque model by Crittenden et al. (2001) which exhibits a quadratic dependence of galaxy ellipticities on angular momenta. These intrinsic correlations are predicted for the time of galaxy formation and serve as a basis to estimate the implications that arise by weak gravitational lensing and their evolution due to peculiar motions. These two processes are likely to induce changes on the shape of the ellipticity spectrum, which to reveal and characterize is the focus of this work.

The implications of weak gravitational lensing on observed galaxy ellipticities are the subject of Chapter 6. Gravitational light deflection is known to be a major source of ellipticity correlations and as such employed to trace the cosmic matter distribution. Intrinsic alignments of galaxies are predicted by tidal shear models which introduce angular momentum into haloes. If intrinsic ellipticity correlations are ignored systematic errors may arise from observations of neighbouring galaxies. Thus, as described above, several observational methods have been developed in order to separate weak lensing data from intrinsic alignments. As intrinsic correlations of galaxy ellipticities yield insight to the question of galaxy formation, understanding the characteristics of intrinsic ellipticity correlations caused by intrinsic alignments is desirable, especially in view of high precision observations such as Euclid. The significance of intrinsic alignments in weak lensing measurements has been predicted with a tidal torque model by Crittenden et al. (2001), who found that the intrinsic signal is between 1 to 10 per cent of the for the measured convergence power spectrum caused by weak gravitational shear for a deep reaching survey. By employing numerical simulations for three-point intrinsic ellipticity correlations (III) and the three-point coupling between the weak lensing shear experienced by distant galaxies and the shape of foreground galaxies (GGI and GII), Semboloni et al. (2008) find that on small scales

baryonic physics and intrinsic alignments can lead to a contamination of the bispectral data of about 15 per cent. These estimates show that for high precision measurements the imprint of intrinsic correlation cannot be ignored. For the observations of intrinsic ellipticity correlations these results indicate the possibility of finding characteristic signatures of intrinsic ellipticities in the weak lensing signal. Due to the short correlation length of intrinsic alignments of about 1 Mpc h^{-1}, changes induced to the observed lensing signal by intrinsic ellipticity correlations are expected to be significant at high multipole numbers. These estimates indicate that the influence of intrinsic correlations in future weak lensing surveys will not be negligible anymore. Hence, a qualitative and quantitative understanding of the contributions of intrinsic ellipticities will be highly desireable. The separation of the weak lensing from the intrinsic alignment signal allows for unbiased weak lensing surveys and the detection of intrinsic alignments by their characteristic imprint on the ellipticity spectrum. For this analysis of the ellipticity spectra, a formalism based on lensing of the cosmic microwave background (CMB) polarization is employed which distinguishes between gradient or E-modes and curl or B-modes (Seljak 1996a, Hu 2000, Challinor & Lewis 2005, Lewis & Challinor 2006). This coordinate basis independent representation is chosen because it reveals deeper insight into the symmetries of the ellipticity field. A suppression of ellipticity correlations is exptected due to the shifting effect of weak gravitational lensing, which dilutes and randomises the galaxy position at which ellipticities are measured.

Chapter 7 addresses the question by how much and on which scales peculiar motions of galaxies change the intrinsic ellipticity correlations. Peculiar motions cause displacements of galaxies relative to their initial positions at formation. This displacement can become comparable to the correlation length of intrinsic alignments, thus significantoly changing the intrinsic ellipticity correlations. The peculiar motion of galaxies is described in Lagrangian perturbation theory (LPT) which is applicable if the flow of dark matter and of the advected galaxies is irrotational and nonlinearities are weak. In this limit, galaxies follow straight lines given by the gradient of the Lagrangian potential Φ_1 to first order LPT (1LPT) (Doroshkevich 1970, Zel'Dovich 1970, Buchert 1989, Moutarde et al. 1991, Bernardeau et al. 2002). The Zeldovich approximation provides a link between the peculiar velocities and the gravitational potential field, allowing to describe the displacement effect in terms of a displacement potential, in analogy to weak lensing potential in the framework the weak gravitational lensing formalism. In contrast to the shifting effect of weak gravitational lensing which is increasing with redshift due to geometrical factors, (projected) displacements caused by peculiar motion are more pronounced for closeby galaxies. As in the case of weak gravitational lensing, ellipticity correlations are expected to be reduced by the diluting effect of the randomised peculiar motions of galaxies. In order to analyze characteristic signatures caused by peculiar motions, a formalism based on lensing of the cosmic microwave background polarization is employed. A model by Crittenden et al. (2001) with quadratic dependency of the ellipticity on the angular momentum serves as a basis for the initial intrinsic ellipticity correlation of an Euclid galaxy sample as an application, allowing a broader application to diverse galaxy morphologies. The analysis provided in this thesis of the evolution of intrinsic ellipticity correlations caused by peculiar motion provides predictions of the redshift-dependent signature of intrinsic ellipticities in weak lensing surveys.

In Chapter 8 inflationary non-Gaussianity models are analyzed in the context of Bayesian model selection. Higher order statistics of observed galaxy ellipticity fields such as bispectra are sensitive to non-Gaussian signatures and thus suited for the study of inflationary non-Gaussianities. Bayesian statistics witnesses a growing interest in cosmology and provides a

complementary perspective compared to frequentist inference. In Bayesian model comparison integrated likelihood-weighted prior probability ratios are assigned to the respective competing models. These ratios are usually interpreted on logarithmic scales such as Jeffrey's scale. Due to the inclusion of both prior and posterior probabilities Bayesian statistics can be viewed as mathematical realization of Occam's razor (Trotta 2008). Frequentist statistics, on the other hand, specifies an arbitrary significance level in chi-squared tests without taking into account the complexity a given model (Mukherjee et al. 2006). A manifestation of the fundamental differences between Bayesian and frequentist statistics is known as by Lindley's Paradox. An instructive application for comparing these two kinds of statistics are inflationary non-Gaussianity models with linear parameter dependence. The linearity of the models allows for analytical solutions for the Bayes factors. Bispectra for each type of inflationary non-Gaussinity model are calculated and employed in the Bayesian and frequentist model selection formalism. By focussing on weak lensing bispectra this work complements CMB studies on inflationary non-Gaussianities using the angular bispectrum of the CMB temperature anisotropy. Calculations include cosmic variance and shape noise but neglect systematical errors. In order to assess the full potential of weak lensing, calculations are performed in the framework of weak lensing tomography (Hu 1999), which is a method to increase the signal to noise ratio of the lensing signal. The results are compared to the priors from Komatsu et al. (2011) and conventional weak lensing, reflecting the constraining power of weak lensing tomography for inflationary non-Gaussianities from both the Bayesian and frequentist perspective.

Key results of this work are summarised and discussed in Chapter 9.

3. Cosmology

This chapter describes the geometrical and dynamical framework relevant for modern cosmology, the theory of cosmological structure formation, inflationary non-Gaussianities and their statistics in terms of correlation functions, and theories of tidal interactions and ellipticities.Sect. 3.1 introduces geometrical and dynamical aspects of space, the dynamical equations in cosmology are set in context to the Theory of General Relativity. Friedmann's equations are discussed as well as consequences of a dynamical metric, such as Hubble expansion and cosmological redshift. In Sect. 3.2 the theory of structure formation in cold dark matter models is discussed both for the linear and non-linear case and methods from Lagrangian perturbation theory are presented. Sect. 3.4 introduces statistical tools to analyse non-Gaussianities arising from inflation. Finally, Section 7.3 gives an overview of models for galaxy formation and ellipticities. Intrinsic ellipticity correlations induced by large scale tidal fields and their statistical properties are discussed.

3.1. Cosmological models

3.1.1. Geometry and dynamics of space-time

3.1.1.1. Geometry of space-time

The discovery that the speed of light is absolute in the sense that it does only depend on electric and magnetic properties of the vacuum and thus is the same in all frames of reference implies that the Newtonian-Galilean Principle of Relativity does not suffice to explain physical processes of electro-magnetic nature. Only a union of space and time would preserve invariance under coordinate transformations. Such a union is constituted within the framework of the so-called Minkowski space-time where Lorentz- instead of Galilei-transformations ensure invariance. The invariant line element is given by

$$\mathrm{d}s^2 = \eta_{\mu\nu}\mathrm{d}x^\mu\mathrm{d}x^\nu, \tag{3.1}$$

where the indices take on the values between 0 to 4 and the Einstein summation convention applies. $\eta_{\mu\nu}$ denotes the metric tensor and $\mathrm{d}x_\mu$ the time and space coordinates. This invariant line element is the foundation of any measure in space and time in cosmology where scales are in the relativistic regime.

Any physical study of the universe requires a metric that allows to define distances and constitutes, in the framework of Einstein's General Theory of Relativity, a foundation for deriving the dynamical equations that govern the evolution of the cosmos. To obtain a metric the cosmological principle is introduced, namely that space is spherically symmetric (isotropic) and invariant under translations (homogeneous). This is in accordance to the Copernican principle stating that there is no privileged point in space. In the general case of a dynamical (time-dependent) met-

ric the symmetries of isotropy and homogeneity, expressed in spherical coordinates, lead to the so-called Robertson-Walker metric:

$$ds^2 = c^2dt^2 - a^2(t)\left[d\chi^2 + f_K^2(\chi)\left(d\theta^2 + \sin^2\theta d\phi^2\right)\right], \tag{3.2}$$

where $f_K(\chi)$ depends on the Gaussian curvature K of space. The time-dependent scale factor $a(t)$ describes the time-evolution of the metric. This Robertson-Walker line element is a consequence of the symmetries imposed by the cosomological principle. These coordinates are comoving, they follow the mean motion of matter in accordance to a time-evolving metric. χ is thus denoted as comoving distance. The curvature dependence of f_K is as follows:

$$f_K(\chi) = \begin{cases} \frac{1}{\sqrt{K}}\sin\left(\sqrt{K}\chi\right) & , K > 0, \text{ spherical,} \\ \chi & , K = 0, \text{ flat,} \\ \frac{1}{\sqrt{|K|}}\sinh\left(\sqrt{|K|}\chi\right), & K < 0, \text{ hyperbolic.} \end{cases} \tag{3.3}$$

An alternative form of the Robertson-Walker line element is given by

$$ds^2 = c^2dt^2 - a^2(t)\left[\frac{d\chi^2}{1 - Kr^2} + r^2(\chi)\left(d\theta^2 + \sin^2\theta d\phi^2\right)\right], \tag{3.4}$$

where $r \equiv f_K(\chi)$.

3.1.1.2. Expansion of space and cosmological redshift

Since Hubble's observation that the galaxies are receding from us with velocities proportional to their distances by the Hubble constant $H_0 = h \cdot 100\,\text{km}\,\text{s}^{-1}\text{Mpc}^{-1}$, with $h = 0.55...0.85$, it is known that the Universe is expanding. In the framework of the Robertson-Walker metric this expansion is described by the scale function $a(t)$. As will be shown in the following, the metric allows us to make some kinematical deductions. For a comoving galaxy at a given (comoving) distance r the corresponding proper distance d_P at a cosmic time t is given by

$$d_P = a(t)\int_0^r \frac{dr'}{\sqrt{1 - Kr'}}. \tag{3.5}$$

The velocity of recession is then

$$v = \frac{dd_P}{dt} = \dot{a}(t)\int_0^r \frac{dr'}{\sqrt{1 - kr'}} = \frac{\dot{a}(t)}{a(t)}d_P, \tag{3.6}$$

which is Hubble's Law with a time-dependent Hubble function

$$H(t) = \frac{\dot{a}(t)}{a(t)}. \tag{3.7}$$

The Hubble Law is a consequence of the symmetry of a dynamical space.

An expanding space implies a redshift for light that propagates from the source to the observer. The shift in frequency can be determined by regarding the invariant line element $ds = 0$ for photons. Light emitted from a comoving source at time t_0 reaches a comoving observer at $\chi = 0$

at t_1. For the metric the condition $c \mathrm{d}t = a \mathrm{d}\chi$ will hold for the light ray. Since by definition the comoving coordinate distance is constant, for the (comoving) separation χ_{01} between source and observer one obtains:

$$\chi_{01} = \int_{\chi_1}^{\chi_0} \mathrm{d}\chi = \int_{t_0}^{t_1(t_0)} \frac{c \mathrm{d}t}{a(t)} = \text{const.}, \tag{3.8}$$

which implies

$$\frac{\mathrm{d}t_1}{a(t_1)} = \frac{\mathrm{d}t_0}{a(t_0)} \quad \text{or} \quad \frac{\mathrm{d}t_1}{\mathrm{d}t_0} = \frac{a(t_1)}{a(t_0)}. \tag{3.9}$$

Relating the time intervals with the light frequency ν and wavelength λ yields

$$\frac{a(t_1)}{a(t_0)} = \frac{\nu_0}{\nu_1} = \frac{\lambda_1}{\lambda_0} = 1 + z, \tag{3.10}$$

where the redshift z is defined as the relative change in wavelength,

$$1 + z \equiv \frac{\lambda_1}{\lambda_0}. \tag{3.11}$$

3.1.1.3. Dynamical equations

For a dynamical metric $g_{\mu\nu}$, such as the Robertson-Walker metric, the scale function $a(t)$ and curvature K are free functions yet to be determined. A framework which describes the dynamics of these functions is provided by the matter field equations of GRT which relate the dynamics and curvature of space-time to the energy-momentum tensor $T_{\mu\nu}$ (Landau & Lifshitz 1975):

$$R_{\mu\nu} - \frac{R}{2} g_{\mu\nu} \equiv G_{\mu\nu} = \frac{8\pi G}{c^4} T_{\mu\nu} + \Lambda g_{\mu\nu}, \quad \text{with} \quad T_{\mu\nu} = \left(\rho + \frac{p}{c^2} \right) \upsilon_\mu \upsilon_\nu - p g_{\mu\nu}, \tag{3.12}$$

where density ρ and pressure p completely characterize the ideal cosmological fluids with four velocity υ_μ in space-time, and Λ denotes the cosmological constant. The Einstein tensor $G_{\mu\nu}$ is constructed from the Ricci tensor $R_{\mu\nu}$ which contains second order derivatives of the metric tensor. This allows equation 3.12 to reduce to Poisson's equation in the classical Newtonian limit. In fact, Poisson's equation can be derived as a linear approximation from the matter field equations in the static weak field limit with a non-relativistic energy-momentum tensor under the assumption of an ideal adiabatic fluid.

3.1.1.4. Cosmological model for a perfect fluid in a Robertson-Walker space-time

A theoretical description of the time evolution of space is given by the dynamical solutions of GRT for the Robertson-Walker metric and an energy-momentum tensor describing a perfect fluid which is characterized by its density ρ and its pressure p. Solving the corresponding field equations yields Friedmann's equations (Friedmann 1922, 1924):

$$\frac{\dot{a}}{a} = \sqrt{\frac{8\pi G}{3} \rho - K \frac{c^2}{a^2} + \frac{\Lambda}{3}} \tag{3.13}$$

and

$$\frac{\ddot{a}}{a} = -\frac{4\pi G}{3} \left(\rho + \frac{3p}{c^2} \right) + \frac{\Lambda}{3}. \tag{3.14}$$

From these two equations model universes can be constructed from these equations. Examples are the dust model ($p = 0$), the radiation model ($\rho = 3p/c^2$), the static solution ($\rho = -3p/c^2$) which requires a cosmological constant, and the Einstein-de Sitter universe ($\rho = K = 0$). A cosmology with an expansion rate as a function of the scale function $a(t)$ governed by Friedmann's equations is called Friedmann-Lemaître-Robertson-Walker (FLRW) cosmology.

For a vanishing cosmological constant following conclusions can be drawn from these equations: Equation (3.13) implies that for $\Lambda > 0$ only the curvature term can cause the expansion to stop and it can be seen that K vanishes for the critical density

$$\rho_c = \frac{3H_0^2}{8\pi G} \approx 1.9 \times 10^{-29} h^2 g\,\mathrm{cm}^{-3}. \tag{3.15}$$

Furthermore, equation (3.14) requires that for $\Lambda = 0$ the acceleration of the Universe is always negative, which means that $\dot{a}$ is always decreasing in time. Thus, the Hubble time $t_0 = H_0^{-1}$ represents an upper limit to the age of the universe.

Both equations can be combined to yield the so-called adiabatic equation,

$$\frac{\mathrm{d}}{\mathrm{d}t}\left[a^3(t)\,c^2\,\rho(t)\right] + p(t)\frac{\mathrm{d}}{\mathrm{d}t}a^3(t) = 0, \tag{3.16}$$

which describes the time evolution of the energy content of a volume that is expanded by the isentropic Hubble flow. Thus, the adiabatic equation corresponds to the first law of thermodynamics with respect to cosmic expansion. The density ρ refers to the entire energy density in the universe and thus represents the sum of matter and radiation density, ρ_M and ρ_R respectively. In units of the critical density ρ_c following notation is common in cosmology:

$$\Omega_R = \frac{8\pi G p}{c^2 H_0^2}, \quad \Omega_m = \frac{\rho}{\rho_c}, \quad \Omega_\Lambda = \frac{\Lambda}{3H_0^2}, \quad \dots \tag{3.17}$$

Reference values according to Planck (Ade et al. 2013) are matter density $\Omega_m = 0.314 \pm 0.020$, baryonic density $\Omega_B = 0.02207 \pm 0.00033\, h^2$, and cosmological constant $\Omega_\Lambda = 0.686 \pm 0.020$. Applying these definitions to equation (3.13) yields

$$H^2(t) = H_0^2\left[\frac{\Omega_R}{a^4(t)} + \frac{\Omega_m}{a^3(t)} - \frac{K(c/H_0)^2}{a^2(t)} + \Omega_\Lambda\right]. \tag{3.18}$$

Since the radiation density Ω_R decreases with a^{-4} it is not relevant to the cosmic dynamics and will be neglected in the following, though it was dominant at early times. At present time, $t = t_0$, from $H(t_0) \equiv H_0$ it follows for the curvature density $\Omega_K \equiv -K(c/H_0)^2$:

$$\Omega_K = 1 - \Omega_0 - \Omega_\Lambda, \tag{3.19}$$

where $\Omega_0 \equiv \Omega_R + \Omega_m$. Introducing the equation of state $w = w(a)$ in equation (3.18) as a generalization which includes the cosmological constant:

$$\frac{H^2}{H_0^2} = \frac{\Omega_m}{a^3} + (1 - \Omega_m)\exp\left[3\int_a^1 \mathrm{d}\ln a\,(1 + w)\right], \tag{3.20}$$

where a vanishing curvature is assumed. The factor $\Omega_\Lambda = 1 - \Omega_m$ represents the dark energy density, the value $w = -1$ corresponds to the cosmological constant Λ.
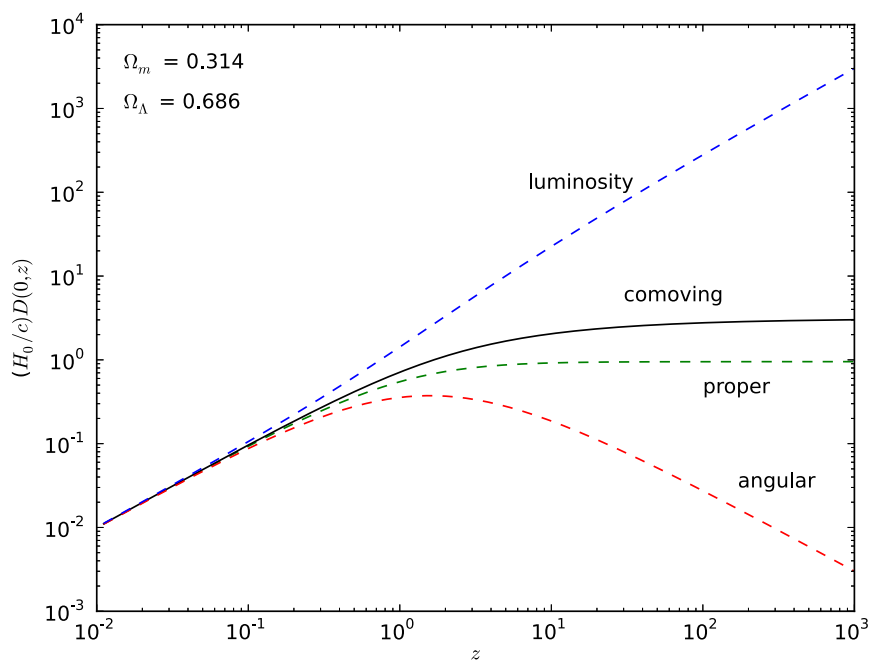
Figure 3.1.: Distance measures in cosmology calculated for cosmological parameters according to Planck.

3.1.2. Distances

In a non-static curved space distances defined by luminosity, coordinates, the travel time of light, or angle of observation can vary significantly. Here, an overview of the different measures of distance is given.

The **proper distance** is given by the travel time of light of emitted by a source at redshift z_0 to an observer at $z_1 < z_0$. Therefore the line element is $\mathrm{d}d_P = -c\mathrm{d}t = -c\dot{a}^{-1}\mathrm{d}a = -c(aH)^{-1}\mathrm{d}a$. Integrating the line elements from source to observer yields:

$$d_P(z_1, z_0) = \frac{c}{H_0} \int_{a(z_0)}^{a(z_1)} \mathrm{d}a \left[a^{-1}\Omega_\mathrm{m} + \Omega_K + a^2\Omega_\Lambda \right]^{-\frac{1}{2}}. \tag{3.21}$$

A measure which is invariant under the expansion of space-time is given by the **comoving distance**, or coordinate distance. It defined as the distance on the spatial hyper-surface $t = t_0$ between the world-lines of a source and an observer comoving with the cosmic flow. The corresponding line element is $\mathrm{d}d_C = \mathrm{d}\chi$, and since for light $\mathrm{d}s = 0$ the line element becomes $\mathrm{d}d_C = -ca^{-1}\mathrm{d}t = -c(a\dot{a})^{-1}\mathrm{d}a = -c(a^2H)^{-1}$, thus

$$\chi \equiv d_C(z_o, z_s) = \frac{c}{H_0} \int_{a(z_s)}^{a(z_o)} \mathrm{d}a \left[a\Omega_\mathrm{m} + a^2\Omega_K + a^4\Omega_\Lambda \right]^{-\frac{1}{2}}. \tag{3.22}$$

The **angular-diameter distance** d_A in curved space-time is modified by the scale factor and curvature is defined in analogy to the relation in Euclidean space between the physical cross section δA of an object at z_0 and the solid angle $\delta\omega$ that it subtends for an observer at z_1, $\Delta\Omega\, d_A^2 = \Delta A$. Thus, in the general case of a curved space-time:

$$d_A(z_1, z_0) = a(z_0)f_K\left[d_C(z_1, z_0)\right]. \tag{3.23}$$

The **luminosity distance** is defined in anology to the Euclidean case but with the generalised angular-diameter distance 3.23. The relation between the luminosity L of an object at z_0 and the flux S received by an observer at z_1 then reads:

$$d_L(z_1, z_0) = \left(\frac{a(z_1)}{a(z_0)}\right)^2 d_A(z_0, z_1) = \frac{a(z_1)^2}{a(z_0)} f_K\left[d_C(z_1, z_0)\right], \tag{3.24}$$

where the factor $(a(z_1)/a(z_0))^{-2}$ accounts for the redshift-induced reduction in energy flux and the increased time interval between subsequent photons.

The distance measures described above and calculated for cosmological parameters according to Planck (see 3.1.1.4) are depicted in Figure 3.1.

3.2. Structure formation

3.2.1. Growth of density perturbations in cold dark matter models

Matter perturbations are quantified by the density contrast $\delta(\boldsymbol{x}, a)$ which relates the local matter density $\delta(\boldsymbol{x}, a)$ to the mean matter density $\rho(a) = \langle\rho(a)\rangle$,

$$\delta(\boldsymbol{x}, a) = \frac{\rho(\boldsymbol{x}, a) - \rho(a)}{\rho(a)}, \tag{3.25}$$

and which is described by a homogeneous and Gaussian distribution. The dependence of the matter density on scale factor a reflects the evolution of the density contrast. For vanishing curvature $\bar{\delta} = \Omega_{\mathrm{m}}\rho_{\mathrm{crit}}a^{-3}$. In the Einstein-de Sitter limit ($\Omega_0 = 1, \Omega_\Lambda = 0$) for small perturbations $|\delta| \ll 1$ relativistic perturbation theory yields

$$\delta(a) \propto \begin{cases} a^2 & , a \ll a_{\mathrm{eq}}, \\ a & , a_{\mathrm{eq}} \ll a \ll 1, \end{cases} \tag{3.26}$$

where a_{eq} denotes the scale factor at the epoch of matter-radiation equality. At later times, when the Einstein de-Sitter limit does not hold ($\Omega_0 \neq 1$ or $\Omega_\Lambda \neq 0$), the evolution of density perturbations can be approximated by the growth function D_+ describing the homogenous growth of structure,

$$\delta(\boldsymbol{x}, a) = D_+\delta(\boldsymbol{x}, a = 1), \tag{3.27}$$

and which is the solution of the growth equation (Carroll et al. 1992, Turner & White 1997, Wang & Steinhardt 1998, Linder & Jenkins 2003)

$$\frac{\mathrm{d}^2}{\mathrm{d}a^2}D_+ + \frac{1}{a}\left(3 + \frac{\mathrm{d}\ln H}{\mathrm{d}\ln a}\right)\frac{\mathrm{d}}{\mathrm{d}a}D_+ = \frac{3}{2a^2}\Omega_{\mathrm{m}}D_+, \tag{3.28}$$

under Newtonian gravity in the linear regime.

3.2.2. Lagrangian perturbation theory

The peculiar motion of galaxies can be described using Lagrangian perturbation theory (LPT) if the flow of dark matter and of the advected galaxies is irrotational and nonlinearities are weak. In this limit, galaxies follow straight lines given by the gradient of the Lagrangian potential Φ_1 to first order LPT (1LPT) (Doroshkevich 1970, Zel'Dovich 1970, Buchert 1989, Moutarde et al. 1991, Bernardeau et al. 2002),

$$\boldsymbol{x} \to \boldsymbol{x} - D_+(a)\nabla\Phi_1, \tag{3.29}$$

where the Lagrangian potential Φ_1 is the solution to the Poisson equation,

$$\nabla^2\Phi_1 = \delta. \tag{3.30}$$

During linear structure growth, the Lagrangian potential Φ_1 is proportional to the true gravitational potential, the proportionality constant being $3\Omega_{\mathrm{m}}/2/\chi_H^2 D_+(a)/a$. This physical picture of particles following a straight paths does not hold anymore when trajectories are crossing.

3.3. Angular momenta of galaxies

The angular momentum of a matter distribution with center of mass $\bar{\boldsymbol{r}}$ is given by

$$\boldsymbol{L} = \int_V [\boldsymbol{r}(t) - \bar{\boldsymbol{r}}(t)] \times \boldsymbol{v}(\boldsymbol{r}, t)\rho(\boldsymbol{r}, t)\, \mathrm{d}\boldsymbol{r}, \tag{3.31}$$

where V denotes the comprising volume and $v(\boldsymbol{r}, t)$ the velocitiy of the fluid element with density $\rho(\boldsymbol{r}, t)$. Angular momentum acquired by tidal torquing between the proto-galaxy and the surrounding matter distribution, as suggested by Hoyle (1949), is only efficient before the collapse

of the proto-galaxy (Doroshkevich 1970, White 1984). For non-spherical shapes angular momentum grows at first order and linearly in time (Doroshkevich 1970). Peebles (1969) showed that for spherical regions the acquisition of angular momentum is a second-order effect, as a consequence of the fact that for a spherical region, there are no torques initially, so the growth is a result of convective effects on the bounding surface. The growth of perturbations can be described in Lagrangian perturbation theory (see 3.2.2), where, to first order, the trajectories of dark matter particles in comoving coordinates are given by the Zel'dovich approximation,

$$\boldsymbol{x} = \boldsymbol{q} - D_+(a)\nabla\Phi_1, \tag{3.32}$$

with growth function $D_+(a)$, describing the homogenous time evolution of the displacement field Φ_1. This approximation relates the initial partical positions $\boldsymbol{q}$ to the positions x and time t to linear order. In Lagrangian coordinates, the expression for the angular momentum becomes

$$\boldsymbol{L} = \rho_0 a^5 \int_{V_L} [\boldsymbol{x}(t) - \bar{\boldsymbol{x}}(t)] \times \dot{\boldsymbol{r}}\, \mathrm{d}\boldsymbol{r} \simeq \rho_0 a^5 \int_{V_L} [\boldsymbol{q}(t) - \bar{\boldsymbol{q}}(t)] \times \dot{\boldsymbol{r}}\, \mathrm{d}\boldsymbol{r} \tag{3.33}$$

If the gradient of the displacement potential $\nabla\Phi_1(\boldsymbol{q})$ does not vary much within the integration volume, a second-order Taylor expansion of the displacement potential at the center of gravity is applicable:

$$\partial_\alpha \Phi_1(\boldsymbol{q}) \simeq \partial_\alpha \Phi_1(\bar{\boldsymbol{q}}) + (\boldsymbol{q} - \bar{\boldsymbol{q}})_\beta T_{\alpha\beta}, \tag{3.34}$$

with $T_{\alpha\beta} \equiv \partial_\alpha \partial_\beta \Phi_1(\boldsymbol{q})$. Since the gradient of the displacement potential, $\partial_\alpha \Phi_1(\bar{\boldsymbol{q}})$, induces only a translation of the protogalactic object, only the second order derivatives sourcing differential advection velocities responsible for rotation, will be considered in the following. Introducing the tensor of second moments of the matter distribution of the protogalactic object as the inertial tensor $I_{\sigma\gamma}$

$$I_{\sigma\gamma} = \rho_0 a^3(t) \int_{V_L} (\boldsymbol{q} - \bar{\boldsymbol{q}})_\sigma (\boldsymbol{q} - \bar{\boldsymbol{q}})_\gamma \, \mathrm{d}\boldsymbol{r}, \tag{3.35}$$

yields the following expression of the angular momentum L_α:

$$L_\alpha = a^2 \dot{D}_+ \, \epsilon_{\alpha\beta\gamma} \, I_{\beta\sigma} \, T_{\sigma\gamma} = a^3 H(a) \frac{\mathrm{d}D_+}{\mathrm{d}a} \, \epsilon_{\alpha\beta\gamma} \, I_{\beta\sigma} \, T_{\sigma\gamma}, \tag{3.36}$$

where the time dependence has ben rewritten in terms of the scalefactor a by using the relation $\mathrm{d}D_+/\mathrm{d}t = aH(a)\mathrm{d}D_+/\mathrm{d}a$. From equation 3.36 it can be observed that angular momentum is mainly acquired before the collapse, when the interta tensor $I_{\sigma\gamma}$ is comparatively large, and that it remains constant after turnaround (Crittenden et al. 2001).

3.4. Non-Gaussian signatures from inflation

The non-Gaussianities considered in this work have their origin in an accelerated expansion of the Universe in an early epoch of its history before primordial nucleosynthesis. The energy density of the Universe at that time was dominated by vacuum energy determined by a scalar field, the so-called inflaton field. What makes inflation possible is the existence of states of matter that have a high energy density which cannot be rapidly lowered. In the original version of the

inflationary theory (Guth 1981), the proposed state was a scalar field in a local minimum of its potential energy function. The scalar field state employed in the original version of inflation is called a false vacuum, since the state temporarily acts as if it were the state of lowest possible energy density. Classically this state would be stable, because there would be no energy available to allow the scalar field to cross the potential energy barrier that separates it from states of lower energy. Quantum mechanically, however, the state would decay by tunneling (Coleman 1977) but the randomness of false vacuum decay would produce catastrophically large inhomogeneities. In the so called slow-roll inflation model, instead of tunneling out of a false vacuum state, inflation occurred by a scalar field rolling down a potential energy hill (Linde 1982, Albrecht & Steinhardt 1982). When the field rolls very slowly compared to the expansion of the universe, inflation occurs. However, when the hill becomes steeper, inflation ends and reheating can occur. The postulate of apparent superluminal expansion solves a number of cosmological problems, such as the flatness of the Universe, the excitation and stretching of quantum fluctuation out of the horizon to cosmic scales, and the observed CMB anisotropies and large scale structure. It solves the horizon problem by explaining why the universe appears statistically homogeneous and isotropic in accordance with the cosmological principle.

3.4.1. Statistics of non-Gaussianities

Any Gaussian distribution is described by its first two moments and is thus determined by two-point correlation functions. Non-Gaussian statistics, however, require higher order spectral estimates in order to be characterized. The bispectrum is an important observable since it is the lowest order statistics sensitive to non-Gaussian signatures in a given statistical distribution. The bispectrum is the equivalent of the three-point correlation function in Fourier space (see Chapter 5).

3.4.2. Primordial bispectrum

The primordial bispectra is written here in terms of the Bardeen curvature perturbation Φ (Bardeen 1980, Bardeen et al. 1983). The bispectrum of Φ is given by

$$\langle \Phi(\boldsymbol{k}_1)\Phi(\boldsymbol{k}_2)\Phi(\boldsymbol{k}_3)\rangle = (2\pi)^3 \delta_D(\boldsymbol{k}_1 + \boldsymbol{k}_2 + \boldsymbol{k}_3) B_\Phi(k_1, k_2, k_3). \tag{3.37}$$

The potential fluctuations are transformed to those of the density field by the Newtonian Poisson equation

$$\Delta\Phi = \frac{3}{2}\frac{\Omega_{\rm m}}{\chi_H^2}\delta, \tag{3.38}$$

or in Fourier space

$$\delta(k, a) = \frac{2}{3\Omega_{\rm m}}D_+(\chi_H k)^2 T(k)\Phi(k). \tag{3.39}$$

Each mode has a horizon passing which is governed by $T(k)$ and grows by D_+ in the linear regime, giving a bispectrum,

$$B_\delta(k_1, k_2, k_3, a) = \prod_{i=1}^{3}\left(\frac{2}{3\Omega_{\rm m}}D_+(\chi_H k_i)^2 T(k_i)\right)B_\Phi(k_1, k_2, k_3), \tag{3.40}$$

which is proportional to D_+^3 ([Munshi et al. 2011](#)). The normalisation factor A is chosen to be consistent with σ_8 for each linearly evolving mode.

4. Weak gravitational lensing

4.1. Weak lensing equations and observables

4.1.1. Gravitational light deflection

In the case of weak lensing, where the graviational field is weak ($\Phi \lesssim 10^{-3}$) the matter field equations of general relativity can be linearised. Then the relativistic deflection angle of a light ray with impact parameter b due to a point mass M is given by (Bartelmann & Schneider 2001, Lewis & Challinor 2006)

$$\delta\beta = \frac{4GM}{c^2 b}. \tag{4.1}$$

Since in the weak field approximation the impact parameter is much larger than the Schwarzschild radius the deflection angle is small. For a given mass distribution with Newtonian potential Φ the deflection becomes

$$\delta\beta = -2\delta_\chi \nabla_\perp \Phi, \tag{4.2}$$

where $\nabla_\perp$ denotes the transverse covariant derivative and δ_χ refers to the distance a photon has passed on its trajectory in a given time. The comoving distance that the source appears to have moved due to the lensing is $f_K(\chi_* - \chi)\,\delta\beta = f_K(\chi_*)\,\delta\theta$ (see Fig. 4.1). In the following, a sufficiently flat space is assumed, and thus $f_K(\chi) = \chi$ throughout this thesis. Solving for $\delta\theta$ yields for the corresponding deflection angle $\delta\theta$ (Lewis & Challinor 2006):

$$\delta\theta = \frac{\chi_* - \chi}{\chi_*}\delta\beta = -\frac{\chi_* - \chi}{\chi_*}2\delta_\chi \nabla_\perp \Phi. \tag{4.3}$$

The finally observed deflection $\boldsymbol{\alpha}$ is the sum of all deflection angles between observer and source and becomes by identifying $\chi\nabla_\perp$ with the angular derivative $\nabla_{\hat{\boldsymbol{n}}}$:

$$\boldsymbol{\alpha} = -2\int_0^{\chi_*} \mathrm{d}\chi \frac{\chi_* - \chi}{\chi_*}\nabla_\perp \Phi(\chi\hat{\boldsymbol{n}}; \eta_0 - \chi) = -2\int_0^{\chi_*} \mathrm{d}\chi \frac{\chi_* - \chi}{\chi_*\chi}\nabla_{\hat{\boldsymbol{n}}}\Phi(\chi\hat{\boldsymbol{n}}; \eta_0 - \chi), \tag{4.4}$$

where $\eta_0 - \chi$ is the conformal time at which the photon was at position $\chi\hat{\boldsymbol{n}}$ (Lewis & Challinor 2006). Equation (4.4) suggests that the deflection angle α can be expressed as a gradient of a lensing potential,

$$\psi = -2\int_0^{\chi_*} \mathrm{d}\chi \frac{\chi_* - \chi}{\chi_*\chi}\,\Phi(\chi\hat{\boldsymbol{n}}; \eta_0 - \chi), \tag{4.5}$$

Applying the Laplace operator $\nabla_{\hat{\boldsymbol{n}}}$ of Equation (4.5) and Poisson's equation yields

$$\nabla_{\hat{\boldsymbol{n}}}^2\psi = -2\int_0^{\chi_*} \mathrm{d}\chi \frac{\chi_* - \chi}{\chi_*\chi}\nabla_{\hat{\boldsymbol{n}}}^2\Phi(\chi\hat{\boldsymbol{n}}; \eta_0 - \chi) = 2\frac{4\pi G}{c^2}\int_0^{\chi_*} \mathrm{d}\chi \frac{\chi_* - \chi}{\chi_*\chi}\rho(\chi\hat{\boldsymbol{n}}; \eta_0 - \chi). \tag{4.6}$$
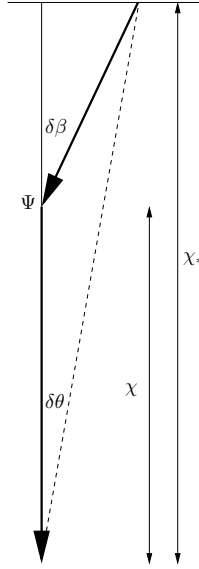
Figure 4.1.: Weak lensing geometry for a light ray emitted at a source at comoving distance χ_* deflected by the gravitational potential Φ at distance χ, assuming a flat universe (Figure from Lewis & Challinor (2006)). The lensing deflection by an angle $\delta\beta$ changes the observed angle of the source by an angle $\delta\theta$.

Interpreting the integral in Equation (4.6) as a Limber projection finally gives (Lewis & Challinor 2006)

$$\frac{1}{2}\nabla_{\hat{\mathbf{n}}}^2\psi = \frac{4\pi G}{c^2}\rho(\chi\hat{\mathbf{n}}) \equiv \kappa, \tag{4.7}$$

where the convergence κ can be regarded as a projected surface mass density weighted by geometrical factors according to the weak lensing efficiency. In the following $\nabla_{\hat{\mathbf{n}}}$ will be denoted by ∇.

4.1.2. Convergence and cosmic shear

Distortions of galaxy ellipticities are characterised by the second derivatives of the lensing potential,

$$\gamma_1 = \psi_{,11}, \quad \gamma_2 = \psi_{,12}, \tag{4.8}$$

which are the components of the shear, $\gamma \equiv \gamma_1 + \iota\gamma_2$. Weak lensing can be described by the lens mapping which can be linearised locally to give

$$\mathcal{A}(\boldsymbol{\theta}) = \frac{\partial\boldsymbol{\beta}}{\partial\boldsymbol{\theta}} = \delta_{ij} - \frac{\partial^2\psi(\boldsymbol{\theta})}{\partial\theta_i\partial\theta_j} = \begin{pmatrix} 1 - \kappa - \gamma_1 & -\gamma_2 \\ -\gamma_2 & 1 - \kappa + \gamma_1 \end{pmatrix}. \tag{4.9}$$

where κ is the convergence of the lensing potential, $\kappa \equiv \frac{1}{2}\nabla^2\psi$. The factor 1/2 can be derived by decomposing the projected tidal field with the Pauli-matrices σ_α, which constitute a basis for the

vector space of 2×2 matrices,

$$\psi = \sum_{\alpha=0}^{3} a_\alpha \sigma_\alpha = (1 - \kappa)\sigma_0 - \gamma_+ \sigma_1 - \gamma_\times \sigma_3, \tag{4.10}$$

(c.f. Abramowitz M. 1972), where σ_0 denotes the 2-dimensional unit matrix. For $\alpha = 1, 2, 3$, the Pauli-matrices have the properties $\sigma_\alpha^2 = \sigma_0$ and $\mathrm{tr}(\sigma_\alpha) = 0$. Due to the property $\sigma_\alpha \sigma_\beta = \sigma_0 \delta_{\alpha\beta} + i\epsilon_{\alpha\beta\gamma}\sigma_\gamma$ of the Pauli-matrices, the coefficients a_α can be recovered by using $a_\alpha = \frac{1}{2}\mathrm{tr}(\psi\sigma_\alpha)$. In particular, one identifies the weak lensing convergence $\kappa = \frac{1}{2}\mathrm{tr}(\psi\sigma_0)$ with the unit matrix σ_0 and the two components of shear $\gamma_+ = \frac{1}{2}\mathrm{tr}(\psi\sigma_1)$ and $\gamma_\times = \frac{1}{2}\mathrm{tr}(\psi\sigma_3)$. The standard expression for κ can be recovered with $\kappa = \frac{1}{2}\mathrm{tr}(\psi\sigma_0) = \frac{1}{2}\sum_i \partial_i\partial_i\psi = \frac{1}{2}\Delta_\theta\psi = \frac{1}{2}\mathrm{div}_\theta\alpha$ with the deflection angle $\alpha = \nabla_\theta\psi$.

4.2. Weak lensing statistics

4.2.1. Convergence power spectrum

The line-of-sight integration for the weak lensing convergence κ is weighted with the lensing efficiency $W_\kappa(\chi)$ (for a review, see Bartelmann & Schneider 2001, Bartelmann 2010), such that

$$\kappa = \int_0^{\chi_H} \mathrm{d}\chi\, W_\kappa(\chi)\delta. \tag{4.11}$$

Since this is a linear superposition, all statistical properties of the density field δ are preserved. The weak lensing efficiency is given by

$$W_\kappa(\chi) = \frac{3\Omega_m}{2a} \frac{1}{\chi_H^2} G(\chi)\chi, \tag{4.12}$$

with the lensing efficiency and matter density weighted distribution,

$$G(\chi) = \int_\chi^{\chi_H} \mathrm{d}\chi'\, n(z) \frac{\mathrm{d}z}{\mathrm{d}\chi'} \frac{\chi' - \chi}{\chi'}, \tag{4.13}$$

and redshift-dependent galaxy distribution $n(z)$. The projection for the spectrum $C_\kappa(\ell)$ is then given by Limber's equation (Limber 1954) which projects a homogeneous isotropic random field in three dimensions onto two dimensions,

$$C_\kappa(\ell) = \int_0^{\chi_H} \frac{\mathrm{d}\chi}{\chi^2} W_\kappa^2(\chi) P_\delta(k = \ell/\chi, a), \tag{4.14}$$

where for linear structure formation $C_\kappa(\ell) \propto D_+^2$.

4.2.2. Spectrum of the weak lensing potential

The spectrum of the weak lensing potential follows from substituting the line of sight-expression $\psi = 2 \int \mathrm{d}\chi\, G(\chi)/\chi\, \Phi$ into the Limber-equation,

$$C_\psi(\ell) = \int \frac{\mathrm{d}\chi}{\chi^4} G(\chi)^2 P_\Phi(k = \ell/\chi, a(\chi)). \tag{4.15}$$
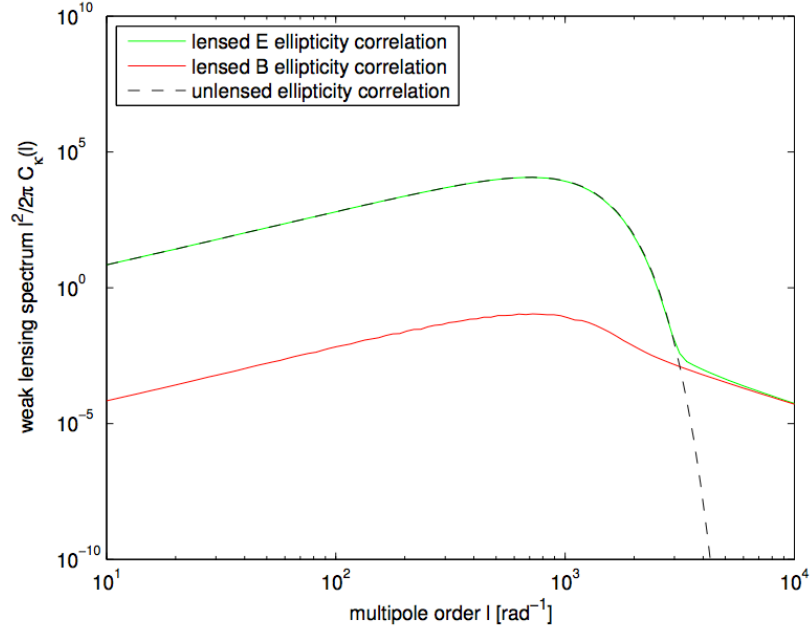
21

Figure 4.2.: Gradient $E-$ (green line) and curl $B-$ (red line) power in the ellipticity spectrum calculated for $z = 0.9$ and a galaxy distribution according to Euclid. The unlensed ellipticity spectrum (dashed line) is shown in comparison.

The power spectrum $P_\Phi(k, a)$ of the gravitational potential Φ at the scale-factor a follows from the comoving Poisson equation $\Delta\Phi = 3H_0^2\Omega_m/(2a)\delta$ and is related to the density power spectrum $P_\delta(k, a)$ by

$$P_\Phi(k, a) = \left(\frac{3\Omega_m}{2}\frac{D_+(a)}{a}\right)^2 \frac{P_\delta(k)}{(\chi_H k)^4}, \tag{4.16}$$

with the Hubble distance $\chi_H = c/H_0$ making the k^{-4}-factor dimensionless. By differentiation one obtains the spectrum $C_\alpha(\ell) = \ell^2 C_\psi(\ell)$ of the deflection angle $\alpha = \nabla_\theta\psi$ and the spectrum $C_\kappa(\ell) = \ell^4/4\, C_\psi(\ell)$ of the weak lensing convergence $\kappa = \frac{1}{2}\mathrm{div}_\theta\alpha = \frac{1}{2}\Delta_\theta\psi$. In the framework of the polarization formalism which is introduced in the following Section 4.3, the convergence spectrum is equal to the gradient- or E-mode correlation function $C_E^\gamma(\ell)$ of the weak lensing shear γ in the absence of curl correlations $C_B^\gamma(\ell)$. Nevertheless, due to the shifting effect of weak gravitational lensing, there will be a non-zero contribution to curl correlations from lensing, as depicted in Figure 4.2.

4.3. Polarization formalism for spin-2 fields

Both the shapes of galaxies and the polarization of the CMB have two degrees of freedom, the amplitude and orientation, and are invariant under rotations of an angle $\varphi = \pi$, allowing a representation by a complex number $Ae^{2i\varphi}$, where A denotes the amplitude. The real and imaginary part of this imaginary quantity are analogous to the Stokes parameters Q and U, defining the

polarization field $P = Q + iU$ for linearly polarized light. A rotation of the coordinate system of $\pi/8$ translates these two components into each other. In order to explore symmetries of a given vector field, it is useful to choose a coordinate basis which is invariant under rotations of the coordinate system. Such a basis, known as spin-2 harmonics and defining a natural basis (Lewis & Challinor 2006), will be used troughout this work. The transformation of the polarization field P in terms in spin-2 harmonics yields two components representing divergence and curl of the vector field. The separation into divergence and curl components is useful in order to characterize the nature of physical processes. Processes which are linear in the tidal field, such as lensing and shape distortions due to tidal stretching introduces curl-free correlations. Thus, any observation of curl correlation indicate an additional source of correlation caused by different physical mechanisms (Crittenden et al. 2002). For instance, correlations induced by tidal torquing, show non-zero curl due to the quadratic dependence on gravitational shear.

4.4. Relation between lensed and intrinsic galaxy ellipticities

4.4.1. Lens mapping for ellipticities

Lensing induces changes to the ellipticity according to Bartelmann & Schneider (2001):

$$\epsilon = \frac{\tilde{\epsilon} + g}{1 + g^*\tilde{\epsilon}} \approx \tilde{\epsilon} + g, \quad g \ll 1, \tag{4.17}$$

where $\tilde{\epsilon}$ denotes the un-lensed ellipticity and g the reduced shear $g = \gamma/(1 - \kappa)$.

4.4.2. Quadratic estimator from off-diagonality: Analogies between CMB and galaxy lensing

The weak gravitational lensing of the CMB temperature and polarization anisotropies allows to map the distribution of matter on large scales and high redshift where density fluctuations are still linear. It is the higher order correlations induced by lensing which carry the necessary information to make mass reconstruction possible (Bernardeau 1998). By remapping the CMB fields according to potential gradients, lensing acts as a convolution in Fourier space which introduces correlations between angular wavenumbers or multipole moments. From a quadratic combination of the multipoles, one can form estimators of the potential field and hence the intervening mass (Hu & Okamoto 2002). Hu (2001) showed that the minimum variance estimator constructed from the temperature field allows arcminute resolution CMB maps. This estimator enables mapping of the dark matter above the degree scale, where the deflection power peaks. The cosmic variance of the CMB temperature field itself prevents mapping on smaller scales. Since galaxy ellipticity fields, being spin 2 tensor fields, symmetry properties similar to CMB polarization maps, the question arises if an estimator could also be constructed for ellipticity fields. This analogy, however, is not valid in all regards since in contrast to the CMB polarization, where only shifting effects play a role, there is an additional shear effect distorting the ellipticities of galaxies. Nevertheless, it is possible to perform the analysis in analogy to Hu (2001).

In the case of CMB lensing the ensemble average is taken for a fixed lensing potential yields a quadratic estimator for ψ. Symmetry properties of the spin-2 ellipticity field suggest a similar approach for the weak lensing of galaxies. There is, however, an important distinction between these to cases. Where for CMB lensing the polarisation of the CMB photons is not correlated with the reduced shear g at leading order, the same is not true for the galaxy lensing. This can be seen from taking the ensemble average over the ellipticity field,

$$\langle \epsilon' \epsilon \rangle_\epsilon \approx \langle \tilde{\epsilon}' \tilde{\epsilon} \rangle_\epsilon + \langle g' g \rangle_\epsilon = \delta(L) \, C_\epsilon + g' g \tag{4.18}$$

where $g \leq 1$. Equation (4.18) indicates that for the off-diagonal case, $L \neq 0$, the shear term, $g'g$, does not vanish and is dominant ($C_g/C_\epsilon \sim 10$) (Giahi & Schäfer 2012). This poses a problem for the derivation of a quadratic estimator for the lensing potential since the reduced shear itself depends on the lensing potential and is the dominating off-diagonal components of the spectrum. Thus, due to the nature of weak gravitational lensing of galaxy ellipticities, for most multipole numbers a reconstruction according to Hu (2001) is not feasible and demonstrates the limitations of transferring reconstruction techniques for the CMB to lensed ellipticity fields.

5. Statistics

Statistical measures for model selection can be substantially different in nature, thus leading to sometimes contradictory results. Bayesian and Frequentist p-value statistics represent such a case, where the focus lies within different aspects of model comparison. Where p-value statistics as a measure of model accuracy does not take into account the information content of the data, the Bayesian approach is oriented towards finding an optimal solution taking into account both, accuracy and complexity. In the following, a brief description is given of these two statistical methods.

5.1. Gaussianity and Likelihoods

Gaussianity is often assumed on grounds of the central limit theorem which states that the accumulated effect of a sufficient number of arbitrary independent random processes with finite variance resembles a Gaussian distribution. The Gaussian statistics resulting from multiple deflections at gravitational potentials in weak gravitational lensing are such an example. If the deviation of every data point of a given data set from the true value is interpreted in terms of an independent random process, then the sum of the individual deviations, from all points can, by virtue of the central limit theorem, be expected to follow a Gaussian distribution. Thus, the likelihood of observing a particular χ^2 can be expected to be Gaussian distributed. This justifies to express the likehood in terms of χ^2 as

$$\mathcal{L} \propto \exp\left(-\frac{\chi^2}{2}\right). \tag{5.1}$$

If χ depends linearly on the parameters it follows from equation 5.1 that the likelihood is Gaussian distributed with respect to the parameters themselves. The likelihood is then represented by a multivariate Gaussian distribution or just a Gaussian function for a single parameter, which is the case for chapter 8.2 in this thesis.

5.2. Higher order statistics

By virtue of the central limit theorem (Section 5.1), many observations in nature can be described in a Gaussian fashion. Furthermore, it is common to linearize the underlying natural processes. The vast majority of phenomena, however, is inherently non-linear and also not necessarily comprehensively described by Gaussian statistics. The power spectrum is only sensitive to Gaussian distributions since, as a two-point statistic, it allows only the analysis of the first two moments. The lowest order statistics sensitive to non-Gaussian signatures is given by three-point correlators or their Fourier space analogue, the bispectrum which furthermore reveals coupling between

different Fourier modes due to non-linearities. In chapter 3 the relevant definitions for this work for both the power spectrum and the bispectrum are given.

5.3. Frequentist statistics

Frequentist statistics focusses on the accuracy of the results as the leading measure. In terms of the parameters f_{NL}^T and f_{NL}^M, relevant in chapter 8.2, the frequentist measure of the likelihood can be expressed by the probability $p(f_{\mathrm{NL}}^T \geq f_{\mathrm{NL}}^{\mathrm{obs}})$ referring to the likelihood of the value f_{NL}^M of a given model to be greater or equal than the observed value $f_{\mathrm{NL}}^{\mathrm{obs}}$,

$$p(f_{\mathrm{NL}}^M \geq f_{\mathrm{NL}}^{\mathrm{obs}}) = \int_{f_{\mathrm{NL}}^{\mathrm{obs}}}^{\infty} p\left(f_{\mathrm{NL}}|M\right) \, \mathrm{d}f_{\mathrm{NL}}, \tag{5.2}$$

and thus defines an estimate of the likelihood of obtaining more extreme fits. The null hypothesis is accepted with a significance level α (Lampton et al. 1976, Trotta 2007),

$$\alpha \leq 2\, p\left(f_{\mathrm{NL}}^M \geq f_{\mathrm{NL}}^{\mathrm{obs}}\right),$$

i.e. rejected with a confidence level of $1 - \alpha$. The probability function, $p(f_{\mathrm{NL}}^M \geq f_{\mathrm{NL}}^{\mathrm{obs}})$, is derived from the likelihood described in Section 5.1. Due to the symmetry of the Gaussian distribition there is a factor of 2 for a two-tailed p-value statistics. In contrast to the Bayesian philosophy, p-value statistics is not taking into account the information content of data.

5.4. Fisher formalism

In order to quantify the significance of deviations of parameter values from expectations a measure has been introduced which weights the probability of deviations from the assumed true parameter value with the covariance of the observation. The logarithm of the likelihood L of a given coordinate θ in parameter space is expanded at the parameter coordinate $\boldsymbol{\theta}_{\mathrm{max}}$ for maximum likelihood L_{max}. Since this is an expansion at the extremum of L, the first derivates vanish and the lowest order contributions are given by the second order derivatives, forming a Hessian matrix. Weighted by the covariance of the data, these derivatives are the constituents of the Fisher matrix,

$$F_{ij} = \left\langle \frac{\partial^2 \ln L}{\partial \theta_i \partial \theta_j} \right\rangle. \tag{5.3}$$

For a single parameter the Fisher matrix is a scalar.

The Cramer-Rao bounds, revealing a lower bound for the variance of an estimator is given by

$$\sigma = \sqrt{F^{-1}}. \tag{5.4}$$

5.5. Bayesian inference

One of the major problems in Bayesian model comparison is the choice of the prior, which seems to be arbitrary and subjective. For theoretical considerations a wide prior volume is desirable,

Table 5.1.: Jeffreys' scale

B	Evidence against the null-hypothesis
$10^{-1/2}$ to 1	Not worth more than a bare mention
10^{-1} to $10^{-1/2}$	Substantial
$10^{-3/2}$ to 10^{-1}	Strong
Less than 10^{-2}	Decisive

Logarithmic scale for interpreting Bayes ratios as introduced by Jeffreys (1998).

so that the posteriors are likelihood-driven. This would also allow for weakly conclusive data to have an impact on the posterior, whereas an experimental prior demands for significantly more conclusive data to show effect in the Bayesian analysis (Mukherjee et al. 2006). Nevertheless, the experimental prior is a compelling choice in view of the Bayesian philosophy of probability, and it is made by Trotta (2007). Both approaches, though, are in line with the Bayesian spirit of data-driven likelihoods and converge for highly conclusive data. However, in case of comparatively small (e.g. experimental) priors, weakly conclusive data will only lead to prior driven likelihoods. A way to quantify the information content of new data is given by the Kullback-Leibler divergence, which relates the prior volume to the posterior volume. In order to compare the two choices, both a theoretically and experimentally motivated prior are employed. In the Bayesian sense, the likelihood $\mathcal{L} \equiv P(D|\theta, M)$ is the conditional probability of obtaining a set of data D, given a point θ in parameter space corresponding to the parameters of the assumed model M and underlying model T. Bayesian statistics is based on the principles of Bayes law,

$$P(\theta|M, D) = \frac{P(D|\theta, M)P(\theta|M)}{P(D|M)}, \tag{5.5}$$

where for model comparison the likelihood is marginalized over parameter space, resulting in the Bayesian evidence $E_M \equiv P(D|M)$ and corresponding to a likelihood-weighted prior probability,

$$E_M = \int \mathrm{d}\theta \, P(D|\theta, M)P(\theta|M). \tag{5.6}$$

In order to compare two models a ratio, the Bayes factor, of the respective model likelihoods given the data is defined,

$$B_{AB} \equiv \frac{P(D|A)}{P(D|B)} = \frac{P(A)P(A|D)}{P(B)P(B|D)} = \frac{P(A)}{P(B)}\frac{E_A}{E_B}, \tag{5.7}$$

where the prior probabilities $P(A)$ and $P(B)$ assigned to the Models themselves are non-committal and taken to be equal in this work. The Bayes factor B serves as a statistical measure for model selection. Obviously, a Bayes factor close to unity leads to an undecisive result. In order to interpret the evidence of a given B in a standardized way, Jeffreys (1998) introduced a logarithmic scale (Table 5.1).

28

6. Weak gravitational lensing of intrinsic alignments

In weak lensing studies it is commonly assumed that the observed lensed galaxies would have had no shape-correlations without lensing, and that there is no clustering in the galaxy sample, neither along the line-of-sight nor perpendicular to it. In short, intrinsic ellipticities are drawn independently from a distribution which is commonly assumed to be Gaussian with variance σ_ϵ^2. In the estimation process of weak lensing spectra from galaxy shapes the intrinsic shape variations would contribute the Poissonian term σ_ϵ^2/n, if the estimation process comprises n galaxies. The physical picture employed in this study is a background field of intrinsically correlated ellipticities on which gravitational lensing acts by both, deflection and shear, while there are no correlations between the ellipticities and the matter distribution responsible for lensing. In this sense, lensing on II-alignments is considered, while GI-alignments are neglected, which vanish in the case of Gaussian fluctuations statistics for quadratic alignment models as the one used in this work, but would be present in nonlinear structures (Lee & Pen 2008). Other lensing-induced effects are modulations in the surface density of galaxies, due to the interplay between magnification of the image brightness and dilution over a larger solid angle, which will be neglected for the purpose of this study.

6.1. Introduction

In light of increasingly precise observations, such as EUCLID, the influence of intrinsic alignments on the convergence power spectrum is gaining practical significance.

Indeed, recent observations with the Sloan Digital Sky Survey (SDSS) (Mandelbaum et al. 2006, Lee & Pen 2007, Okumura & Jing 2009) and 2SLAQ (Hirata et al. 2007), WiggleZ (Mandelbaum et al. 2011), Point Source Catalog (PSC) (Lee & Pen 2002), Tully catalogue (Pen et al. 2000), and MegaZ-sample (Joachimi et al. 2011) report detection of intrinsic alignments. Since the weak lensing efficiency is increasing with redshift (for reviews on weak lensing, see Bartelmann & Schneider 2001, Bartelmann 2010), shallow surveys are suited best to reveal the contribution of intrinsic alignments to the observed signal.

Biases on wCDM cosmologies imposed by intrinsic alignment induced contaminations have been shown to be significant (King 2005, Bridle & King 2007, Joachimi & Bridle 2010, Kirk et al. 2010, 2012). (A study of the sensitivity of measured ellipticity correlations on intrinsic alignments and cosmological parameters can be found in Capranico et al. 2012). Understanding the influence of intrinsic alignments on observed ellipticity correlations is thus crucial for precise estimates of cosmological parameters. It should be mentioned, that Hirata & Seljak (2004) found that a further contribution arising from anticorrelations between foreground shear and intrinsic ellipticity to be a dominating contaminant.

While for cosmological parameter inference contaminations by intrinsic alignments cause severe constraints on the precision of the derived parameter values, the analysis of observed intrinsic alignments also sheds light on the question of galaxy formation. In both cases, methods for disentangling intrinsic alignments from weak gravitational shear are desirable. Such methods have been developed recently and cover a wide range of techniques, such as 'nulling' or 'boosting' methods in order to downweigh or amplify the contributions by intrinsic alignments by transforming the observed power spectra with a weighting function (Joachimi & Schneider 2008, 2010). These methods exploit the specific redshift depency and local nature of intrinsic alignments. As a consequence of the short correlation length of intrinsic alignments, a possibility to remove them from the observed signal is given by discarding close galaxy pairs with small redshift difference (King & Schneider 2002, Heymans & Heavens 2003, Heymans et al. 2004), or using different redshift slices for measuring the ellipticity correlation (King & Schneider 2003). Furthermore, 'self-calibration', i.e. constraining unknown parameters, of the intrinsinsic alignment signal can be achieved by additional information from cross-correlations between ellipticity and galaxy density where uncertainties in the intrinsic alignment model are marginalised over (Bernstein 2009, Zhang 2010, Joachimi & Bridle 2010). Kirk et al. (2013) show that, in principle, this technique allows to restore the information content of observed ellipticity correlations. A likelihood formalism based on a path integral method on continuous functions allowing for the removal of unknown systematics is introduced by (Kitching & Taylor 2011). Another way to observe intrinsic alignments is given by expanding the ellipticity field in gradient (E) and curl (B) modes. Since gravitational lensing, unlike intrinsic alignments is curl-free to first order, observed $B-$modes can be attributed to intrinsic alignments (Crittenden et al. 2002). This coordinate-independent representation offers analytical advantages due to its symmetry and will be used throughout this paper.

Galaxies are assumed to be formed at peaks in the dark matter concentration. Correlations between galaxies that are positioned in different halos thus imply correlations between two halos, giving rise to a so-called two-halo term, whereas correlation contributions of neighbouring galaxies located in the same halo are denoted by one-halo term. Schneider & Bridle (2010) introduce a model that distinguishes between contributions of central and satellite galaxies, where two-halo contributions are mainly due to central-central correlations, and one-halo contributions arise only by satellite-satellite correlations. One-halo terms support the intrinsic alignment power spectrum on small scales. Schäfer & Merkel (2012) extend the halo model by introducing a correlation function that also allows for anticorrelations and thus exhibits a more complex than only quadratic relation to the tidal field and by computing the alignment of tidal and intertia fields via a Gaussian random process.

Most models of galaxy formation assume that the shapes of galaxies are induced by tidal forces of large scale gravitational fields during the collapse. The so-called linear model (Hirata & Seljak 2004) is linear in the tidal field and believed to apply for elliptical galaxies. In this model tidal stretching is supposed to be the shape generating mechanism during galaxy formation (Catelan et al. 2001). For spiral galaxies, it is assumed that tidal stretching produces an anisotropic moment of inertia and that second order contributions from the tidal field induce an angular momentum by applying a torque (Crittenden et al. 2001). This model is also denoted as the quadratic model (Hirata & Seljak 2004). Tidal shear mechanisms have been investigated by perturbation theory, including the deformation of forming halos (Catelan 1995, Catelan & Theuns 1996b,a, Catelan et al. 2001, Catelan & Porciani 2001, Lee et al. 2007, Schäfer & Merkel 2012). By

30

statistical analysis of data from the SDSS, Blazek et al. (2011) have confirmed consistency with linear tidal shear models. Numerical studies investigating the role of tidal torquing in the angular momentum build-up during galaxy formation support theory, but indicate that tidal torquing models might be too positive on the amount of angular momentum (Bullock et al. 2001, Catelan & Porciani 2001, Porciani et al. 2002b,a, Bailin et al. 2005, Hahn et al. 2007).

Angular momentum alignments give rise to a correlation in intrinsic ellipticities between neighbouring galaxies if the angular momentum direction of the galaxy corresponds to the one of the host halo. The scale of this correlation is predicted to be in the range of ∼ 1 Mpc/h (Crittenden et al. 2001, Natarajan et al. 2001, Schäfer & Merkel 2012). Hence, intrinsic alignments influence the angular momentum correlation on small scales and can be of significance for high precision observations such as the future surveys mentioned above. Contaminations of cosmic shear by intrinsic alignments have been studied analytically (Crittenden et al. 2001, Mackey et al. 2002, Hirata & Seljak 2004) and with N-body simulations (Croft & Metzler 2000, Heavens et al. 2000, Semboloni et al. 2008). N-body simulations carried out by Croft & Metzler (2000) to explore the detectability of intrinsic alignments and predict a signal of 10-20 per cent due to intrinsic alignments. Based on an analytical tidal torque model, Crittenden et al. (2001) estimate the contamination from intrinsic alignments, depending on redshift, to be in the range between 1-10 per cent for a median redshift of $z = 1$, and even to dominate the cosmic shear for shallow surveys. For 3-point correlations, Semboloni et al. (2008) find an even stronger influence from intrinsic alignments, where for shallow surveys ($z ≈ 0.4$) the intrinsic signal is an order of magnitude larger than the shear and for $z ≈ 0.7$ the contamination is ≈ 15 per cent.

In chapter 7 (results published in Giahi & Schäfer (2012)), it is shown how peculiar velocities of galaxies introduce a time evolution of the ellipticity correlation function, giving rise to a decrease of ellipticity correlations on small scales of up to 10 per cent in the E-mode spectrum and 60 per cent in the B-mode spectrum. Motivation for this paper is to investigate the implications of the distortion due to weak gravitional shear of galaxy ellipticities and the displacement of galaxies caused by the gradient of the weak lensing potential on the shape of the *E*- and *B*-mode spectra of the lensed ellipticity correlation function. Thus, a formalism will be emplyed which is based on lensing of the cosmic microwave background (CMB) polarization (Seljak 1996a, Hu & White 2001, Challinor & Lewis 2005, Lewis & Challinor 2006). It should be mentioned that in contrast to the lensing of the CMB, where only the shifting effect is of importance and the polarization of the CMB photons remains unchanged, galaxy lensing involves, in addition, a distortion of ellipticities and a change of their orientation. In this regard, the effect of weak gravitational lensing on the polarization of the CMB and on the orientation of galaxy ellipticities has to be viewed differently. Here the model of Crittenden et al. (2001) is employed for deriving a correlation function for the intrinsic ellipticities and apply the CMB formalism to it in order to observe characteristic features of weak lensing, such as the mixing of E- and B-modes. In analogy to the study of the effect of peculiar galaxy velocities on the ellipticity power spectrum (Giahi & Schäfer 2012), which is described in Chapter 7, a suppression of ellipticity correlations is expected due to the shifting and mixing of the positions of neighbouring galaxies that originated from similar physical conditions. Furthermore, an analysis of the off-diagonal terms in the lensed ellipticity power spectrum is due to inhomogeneities induced by weak lensing is given. By this study it is intended to give a more detailed and deeper view into the implications of weak lensing on observations of intrinsic alignment.

The reference model of this work is a basic spatially flat *w*CDM model with Gaussian adiabatic

initial perturbations in cosmic density field. Model parameters were set to be $\Omega_m = 0.25$, $n_s = 1$, $\sigma_8 = 0.85$, $\Omega_b = 0.04$ and the Hubble-radius $c/H_0 = 2996.9$ Gpc/h, with $h = 0.72$. The dark energy equation of state parameter w was assumed to be constant at a value of -0.9.

6.2. Cosmology

6.2.1. Dark energy cosmologies

The time evolution of isotropic Friedmann-universe with homogeneous dark matter and dark energy is described by the Hubble function $H(a) = \mathrm{d}\ln a/\mathrm{d}t$, which is given by

$$\frac{H^2(a)}{H_0^2} = \frac{\Omega_m}{a^3} + (1 - \Omega_m)\exp\left(3\int_a^1 \mathrm{d}\ln a\,(1 + w(a))\right), \tag{6.1}$$

with the matter density parameter Ω_m and the dark energy equation of state function $w(a)$. Spatial flatness requires the dark energy density to be $1 - \Omega_m$. The comoving distance χ can be computed from the scale factor a,

$$\chi = c\int_a^1 \frac{\mathrm{d}a}{a^2 H(a)}. \tag{6.2}$$

For the galaxy redshift distribution $n(z)\mathrm{d}z$, a standard shape,

$$n(z) = n_0\left(\frac{z}{z_0}\right)^2 \exp\left(-\left(\frac{z}{z_0}\right)^\beta\right)\mathrm{d}z \quad \text{with} \quad \frac{1}{n_0} = \frac{z_0}{\beta}\Gamma\left(\frac{3}{\beta}\right), \tag{6.3}$$

is used, with $\beta = 3/2$. I choose z_0 such that the distribution has a median redshift of 0.9 corresponding to EUCLID which will be contrasted with a galaxy distribution of identical shape but with a much lower median of 0.3. This work refers to the two application cases as the high and low redshift galaxy sample, respectively. The distribution can be rewritten in terms of comoving distance using the relation $p(z)\mathrm{d}z = p(\chi)\mathrm{d}\chi$ with $\mathrm{d}z/\mathrm{d}\chi = H(\chi)/c$.

6.2.2. CDM power spectrum

The CDM power spectrum P_δ describes the wavelength dependence of the density correlations. For the statistically homogeneous Gaussian density field δ the power spectrum is defined in Fourier space as

$$\langle\delta(\boldsymbol{k})\delta(\boldsymbol{k}')\rangle = (2\pi)^3\delta_D(\boldsymbol{k} + \boldsymbol{k}')P_\delta(k), \tag{6.4}$$

in a sufficiently flat space. For the shape of the power spectrum the following Ansatz is used Bardeen et al. (1986):

$$P_\delta(k) \propto k^{n_s}T^2(k), \tag{6.5}$$

with $T(k)$ being a transfer function approximated by

$$T(q) = \frac{\ln(1 + 2.34q)}{2.34q}\left(1 + 3.89q + (16.1q)^2 + (5.46q)^3 + (6.71q)^4\right)^{-\frac{1}{4}}, \tag{6.6}$$

and $k = q\Gamma$ measured in units of the shape parameter (Sugiyama 1995)

$$\Gamma = \Omega_m h \exp\left[-\Omega_b\left(1 + \frac{\sqrt{2h}}{\Omega_m}\right)\right]. \tag{6.7}$$

The amplitude of P_δ is normalized on the scale $R = 8$ Mpc/h to the variance σ_8,

$$\sigma_R^2 = \int \frac{k^2 \mathrm{d}k}{2\pi^2} P_\delta(k) W^2(kR), \tag{6.8}$$

with a Fourier transformed spherical top hat filter function $W(x) = 3j_1(x)/x$, and j_1 denoting the spherical Bessel function of the first kind of order ℓ (Abramowitz M. 1972).

6.3. Weak gravitational lensing

6.3.1. Weak lensing formalism

The lensing potential ψ is defined as the line of sight projected gravitational potential Φ

$$\psi = \int_0^{\chi_H} \mathrm{d}\chi \, \frac{G(\chi)}{\chi} \, \Phi, \tag{6.9}$$

with the lensing-efficiency weighted galaxy distribution $G(\chi)$ as a weighting function,

$$G(\chi) = \int_\chi^{\chi_H} \mathrm{d}\chi' \, n(\chi')\left(1 - \frac{\chi}{\chi'}\right) \tag{6.10}$$

The lensing deflection angle α is obtained from the lensing potential ψ by differentiation, $\alpha_i = \partial_i \psi$. Further differentiation yiels the projected tidal field $\psi \equiv \partial_i \partial_j \psi$ which can be decomposed with the Pauli-matrices σ_α, because they constitute a basis for the vector space of 2×2 matrices,

$$\psi = \sum_{\alpha=0}^{3} a_\alpha \sigma_\alpha = (1 - \kappa)\sigma_0 - \gamma_+ \sigma_1 - \gamma_\times \sigma_3, \tag{6.11}$$

(c.f. Abramowitz & Stegun 1972, Arfken & Weber 2005), where σ_0 denotes the 2-dimensional unit matrix. For $\alpha = 1, 2, 3$, the Pauli-matrices have the properties $\sigma_\alpha^2 = \sigma_0$ and $\mathrm{tr}(\sigma_\alpha) = 0$. Due to the property $\sigma_\alpha \sigma_\beta = \sigma_0 \delta_{\alpha\beta} + \mathrm{i}\epsilon_{\alpha\beta\gamma}\sigma_\gamma$ of the Pauli-matrices, the coefficients a_α can be recovered by using $a_\alpha = \frac{1}{2}\mathrm{tr}(\psi\sigma_\alpha)$. In particular, one identifies the weak lensing convergence $\kappa = \frac{1}{2}\mathrm{tr}(\psi\sigma_0)$ with the unit matrix σ_0 and the two components of shear $\gamma_+ = \frac{1}{2}\mathrm{tr}(\psi\sigma_1)$ and $\gamma_\times = \frac{1}{2}\mathrm{tr}(\psi\sigma_3)$. The standard expression for κ can be recovered with $\kappa = \frac{1}{2}\mathrm{tr}(\psi\sigma_0) = \frac{1}{2}\sum_i \partial_i\partial_i\psi = \frac{1}{2}\Delta_\theta\psi = \frac{1}{2}\mathrm{div}_\theta\alpha$ with the deflection angle $\alpha = \nabla_\theta\psi$.

The two components of lensing shear are combined to form the complex shear $\gamma = \gamma_+ + \mathrm{i}\gamma_\times$ with the transformation property $\gamma \to \gamma \exp(2\mathrm{i}\varphi)$ under a rotation of the coordinate frame by an angle φ. Violations of the symmetry of ψ are very small and might e.g. be caused by geodesic effects such as lens-lens-coupling and Born-corrections (see Shapiro & Cooray 2006, Cooray & Hu 2002, Krause & Hirata 2010, Bernardeau et al. 2010, for a detailed computation). Therefore, an expansion coefficient for the contribution due to σ_2 which parameterises image rotation was neglected. In the limit of weak lensing, the galaxy ellipticity is transformed according to $\epsilon \to \epsilon + \gamma$.
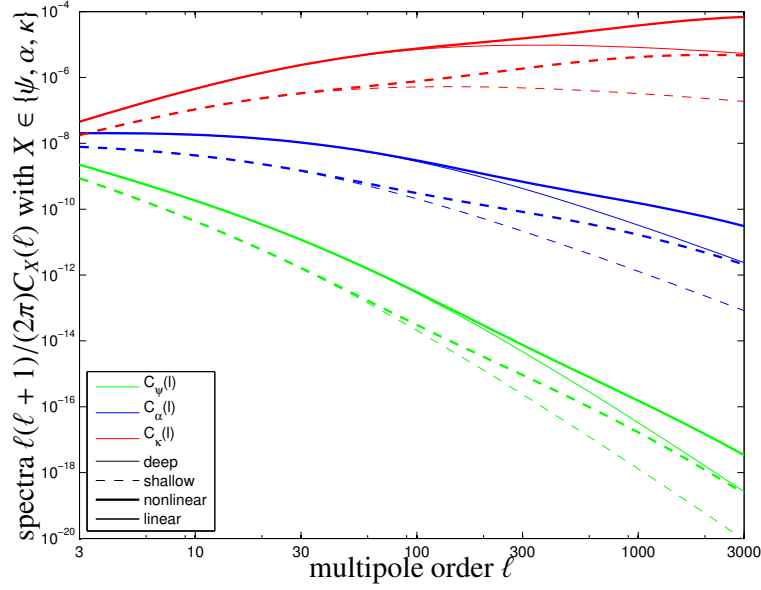
Figure 6.1.: Angular spectrum $C_\psi(\ell)$ (green line) of the lensing potential ψ, the spectrum $C_\alpha(\ell) \equiv \ell^2 C_\psi(\ell)$ (blue line) of the lensing deflection field $\alpha = \nabla_\theta \psi$ and the spectrum $C_E^\gamma(\ell) = C_\kappa(\ell) = \ell^4/4\, C_\psi(\ell)$ of the E-mode shear, for the high redshift galaxy sample (solid lines) and the low redshift galaxy sample (dashed lines), comparing the prediction for a linear CDM spectrum (thin lines) with a nonlinear one (thick lines).

6.3.2. Spectrum of the weak lensing potential

The spectrum of the weak lensing potential follows from substituting the line of sight-expression $\psi = \int d\chi\, G(\chi)/\chi\, \Phi$ into the Limber-equation,

$$C_\psi(\ell) = \int_0^{\chi_H} \frac{d\chi}{\chi^4}\, G(\chi)^2\, P_\Phi(k = \ell/\chi, a(\chi)). \tag{6.12}$$

The power spectrum $P_\Phi(k, a)$ of the gravitational potential Φ at the scale-factor a follows from the comoving Poisson equation $\Delta\Phi = 3H_0^2\Omega_m/(2a)\delta$ and is related to the density power spectrum $P_\delta(k, a)$ by

$$P_\Phi(k, a) = \left(\frac{3\Omega_m}{2}\frac{D_+(a)}{a}\right)^2 \frac{P_\delta(k)}{(\chi_H k)^4}, \tag{6.13}$$

with the Hubble distance $\chi_H = c/H_0$ making the k^{-4}-factor dimensionless. By differentiation one obtains the spectrum $C_\alpha(\ell) = \ell^2 C_\psi(\ell)$ of the deflection angle $\alpha = \nabla_\theta \psi$ and the spectrum $C_\kappa(\ell) = \ell^4/4\, C_\psi(\ell)$ of the weak lensing convergence $\kappa = \frac{1}{2}\text{div}_\theta\alpha = \frac{1}{2}\Delta_\theta\psi$, which is equal to the E-mode correlation function $C_E^\gamma(\ell)$ of the weak lensing shear γ in the absence of $C_B^\gamma(\ell)$ (c.f. the following section).

The angular spectrum $C_\psi(\ell)$ of the weak lensing potential ψ resulting from the Limber-projection of $P_\Phi(k)$ is depicted in Fig. 6.1 along with the spectrum $C_\alpha(\ell)$ of the lensing deflection angle α

and the weak lensing shear spectrum $C_E^\gamma(\ell)$, for the high redshift galaxy sample with $z_{\mathrm{med}} = 0.9$ and the low redshift galaxy sample with $z_{\mathrm{med}} = 0.3$. Furthermore, predictions for the spectra using a linear and a nonlinear CDM spectrum $P(k)$ are contrasted.

6.4. Galaxy formation and ellipticities

6.4.1. Angular momentum from tidal shearing

Angular momentum generation in CDM-haloes is a Lagrangian perturbative process (Hoyle 1949, Sciama 1955, Peebles 1969, Doroshkevich 1970, White 1984): The variation of velocities displacing a protogalactic region acts as a torque which generates angular momentum L_α:

$$L_\alpha = a^3 H(a) \frac{\mathrm{d}D_+}{\mathrm{d}a} \epsilon_{\alpha\beta\gamma} I_{\beta\delta} \Phi_{,\delta\gamma},$$
(6.14)

with the tidal shear being defined as the Hessian of the gravitational potential and the inertia tensor measuring the second moments of the mass distribution inside the protohalo,

$$\Phi_{,\delta\gamma} \equiv \frac{\partial^2 \Phi}{\partial x_\delta \partial x_\gamma} \quad \text{and}$$
(6.15)

$$I_{\beta\delta} \equiv \Omega_{\mathrm{m}} \rho_{\mathrm{crit}} \int \mathrm{d}^3 q \, \delta(\boldsymbol{q}) (\boldsymbol{q} - \bar{\boldsymbol{q}})_\beta (\boldsymbol{q} - \bar{\boldsymbol{q}})_\delta,$$
(6.16)

respectively, with implicit summation over repeated indices. $\boldsymbol{q}$ are Lagrangian coordinates moving along with the halo's centre of gravity $\bar{\boldsymbol{q}}$.

This relation reflects the interesting requirement of misalignments between the shear and inertia eigensystems which is necessary for angular momentum generation: Only the antisymmetric tensor $X_{\beta\gamma}^- = \sum_\delta (I_{\beta\delta}\Phi_{,\delta\gamma} - \Phi_{,\beta\delta}I_{\delta\gamma})/2$ is relevant for the angular momentum (Merkel & Schäfer 2011), $L_\alpha \propto X_{\beta\gamma}^-$, because the contraction of the symmetric contribution $X_{\beta\gamma}^+$ with the antisymmetric $\epsilon_{\alpha\beta\delta}$ vanishes. The antisymmetric tensor X_- is equal to the commutator $[I_{\beta\delta}, \Phi_{,\delta\gamma}]$ which suggests that the tidal shear and the inertia are not allowed to be simultaneously diagonalisable and must not have a common eigensystem, otherwise angular momentum can not arise.

In this work the angular momentum-based ellipticity correlation model proposed by Crittenden et al. (2001) is used. There, ellipticities are set into relation to tidal shear by means of a conditional probability distribution $p(\boldsymbol{L}|\Phi_{,\alpha\beta})\mathrm{d}\boldsymbol{L}$. Such a distribution has been proposed by Lee & Pen (2001) as being Gaussian with the covariance

$$\mathrm{cov}(L)_{\alpha\beta} \propto \frac{1}{3}\left(\frac{1+a}{3}\delta_{\alpha\beta} - a\,(\hat{\Phi}^2)_{\alpha\beta}\right),$$
(6.17)

which acquires a dependence on the tidal shear tensor, that has been normalised and made trace-free, $\mathrm{tr}(\hat{\Phi}) = 0$ and $\mathrm{tr}(\hat{\Phi}^2) = 1$. In this way, the variance of the angular momentum field varies with the tidal shear, and the randomness of the angular momentum field is controlled by the misalignment parameter a, which describes the average orientation of the protohalo's inertia to the tidal shear eigensystem. a has been measured in numerical simulation to be the value $\simeq 0.25$ for galactic halos.

This description is valid on scales where the correlations between inertia tensors are negligible and is sufficient because the focus of this thesis is on the angular momentum direction. Therefore, one does not need the variance $\langle \boldsymbol{L}^2 \rangle$ of the angular momentum field as a parameter and it is possible to marginalise the distribution over the magnitude L,

$$p(\hat{L}|\Phi_{,\alpha\beta}) = \int L^2 \mathrm{d}L \; p(\boldsymbol{L}|\Phi_{,\alpha\beta}). \tag{6.18}$$

In this picture correlations between angular momenta can be traced back to correlations between tidal shears that neighbouring galaxies experienced in building up their angular momenta.

6.4.2. Intrinsic ellipticity correlations from angular momenta of the host halos

In this work, it is assumed that the halo angular momentum axis and the symmetry axis of the galactic disk are parallel. The tilting of the disk relative to the line of sight determines the aspect ratio under which the galactic disk is viewed and therefore the galaxy's ellipticity. In this way, the angular momentum direction $\hat{L} = \boldsymbol{L}/L$ with $L = |\boldsymbol{L}|$ determines the ellipticity ϵ. In this picture, ellipticity correlations are derived from angular momentum direction correlations and ultimately from tidal shear correlations (Heavens et al. 2000, Crittenden et al. 2001, 2002, Mackey et al. 2002, Heymans & Heavens 2003). Specifically, the two components of the ellipticity field can be combined to form the complex ellipticity with ϵ_+ as the real and $\epsilon_\times$ as the complex part, and related to the angular momentum direction $\hat{L}$:

$$\epsilon = \epsilon_+ + \mathrm{i}\epsilon_\times \quad \text{with} \quad \epsilon_+ = \alpha \frac{\hat{L}_x^2 - \hat{L}_y^2}{1 + \hat{L}_z^2}, \quad \epsilon_\times = 2\alpha \frac{\hat{L}_x \hat{L}_y}{1 + \hat{L}_z^2}, \tag{6.19}$$

when the coordinate system is aligned with its z-axis parallel to the line of sight. Under a rotation of the coordinate frame by an angle φ the complex ellipticity transforms according to the relation $\epsilon \rightarrow \exp(2\mathrm{i}\varphi)\epsilon$, in accordance with the spin-2 property of the ellipticity field. α is the disk thickness parameter and can be used for describing a weaker dependence of ϵ on $\hat{L}$ if the galactic disk has a finite thickness. In this thesis, the numerical value $\alpha = 0.75$, which has been measured in the APM galaxy sample by Crittenden et al. (2001), is used.

Linking the ellipticity components ϵ_+ and $\epsilon_\times$ to the angular momentum direction $\hat{L}$ and ultimately to the tidal shear tensor by means of the conditional probability density $p(\boldsymbol{L}|\Phi_{,\alpha\beta})\mathrm{d}\boldsymbol{L}$ provides means to derive ellipticity correlations in terms of tidal shear correlations, and ultimately as functions of the CDM-spectrum. Because the ellipticity correlations of galaxies are of interest here, the CDM-spectrum is smoothed with a Gaussian filter on the mass-scale $3 \times 10^{11} M_\odot/h$. Employing the covariance $\langle L_\alpha L_\beta \rangle$ as a function of the squared tidal shear tensor, as advocated by Lee & Pen (2001), it is possible to relate the tidal shear correlations to the spectrum of the density field. This allows to derive a 3-dimensional correlation function of the ellipticity field as a function of moments $\zeta_n(r)$ (see Crittenden et al. 2001) of the CDM-spectrum and finally to carry out a Limber projection for obtaining the angular correlation function of the ellipticity field. The correlation function can be Fourier-transformed to yield the E-mode and B-mode ellipticity spectra (c.f. Sect. 6.5.2).

6.5. Imprints of lensing on ellipticities

6.5.1. Lensing effects on ellipticity fields

In weak lensing studies it is commonly assumed that the observed lensed galaxies would have had no shape-correlations without lensing, and that there is no clustering in the galaxy sample, neither along the line-of-sight nor perpendicular to it. In short, intrinsic ellipticities are drawn independently from a distribution which is commonly assumed to be Gaussian with variance σ_ϵ^2. In the estimation process of weak lensing spectra from galaxy shapes the intrinsic shape variations would contribute the Poissonian term σ_ϵ^2/n, if the estimation process comprises n galaxies.

The physical picture in this work is a background field of intrinsically correlated ellipticities on which gravitational lensing acts by deflection and shear, while there are no correlations between the ellipticities and the lensing matter distribution responsible for lensing. In this sense, I consider lensing on II-alignments, while neglecting GI-alignments, which vanish in the case of Gaussian fluctuations statistics for quadratic alignment models as the one used in this work, but would be present in nonlinear structures (Lee & Pen 2008). Other lensing-induced effects are modulations in the surface density of galaxies, due to the interplay between magnification of the image brightness and dilution over a larger solid angle, which is neglected for the purpose of this work.

6.5.2. Weak lensing of galaxy ellipticities

Both the galaxy ellipticities and the Stokes-parameters of the CMB-polarisation form a tensorial spin-2 field, which means that rotations of the coordinate frame by an angle φ give rise to a transformation of the tensor components as $\epsilon \rightarrow \exp(2\mathrm{i}\varphi)\epsilon$ and $P \rightarrow \exp(2\mathrm{i}\varphi)P$, when the ellipticity is written as a complex ellipticity $\epsilon = \epsilon_+ + \mathrm{i}\epsilon_\times$ and the polarisation tensor P is composed of the Stokes parameters Q and U according to $P = U + \mathrm{i}Q$.

Correlations between two points $\boldsymbol{\theta}_1$ and $\boldsymbol{\theta}_2$ separated by the distance θ of a spin-2 field such as the complex polarisation $P = Q + \mathrm{i}U$, the complex ellipticity $\epsilon = \epsilon_+ + \mathrm{i}\epsilon_\times$ or the weak lensing shear $\gamma = \gamma_+ + \mathrm{i}\gamma_\times$ are described in terms of two correlation functions $\xi_\pm(\theta)$,

$$\xi_+(\theta) = \langle\epsilon_+(\boldsymbol{\theta}_1)\epsilon_+(\boldsymbol{\theta}_2)\rangle + \langle\epsilon_\times(\boldsymbol{\theta}_1)\epsilon_\times(\boldsymbol{\theta}_2)\rangle \tag{6.20}$$

$$\xi_-(\theta) = \langle\epsilon_+(\boldsymbol{\theta}_1)\epsilon_+(\boldsymbol{\theta}_2)\rangle - \langle\epsilon_\times(\boldsymbol{\theta}_1)\epsilon_\times(\boldsymbol{\theta}_2)\rangle \tag{6.21}$$

which will be employed for the ellipticity field while of course completely analogous relations apply to the polarisation field. The correlation functions $\xi_\pm(\theta)$ are constructed from the variances of the components ϵ_+ and $\epsilon_\times$ using vanishing cross-correlations, $\langle\epsilon_+\epsilon_\times\rangle = 0$. They can be transformed to the spectra $C_E^\epsilon(\ell)$ and $C_B^\epsilon(\ell)$ of the gradient (E) and vorticity (B) modes of the ellipticity field,

$$C_E^\epsilon(\ell) = \pi \int \theta\mathrm{d}\theta \left[\xi_+(\theta)J_0(\ell\theta) + \xi_-(\theta)J_4(\ell\theta)\right], \tag{6.22}$$

$$C_B^\epsilon(\ell) = \pi \int \theta\mathrm{d}\theta \left[\xi_+(\theta)J_0(\ell\theta) - \xi_-(\theta)J_4(\ell\theta)\right], \tag{6.23}$$

by Fourier transform (Kaiser 1992, Schneider et al. 2002, Schneider & Kilbinger 2007, Fu & Kilbinger 2010). Completely analogous formulae apply for the description of the angular correlation properties of the weak lensing shear and their transformation to Fourier space yielding $C_E^\gamma(\ell)$ and $C_B^\gamma(\ell)$, the latter of which is zero if lensing on a scalar gravitational potential is considered and if the Born-approximation applies.

Figs. 6.4 and 6.5 shows intrinsic ellipticity spectra $C_E^\epsilon(\ell)$ and $C_B^\epsilon(\ell)$ for the EUCLID galaxy sample with its median redshift at $z_{\mathrm{med}} = 0.9$ which are contrasted with the spectra $C_E^\epsilon(\ell)$ and $C_B^\epsilon(\ell)$ for a galaxy sample with a much lower median redshift of $z_{\mathrm{med}} = 0.3$. For comparison, the corresponding spectra $C_E^\gamma(\ell)$ for the weak lensing shear γ measured on the same galaxy populations are superposed.

The spectra are constant and equal in amplitude up to multipoles of $\ell \simeq 100$, indicating the absence of correlations such that on each scale on measures the variance of the uncorrelated ellipticity field. Correlations become important on angular scales $\ell \gtrsim 300$ where the spectra level off and decrease from multipoles of $\ell \gtrsim 3000$ on very rapidly. In the peak region, the ellipticity E-modes have an amplitude larger than the B-modes by about an order of magnitude.

6.5.3. Adaptation of the CMB-lensing formalism

As in the case of CMB lensing where the (complex) polarisation tensor $P(\boldsymbol{\theta}) = Q(\boldsymbol{\theta}) + iU(\boldsymbol{\theta})$ is measured at a new position $\boldsymbol{\theta} + \boldsymbol{\alpha}$ due to gravitational lensing, it is asserted that the ellipticity ϵ is not observed at the true position $\boldsymbol{\theta}$ of the galaxy, but at the apparent position $\boldsymbol{\theta} + \boldsymbol{\alpha}$, $\epsilon(\boldsymbol{\theta}) \rightarrow \epsilon(\boldsymbol{\theta} + \boldsymbol{\alpha})$ with the lensing deflection angle $\boldsymbol{\alpha}$. Additionally, a variation of the deflection angle across the galaxy image leads to a distortion described by the complex shear γ and the convergence κ.

Adapting the CMB-lensing formalism, correlations between the components of the shifting angle α at two positions $\boldsymbol{\theta}_1$ and $\boldsymbol{\theta}_2$ are described by (Seljak 1996a)

$$\langle \alpha_i(\boldsymbol{\theta}_1)\alpha_j(\boldsymbol{\theta}_2) \rangle = \frac{1}{2}C_0(\theta) - C_2(\theta)\,\hat{\theta}_{\langle i}\hat{\theta}_{j\rangle} \tag{6.24}$$

with $\boldsymbol{\theta} = \boldsymbol{\theta}_2 - \boldsymbol{\theta}_1$. The two correlation functions of the deflection angle are defined as

$$C_0(\theta) = \int \frac{\ell^3 \mathrm{d}\ell}{2\pi} C_\psi(\ell) J_0(\ell\theta) \tag{6.25}$$

and

$$C_2(\theta) = \int \frac{\ell^3 \mathrm{d}\ell}{2\pi} C_\psi(\ell) J_2(\ell\theta). \tag{6.26}$$

We abbreviate the variance of the deflection angle

$$\sigma^2(\theta) = C_0(0) - C_0(\theta) \tag{6.27}$$

in complete analogy to CMB-lensing for describing uncorrelated deflections.

The characteristic function of $\boldsymbol{\alpha}$, i.e. the Fourier transform of the probability density $p(\boldsymbol{\alpha})\mathrm{d}\boldsymbol{\alpha}$ is then obtained as:

$$\langle \exp\left(i\boldsymbol{\ell}\left[\boldsymbol{\alpha}(\boldsymbol{\theta}_1) - \boldsymbol{\alpha}(\boldsymbol{\theta}_2)\right]\right) \rangle = \exp\left(\frac{\ell^2}{2}\left[-\sigma^2(\theta) + \cos 2\varphi_\ell C_2(\theta)\right]\right), \tag{6.28}$$
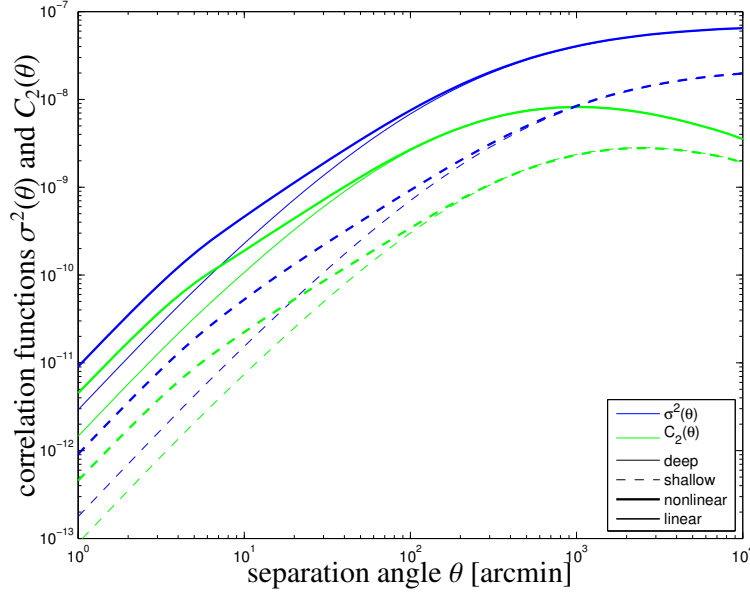
Figure 6.2.: Correlation functions $\sigma^2(\theta) = C_0(0) - C_0(\theta)$ (blue line) and $C_2(\theta)$ (green line) as a function of separation angle θ, for the high redshift galaxy sample (solid line) and the low redshift galaxy sample (dashed line), again comparing the predictions from linear (thin lines) and nonlinear (thick lines) CDM spectra.

and can be expressed in the case of Gaussian distributions in terms of $\sigma^2(\theta)$ and $C_2(\theta)$. In the case of CMB-lensing, non-Gaussian contributions have been shown to have negligible effect on the deflection angle statistics (Carbone et al. 2009, Merkel & Schäfer 2011) and in the case of weak cosmic shear, arguments about the rarity of strong deflections not described by a Gaussian distributions apply in a similar way (Hamana et al. 2005).

Fig. 6.2 shows the quantities $\sigma^2(\theta) = C_0(0) - C_0(\theta)$ and $C_2(\theta)$ needed in this formalism, for both a high and a low redshift galaxy sample and for linear and nonlinear CDM-spectra: Both correlation functions assume larger values for the high-redshift sample and for lensing on nonlinear structures, which in particular causes a larger variance of the deflection angle on small angular scales. For large values of of the argument θ, both correlation function start to oscillate rapidly.

The correlation properties of the lensing-distorted ellipticity field can be described using the two correlation functions $\xi_\pm(\theta)$,

$$\xi'_+(\theta) = \langle \epsilon^*(\boldsymbol{x} + \boldsymbol{\alpha})\epsilon(\boldsymbol{x}' + \boldsymbol{\alpha}') \rangle \tag{6.29}$$

$$\xi'_-(\theta) = \langle \exp(-4\mathrm{i}\phi_\ell)\epsilon(\boldsymbol{x} + \boldsymbol{\alpha})\epsilon(\boldsymbol{x}' + \boldsymbol{\alpha}') \rangle. \tag{6.30}$$

Substituting the correlation function for the deflection angle in the Fourier-transforms of the above expressions yields the correlation functions $\xi'_\pm(\theta)$ of the new ellipticity field. They can be transformed to E-mode and B-mode spectra with the standard transformations eqns. (6.22) and (6.23).

These steps lead to a transformation formula the E-mode and B-mode spectra of the ellipticity field, which can be summarised by a concise matrix notation:

$$\begin{pmatrix} C'_E(\ell) \\ C'_B(\ell) \end{pmatrix} = \int \ell' \mathrm{d}\ell' \begin{pmatrix} W_+(\ell, \ell') & W_-(\ell, \ell') \\ W_-(\ell, \ell') & W_+(\ell, \ell') \end{pmatrix} \begin{pmatrix} C^\epsilon_E(\ell') \\ C^\epsilon_B(\ell') \end{pmatrix}. \tag{6.31}$$

This notation shows explicitly the mixing between scales due to the convolution weighted with $W_+(\ell, \ell')$ and the conversion between $C^\epsilon_E(\ell)$ and $C^\epsilon_B(\ell)$ under the influence of $W_-(\ell, \ell')$. These kernels $W_\pm(\ell, \ell')$ are given by

$$W_+(\ell, \ell') = \frac{1}{2} \int \theta \mathrm{d}\theta \left[J_0(\ell\theta) A(\ell', \theta) + J_4(\ell\theta) B(\ell', \theta) \right], \tag{6.32}$$

$$W_-(\ell, \ell') = \frac{1}{2} \int \theta \mathrm{d}\theta \left[J_0(\ell\theta) A(\ell', \theta) - J_4(\ell\theta) B(\ell', \theta) \right], \tag{6.33}$$

with the functions

$$A(\ell, \theta) = \exp\left(-\frac{\ell^2 \sigma^2(\theta)}{2}\right) \left[J_0(\ell, \theta) + \frac{\ell^2}{2} C_2(\theta) J_4(\ell\theta) \right], \tag{6.34}$$

$$B(\ell, \theta) = \exp\left(-\frac{\ell^2 \sigma^2(\theta)}{2}\right) \left[J_4(\ell, \theta) + \frac{\ell^2}{2} C_2(\theta) J_s(\ell\theta) \right]. \tag{6.35}$$

Here, uncorrelated deflections contained in the variance $\sigma^2(\theta)$ give rise to a Gaussian convolution kernel while correlated deflections due to $C_2(\theta)$ show a more complicated mode-coupling. The abbreviation $J_s(x) = J_2(x) + J_6(x)$ is employed.

In the limit absent lensing, $C_0(\theta) = C_2(\theta) = 0$ such that $W_+(\ell, \ell') = \delta(\ell - \ell')/\ell$ and $W_-(\ell, \ell') = 0$, due to the orthogonality relations of the cylindrical Bessel functions,

$$\int \theta \mathrm{d}\theta \, J_n(\ell\theta) J_n(\ell'\theta) = \frac{1}{\ell} \delta_D(\ell - \ell'). \tag{6.36}$$

In this case, the convolution is reduced to a Dirac δ_D-function and the mixing matrix is the unit matrix, so that the E-mode and B-mode amplitudes are conserved and there is no convolution between ℓ-modes. It could be verified that higher-oder corrections arising in the transformation of correlation functions do have a negligible effect for the evolved ellipticity correlations (Challinor & Lewis 2005, Lewis & Challinor 2006) and in the numerical implementation, the same relations were used for the required number of grid points ($4 \times \ell_{\max}$ tabulated values of $\sigma^2(\theta)$ and $C_2(\theta)$ in θ) as in CMB-lensing.

6.5.4. Conversion between E and B-modes

Fig. 6.3 shows the mode coupling kernels $W_+(\ell, \ell')$ and $W_-(\ell, \ell')$, according to equation **??**, for the high-redshift distribution and computed for a nonlinear CDM spectrum, with qualitatively very similar results for the low redshift sample. Apart from a smooth variation of $W_+(\ell, \ell')$, which acts on the ellipticity spectra by convolution, one notices tall spikes at $\ell = \ell'$, illustrating the closeness to diagonality of the W_+-matrix. In contrast, $W_-(\ell, \ell')$ shows smaller amplitudes by about two orders of magnitude, indicating that the conversion between E- and B-modes is a
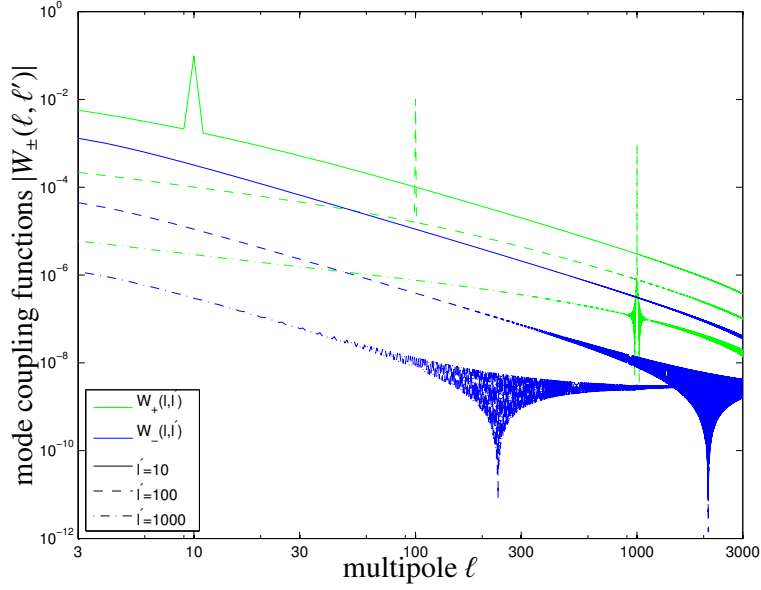
Figure 6.3.: Mode coupling functions $W_+(\ell, \ell')$ (green lines) and $W_-(\ell, \ell')$ (blue lines) used in the transformation of the ellipticity spectra, which describes the convolving effect on the ellipticity spectra, for $\ell' = 10, 100, 1000$ (solid, dashed and dash-dotted, respectively). The coupling functions shown are the ones for the high redshift galaxy sample, while those for the low redshift sample look qualitatively very similar.

minor effect compared to the convolution mediated by $W_+(\ell, \ell')$, with strong oscillatory features close to diagonal $\ell = \ell'$. The kernels $W_\pm(\ell, \ell')$ show an inverse scaling with multipole ℓ such that they become approximately constant when substituted into the relation (7.42) by multiplication with the $\ell' \mathrm{d}\ell'$-differential.

6.6. Lensed ellipticity spectra

The final results are given in Figs. 6.4 and 6.5, which compare the initial ellipticity spectra $C_E^\epsilon(\ell)$ and $C_B^\epsilon(\ell)$ of the ellipticity field as predicted by the angular momentum model, and the evolved spectra $C_E'(\ell)$ and $C_B'(\ell)$ due to peculiar motion. For comparison with weak lensing, the weak convergence spectrum $C_\kappa(\ell)$ expected from the EUCLID galaxy sample is plotted in comparison, for a nonlinear CDM spectrum (using the parameterisation by Smith et al. 2003). The first observation is that ellipticity correlations reach amplitudes similat to those of the weak lensing convergence in the nonlinear part corresponding to amplitudes $\ell \lesssim 300$, and that the intrinsic E-mode spectrum $C_E^\epsilon(\ell)$ is larger than the B-mode spectrum $C_B^\epsilon(\ell)$ by about an order of magnitude in this regime. On larger angular scales, there are no appreciable ellipticity correlations and one effectively observes the variance of the ellipticity field for uncorrelated objects. Consequently, the spectra have identical amplitudes and are effectively constant. In this regime, the shifting
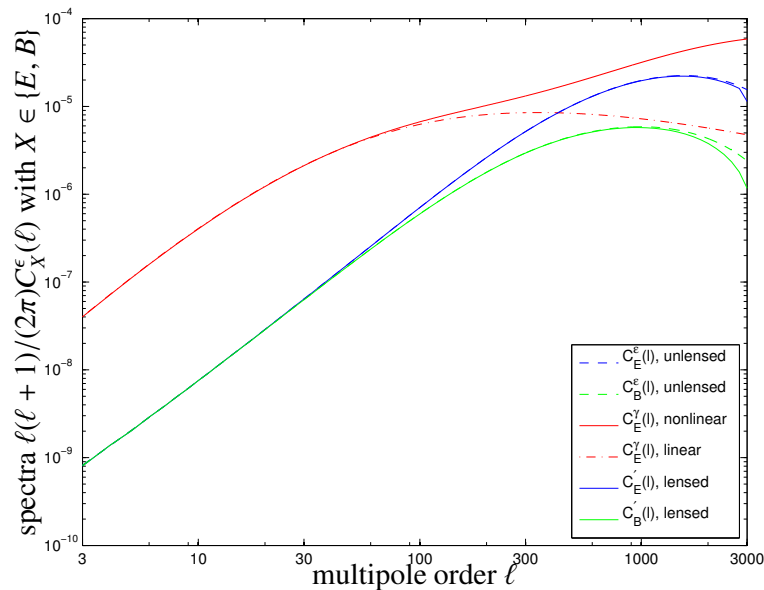
41

Figure 6.4.: Ellipticity spectra $C_E^\epsilon(\ell)$ (blue line) and $C_B^\epsilon(\ell)$ (green line) as predicted by the angular momentum model with $a = 0.25$ and the disk thickness parameter set to $\alpha = 1$ (dashed lines), and the lensed ellipticity spectra (solid lines) where the displacements were computed for the high redshift galaxies. For comparison, the spectrum $C_E^\gamma(\ell)$ of the weak lensing shear γ (red line) is plotted.

effect is not able to affect the galaxies, which is a well-known result in CMB-lensing, where scale free-spectra are invariant (Lewis & Challinor 2006): The mode-conversion mechanism is uneffective if the spectra are equal, $C_E^\epsilon(\ell) = C_B^\epsilon(\ell)$, and the convolution with $W_+(\ell, \ell')$ is not able to redistribute amplitudes. In contrast, both spectra are affected on multipoles $\ell > 1000$, where in particular $C_B^\epsilon(\ell)$ has decreased relative to $C_E^\epsilon(\ell)$. Fig. 6.6 shows the changes in the spectra as a function of multipole l by giving the ratio of the evolved and initial E-mode and B-mode spectra, $C_E'(\ell)/C_E^\epsilon$ and $C_B'(\ell)/C_B^\epsilon$ respectively. As already indicated by Figs. 6.4 and 6.5, there is a significant decrease of amplitude amounting to 5% for the $E-$ and 30% for the B-modes from $\ell = 3000$ on in the case of the high-redshift sample and from $\ell = 1000$ on in the case of the low-redshift sample. This implies that for EUCLID's weak lensing application, changes in the ellipticity spectra are affecting scales where the shape noise starts dominating, but for shallower surveys, lower multipoles would be affected by weak lensing deflection. It can be concluded that in the case of deep surveys such as EUCLID, weak lensing manifests itself primarily as weak lensing shear which dominates over intrinsic alignments and the lensing deflection effect shapes intrinsic alignments by decreasing their amplitudes only at very high multipoles.
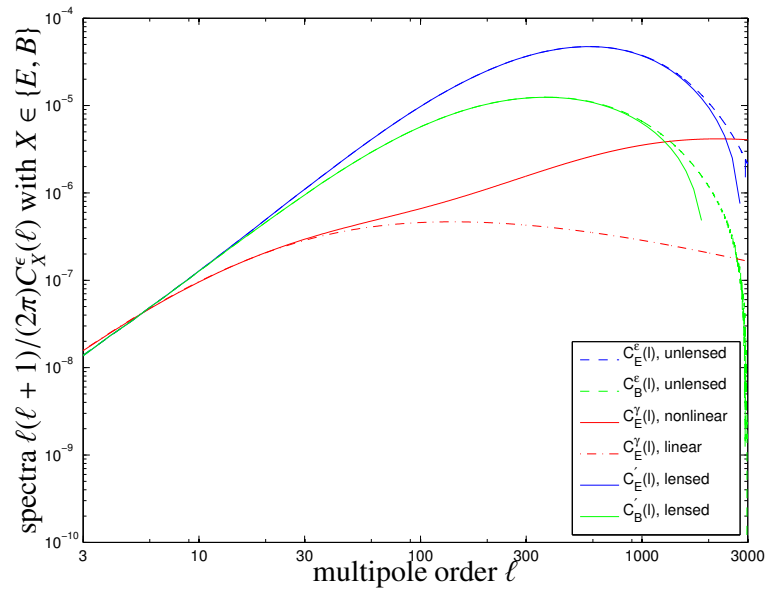
Figure 6.5.: Ellipticity spectra $C_E^\epsilon(\ell)$ (blue line) and $C_B^\epsilon(\ell)$ (green line) as predicted by the angular momentum model (dashed lines), and the lensed ellipticity spectra (solid lines) where the displacements were computed for the low redshift galaxies. For comparison, the spectrum $C_E^\gamma(\ell)$ of the weak lensing shear γ for the same galaxy sample (red line) is shown.
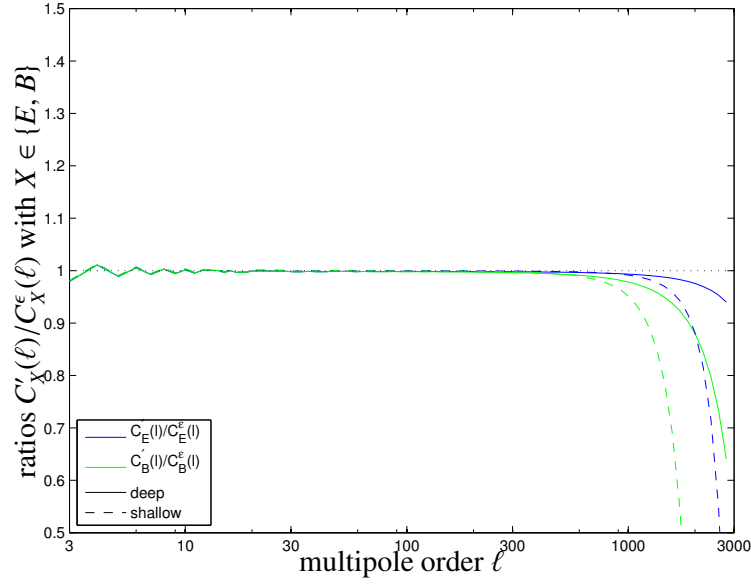
Figure 6.6.: Ratios $C'_E(\ell)/C^\epsilon_E(\ell)$ (blue lines) and $C'_B(\ell)/C^\epsilon_B(\ell)$ (green lines), for both a high redshift galaxy sample (solid lines) and a low redshift galaxy sample (dashed lines).

6.7. Violated homogeneity of the ellipticity field

Lensing of the intrinsic ellipticity field introduces a violation of their statistical homogeneity in complete analogy to the lensing deflection acting on the CMB polarisation. For a given realisation of the deflection potential ψ one can estimate the lensing effect on the ellipticity spectra, $X = E, B$:

$$\langle \epsilon'_X(\ell)\epsilon'_X(\ell') \rangle = f_X(\ell, \ell')\psi(\ell - \ell') \tag{6.37}$$

with

$$\begin{aligned}
f_E(\ell, \ell') &= \left(\ell \delta_\ell C^\epsilon_E(\ell) + \ell' \delta_\ell C^\epsilon_E(\ell - 1) \right) \cos 2\varphi_{\ell,\ell'} \\
f_B(\ell, \ell') &= \left(\ell \delta_\ell C^\epsilon_B(\ell) + \ell' \delta_\ell C^\epsilon_B(\ell - 1) \right) \cos 2\varphi_{\ell,\ell'}
\end{aligned} \tag{6.38}$$

where $\varphi_{\ell,\ell'}$ denotes the enclosed angle. Nonzero correlations between multipoles are the signature of homogeneity violation introduced by a single realisation and they would disappear in the process of ensemble averaging the lensing potential.

In order to place an upper limit on this effect a particularly simple geometry is selected, namely parallel alignment of the wave vectors ℓ and ℓ' such that the cosines are equal to one and have the wave vectors them differ by one unit, $\ell - \ell' = 1$, as the coupling between neighbouring multipoles is strongest due to the rapid decline of the lensing potential's Fourier transform with increasing ℓ. In this limit, and if one assumes the ellipticity spectra to be slowly varying, the ratio between the off-diagonal and diagonal correlations is given by

$$\frac{C'_E(\ell, \ell + 1)}{C^\epsilon_E(\ell)} = \frac{C'_B(\ell, \ell + 1)}{C^\epsilon_B(\ell)} = \frac{\ell}{2\pi^2}\sigma_\psi(\ell = 1), \tag{6.39}$$
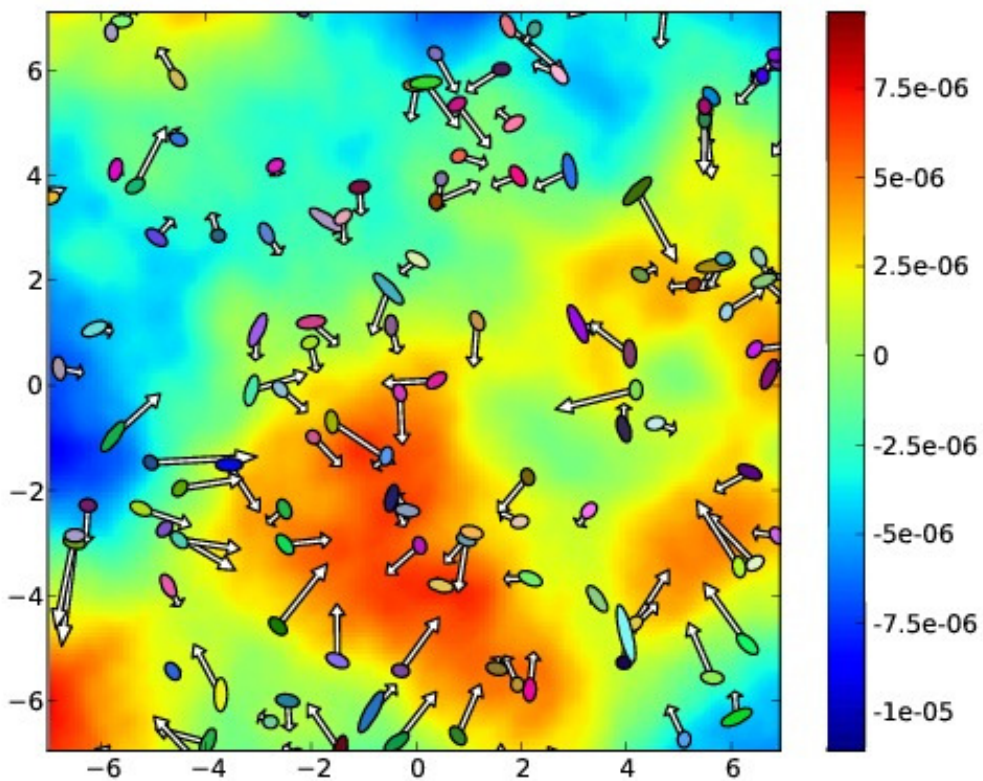
Figure 6.7.: Realisation of a lensing potential on a $14° \times 14°$-patch with 100 randomly sampled galaxies. The ellipticity is given by the lensing shear and the arrow indicates the apparent shift due to the weak lensing deflection. The realisation uses a lensing potential for the high-redshift galaxy sample with dominating shear.

where σ_ψ is substituted as an order of magnitude estimate for a typical amplitude of the lensing potential. Substituting numbers yields upper limits of 10% for the off-diagonal correlation relative to the diagonal ones at $\ell = 10^3$ which is smaller than the weak lensing shear at high redshifts, but comparable if not slightly larger than the lensing shear at low redshifts.

As the imprints of weak lensing on the intrinsic ellipticity pattern are basically identical to those in the case of lensing of the CMB polarisation, it is conceivable that the lensing deflection field can be estimated by measuring the amount of off-diagonal (meaning $\ell \neq \ell'$) spectra of the ellipticity modes as illustrated above, by applying the reconstruction technique worked out by Hu and Okamoto: With a model for intrinsic ellipticity spectra (which can be well predicted using a good prior on Ω_m, σ_8, a and α) the statistics of the lensing deflection field can be inferred from broken homogeneity. In contrast to polarisation tensors, however, the ellipticity field is strongly shaped by shear and only in extreme cases such as a low-redshift galaxy sample at large multipoles the intrinsic alignment effects are dominant, where of course issues with the low surface density of lensing galaxies and the corresponding high Poisson-noise become important. For illustration, Fig. 6.7 shows a realisation of the lensing potential with derived lensing deflections as gradients of the potential. The second derivatives have been used for generating a shear field that is depicted as a shape distortions of the otherwise circular spots. For visualisation, the deflections have been enlarged by a factor of 100 and the shear has been multiplied by 10.

6.8. Summary

The subject of this study was an investigation of lensing effects and their observable signatures if the lensed galaxy sample shows intrinsic ellipticity correlations. Apart from weak lensing shear that operates on the shape of galaxies there will be a lensing deflection, which is unobservable in the case of uncorrelated ellipticities, but generates observable signatures if the lensing galaxies are intrinsically shape correlated. The lensing deflection manifests itself in the ellipticity spectra in three distinct ways: Firstly, there is a loss of amplitude in the spectra at high multipoles, secondly one can observe a redistribution of amplitude between the E-mode and B-mode spectra, and thirdly there will be correlations between adjacent multipoles. In deriving these effects heavy use of analogies to the theory of lensing of the cosmic microwave background polarisation and identical mathematical properties of the ellipticity-polarisation tensors has been made. In this investigation, the forecasts for a high-redshift lensing survey such as EUCLID with a low-redshift galaxy sample are compared in order understand the scaling behaviour of all effects with distance.

(i) The ellipticity E-mode and B-mode spectra are derived from a physical alignment model due to Crittenden et al. (2001). This model is quadratic in the tidal shear and applicable for describing shape correlations between isolated spiral galaxies. Due to the lack of an analytical description of how a galactic disk is oriented inside a dark matter halo one can think of the spectra as upper limits as perfect alignment of the symmetry axis of the galactic disk with the host halo's angular momentum direction is assumed. The two parameters that enter this ellipticity model, the alignment parameter a and the disk thickness α, are determined from numerical simulations and from observations of local galaxies.

(ii) The impact of lensing deflection on intrinsically shape-correlated galaxies is threefold: There is a smoothing of the intrinsic ellipticity spectra, a mixing in multipole and a conversion between *E*-modes and *B*-modes, and the generation of correlations between otherwise uncorrelated multipoles, as an expression of violated homogeneity of the lensed galaxy field.

(iii) By drawing analogies between galaxy ellipticities and the CMB-polarisation, namely that both are tensorial fields with spin-2, one can formulate transformation formulas for the ellipticity spectra, if individual galaxies have been coherently shifted to a new position by lensing. The transformation formula can be written concisely as a combined convolution and mode-mixing relation.

(iv) Lensing deflection operates on intrinsic ellipticity spectra by convolution. Correlation amplitudes are redistributed in multipoles which can be observed on small angular scales when intrinsic alignment spectra cease to be constant and drop in amplitude. Then, lensing causes the spectra to drop faster. Qualitatively, these effects are weak at high redshifts and dominated by far by the weak shear signal, but are sizable at low redshifts, where the weak lensing shear is small. In this case, weak lensing can actually weaken shape-correlations by random redistribution of intrinsically aligned galaxies.

(v) The losses in amplitude amount roughly to 5% in $C_E^\epsilon(\ell)$ and to 30% in $C_B^\epsilon(\ell)$ at $\ell = 3000$ in the case of the high redshift sample and at $\ell = 1000$ in the case of the low redshift sample. Compared to the convolution of the spectra the conversion between *E*- and *B*-modes is a minor effect.

(vi) An upper limit on the correlation between different multipoles due to broken homogeneity has been derived by using the fact that the correlations with between adjacent multipoles should be strongest. These correlations can be estimated to be at most $\sim 10\%$ of the spectra at the largest multipoles, both for *E*- and *B*-modes, and are proportional to ℓ.

(vii) Although it has been taken advantage of formal analogies between the CMB-polarisation and ellipticity fields, concerning symmetry properties, the description with spectra and the incorporation of the lensing effect it is worth to emphasise that in contrast to the CMB, lensing does not introduce a bispectrum into the ellipticity correlations. The CMB-lensing bispectrum is sourced by the integrated Sachs-Wolfe effect in the same potential that causes the lensing-deflection, and there is no analogous mechanism in the case of galaxy ellipticities.

It can be concluded that for deep-reaching lensing surveys intrinsic alignments are subdominant and that the shaping of their correlations by weak lensing deflection (and by peculiar motion, which is of a similar order of magnitude, see Giahi & Schäfer 2012) is small compared to gravitational shear. At low redshifts, however, the situation is inverted: Intrinsic alignments dominate and the most important lensing effect is deflection. In contrast to the CMB-polarisation, it is doubtful if a violation of homogeneity of the ellipticity field introduced by lensing can be observed.

Note

The results of this chapter are the basis of Giahi-Saravani & Schaefer (2013) and have been accepted for publication.

7. Evolution of intrinsic alignments

7.1. Introduction

A common assumption in weak cosmic lensing is that galaxy ellipticities are intrinsically uncorrelated and that the only correlating effect is weak lensing, because the light from neighbouring galaxies has to transverse the same cosmic tidal fields, leading to a correlation in change in shape. This assumption, however, is challenged on small scales by intrinsic alignment effects (for a review on angular momentum models and intrinsic alignments, see Schäfer 2009). Tidal shearing models for angular momentum build-up in galactic haloes predict correlated angular momenta of neighbouring galaxies. If the symmetry axis of the galactic disc is aligned with the angular momentum direction of the host halo, neighbouring galaxies are viewed under correlated angles of inclination such that their ellipticities appear correlated. This intrinsic alignment effect is important on small scales because the angular momentum correlation is comparatively short ranged: it is predicted to be present on scales of about 1 Mpc h^{-1} (Crittenden et al. 2001, Natarajan et al. 2001, Schäfer & Merkel 2012). Intrinsic alignments of galaxies based on angular momentum models are a relatively new topic which will undoubtedly attract much interest in the future as the weak lensing data sets provided by large-scale lensing observations will at the same time help to scrutinise intrinsic alignment models. The theory of angular momentum-induced alignments (Croft & Metzler 2000, Crittenden et al. 2001, 2002, Mackey et al. 2002) has been applied to describe contamination of weak lensing data in the convergence spectrum (Heavens et al. 2000, Heymans & Heavens 2003, Heymans et al. 2004, 2006) and bispectrum (Semboloni et al. 2008). Different schemes for removing the contamination of intrinsic alignments have been proposed, from discarding close galaxy pairs (King & Schneider 2002, 2003) to specifically designed weighting schemes for nulling out their contribution (Joachimi & Schneider 2008) or amplifying them relative to the weak lensing-induced ellipticity correlations (King & Schneider 2003, Joachimi & Schneider 2010). Resulting biases on cosmological parameter estimation if intrinsic alignments remain uncorrected have been quantified (Bridle & King 2007, Joachimi & Bridle 2010, Kirk et al. 2010, Schneider & Bridle 2010).

The wealth of structure in the angular momentum and ellipticity field and their alignment with large-scale tidal fields has attracted much interest from the numerical perspective (Hahn et al. 2007, Codis et al. 2012) and suggests the question if large-scale tidal fields can be reconstructed using the ellipticity field as a tracer (Lee & Pen 2000, 2001, 2007). On a more fundamental level, the investigation of tidal shearing mechanisms in different orders of perturbation theory along with the deformation of forming haloes due to tidal forces has been done by Catelan & Theuns (1996a), Catelan (1995), Catelan et al. (2001), Catelan & Theuns (1996b), Catelan et al. (1995), Catelan & Porciani (2001) and (Lee & Pen 2008). Numerical verification of the tidal torquing theories of angular momentum build-up has been the topic of a number of papers (Bullock et al. 2001, Catelan & Porciani 2001, Porciani et al. 2002b, Hahn et al. 2007) who agree that the

angular momentum direction can be well described by tidal torquing whereas the amount of angular momentum might be overestimated. Because ellipticity alignments are only sensitive to the angular momentum direction, these studies provide support for using tidal torquing models with this particular application in mind. The way in which the orientation of a galactic disc is linked to the angular momentum direction of the host halo is not very clearly cut. In a small number of simulations (Bailin et al. 2005) found mismatches and suggest that direct linking of the symmetry axis of the disc to the host halo angular momentum would lead to overestimation of the ellipticity alignments. Until a better description of how large this misalignments can be and a modelling with known parameters similarly to the relation between tidal shear and angular momentum direction is available, the derived ellipticity spectra are considered as upper limits. By now, intrinsic alignments of spiral galaxies have been measured in a number of data sets and have been found at the expected levels (Pen et al. 2000, Lee & Pen 2002, Mandelbaum et al. 2006, Hirata et al. 2007), although some studies doubt these claims (e.g. Andrae & Jahnke 2011, Mandelbaum et al. 2011). The point which motivated this paper is the comparatively short-ranged correlation of angular momenta and consequently of the galaxy ellipticities, which reaches out to distances of about 1 Mpc h^{-1}. If the ellipticity field is this short-ranged, and if it is distorted by the peculiar motion of galaxies, by how much do the correlations change and on what scales? I will investigate this question by employing a formalism based on lensing of the cosmic microwave background (CMB) polarization (Seljak 1996a, Hu 2000, Challinor & Lewis 2005, Lewis & Challinor 2006), by describing peculiar motion with Lagrangian perturbation theory (LPT) and consider the Euclid galaxy sample as an application. After a summary of cosmology, structure formation, LPT, angular momentum models and ellipticity correlations in Section 2, the formalism and the results are described in Section 3. The main findings are summarized in Section 4. As reference model a spatially flat w cold dark matter (wCDM) model is chosen with Gaussian adiabatic initial perturbations in the CDM distribution. Specifically, parameters were chosen to be $\Omega_m = 0.25$, $n_s = 1$, $\sigma_8 = 0.8$, $\Omega_b = 0.04$ and finally $H_0 = 10^5\,h\,\mathrm{ms}^{-1}\mathrm{Mpc}^{-1}$, with $h = 0.72$. The dark energy equation of state is set to $w = -0.95$ and the sound speed is equal to the speed of light, $c_s = c$, such that there is no dark energy clustering. The derivations will assume the flat-sky approximation in the computation of ellipticity spectra and for deriving angular displacements and their statistical properties, and likewise in the adaptation of the CMB-lensing formalism.

7.2. Cosmology

7.2.1. Dark energy cosmologies

The time evolution of isotropic Friedmann-universe with homogeneous dark matter and dark energy is described by the Hubble function $H(a) = \mathrm{d}\ln a/\mathrm{d}t$, which is given by

$$\frac{H^2(a)}{H_0^2} = \frac{\Omega_m}{a^3} + (1 - \Omega_m)\exp\left(3\int_a^1 \mathrm{d}\ln a\,(1 + w(a))\right), \qquad (7.1)$$

with the matter density parameter Ω_m and the dark energy equation of state function $w(a)$. Spatial flatness requires the dark energy density to be $1 - \Omega_m$. The comoving distance χ can be computed

from the scale factor a,

$$\chi = c \int_a^1 \frac{\mathrm{d}a}{a^2 H(a)}. \tag{7.2}$$

For the galaxy redshift distribution $n(z)\mathrm{d}z$ a standard shape,

$$n(z) = n_0 \left(\frac{z}{z_0}\right)^2 \exp\left(-\left(\frac{z}{z_0}\right)^\beta\right)\mathrm{d}z \quad \text{with} \quad \frac{1}{n_0} = \frac{z_0}{\beta}\Gamma\left(\frac{3}{\beta}\right), \tag{7.3}$$

is used with $\beta = 3/2$. z_0 is chosen such that the distribution has a median redshift of 0.9 corresponding to EUCLID which will be contrasted with a galaxy distribution of identical shape but with a much lower median of 0.3. This work will refer to the two application cases as the high and low redshift galaxy sample, respectively. The distribution can be rewritten in terms of comoving distance using the relation $p(z)\mathrm{d}z = p(\chi)\mathrm{d}\chi$ with $\mathrm{d}z/\mathrm{d}\chi = H(\chi)/c$.

7.2.2. CDM power spectrum

The CDM power spectrum P_δ describes the wavelength dependence of the density correlations. For the statistically homogeneous Gaussian density field δ the power spectrum is defined in Fourier space as

$$\langle \delta(\boldsymbol{k})\delta(\boldsymbol{k}')\rangle = (2\pi)^3 \delta_D(\boldsymbol{k} + \boldsymbol{k}')P_\delta(k), \tag{7.4}$$

in a sufficiently flat space. For the shape of the power spectrum the following Ansatz is used Bardeen et al. (1986):

$$P_\delta(k) \propto k^{n_S} T^2(k), \tag{7.5}$$

with $T(k)$ being a transfer function approximated by

$$T(q) = \frac{\ln(1 + 2.34q)}{2.34q}\left(1 + 3.89q + (16.1q)^2 + (5.46q)^3 + (6.71q)^4\right)^{-\frac{1}{4}}, \tag{7.6}$$

and $k = q\Gamma$ measured in units of the shape parameter (Sugiyama 1995)

$$\Gamma = \Omega_m h \exp\left[-\Omega_b\left(1 + \frac{\sqrt{2h}}{\Omega_m}\right)\right]. \tag{7.7}$$

The amplitude of P_δ is normalized on the scale $R = 8$ Mpc/h to the variance σ_8,

$$\sigma_R^2 = \int \frac{k^2 \mathrm{d}k}{2\pi^2} P_\delta(k) W^2(kR), \tag{7.8}$$

with a Fourier transformed spherical top hat filter function $W(x) = 3j_1(x)/x$, and j_1 denoting the spherical Bessel function of the first kind of order ℓ (Abramowitz M. 1972).

7.2.3. Linear structure growth

The growth of the density field in the linear regime, $\delta(\boldsymbol{x}, a) = D_+(a)\delta(\boldsymbol{x}, a = 1)$, is given by the growth function $D_+(a)$, which follows as a solution to the growth equation (Carroll et al. 1992, Turner & White 1997, Wang & Steinhardt 1998, Linder & Jenkins 2003)

$$\frac{\mathrm{d}^2}{\mathrm{d}a^2}D_+ + \frac{1}{a}\left(3 + \frac{\mathrm{d}\ln H}{\mathrm{d}\ln a}\right)\frac{\mathrm{d}}{\mathrm{d}a}D_+ = \frac{3}{2a^2}\Omega_m D_+, \tag{7.9}$$

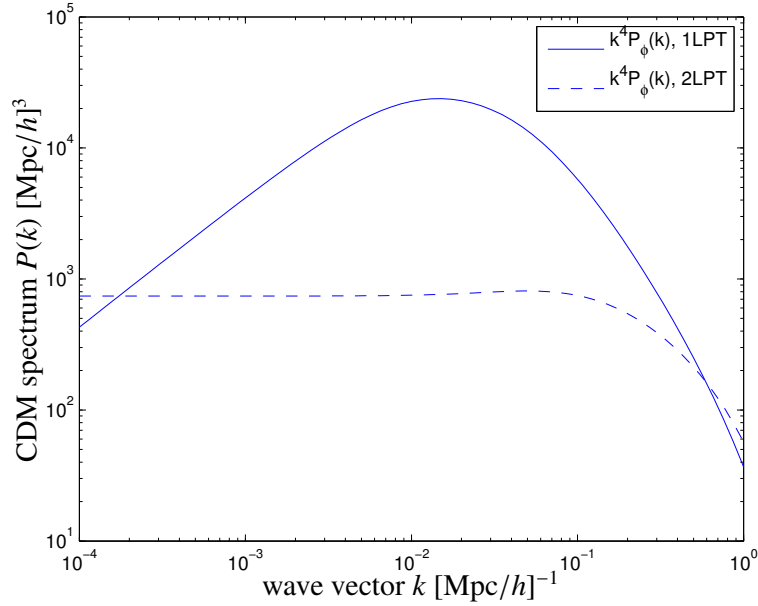under Newtonian gravity in the linear regime.

Figure 7.1.: CDM spectra $k^4 P_\Phi(k) \equiv P(k)$ which are employed in LPT for displacing the galaxies, for 1LPT (solid line) and 2LPT (dashed line). The 1LPT result corresponds in this representation to the CDM spectrum $P(k)$, $k^4 P_\Phi^{(1)} = P(k)$.

7.2.4. Nonlinear growth and Lagrangian perturbation theory (LPT)

The peculiar motion of galaxies can be described using Lagrangian perturbation theory (LPT) if the flow of dark matter and of the advected galaxies is irrotational and nonlinearities are weak. In this limit, galaxies follow straight lines given by the gradient of the Lagrangian potential Φ_1 to first order LPT (1LPT) (Doroshkevich 1970, Zel'Dovich 1970, Buchert 1989, Moutarde et al. 1991, Bernardeau et al. 2002),

$$\boldsymbol{x} \rightarrow \boldsymbol{x} - D_1(a)\nabla\Phi_1, \tag{7.10}$$

where the Lagrangian potential Φ_1 is the solution to the Poisson equation,

$$\nabla^2\Phi_1 = \delta. \tag{7.11}$$

During linear structure growth, the Lagrangian potential Φ_1 is proportional to the true gravitational potential, the proportionality constant being $3\Omega_\mathrm{m}/2/\chi_H^2 \, D_+(a)/a$. The trajectory can be improved by adding second-order corrections to LPT (2LPT) (Melott et al. 1994),

$$\boldsymbol{x} \rightarrow \boldsymbol{x} - D_1(a)\nabla\Phi_1 + D_2(a)\nabla\Phi_2 \tag{7.12}$$

with the second-order Lagrangian potential Φ_2,

$$\nabla\Phi_2 = \sum_{\alpha>\beta} \left[\Phi_{1,\alpha\alpha}\Phi_{1,\beta\beta} - \Phi_{1,\alpha\beta}\Phi_{1,\beta\alpha} \right], \tag{7.13}$$

with

$$\Phi_{1,\alpha\beta} = \frac{\partial^2 \Phi_1}{\partial x_\alpha \partial x_\beta}. \tag{7.14}$$

The time dependence are given by $D_1(a) = D_+(a)$ and $D_2(a) = -3/7D_+^2(a)\Omega_m^{-1/143}$ (for a low-Ω_m cosmology with a cosmological constant Λ, see Bouchet et al. (1992)). The solution to the latter relation can be written down in Fourier space, where products of Lagrangian potentials and their derivatives become convolutions,

$$\Phi_2 = -\frac{1}{k^2} \int \frac{d^3 k'}{(2\pi)^3} \sum_{i>j} Q_{ij}(\boldsymbol{k}, \boldsymbol{k}')\delta(\boldsymbol{k}')\delta(\boldsymbol{k} - \boldsymbol{k}'), \tag{7.15}$$

where the mode coupling function $Q_{ij}(\boldsymbol{k}, \boldsymbol{k}')$ is given by

$$Q_{ij}(\boldsymbol{k}, \boldsymbol{k}') = \frac{(\boldsymbol{k}')_i^2(\boldsymbol{k}' - \boldsymbol{k})_j^2 - \boldsymbol{k}_i\boldsymbol{k}_j(\boldsymbol{k} - \boldsymbol{k}')_i(\boldsymbol{k} - \boldsymbol{k}')_j}{(\boldsymbol{k}')^2(\boldsymbol{k} - \boldsymbol{k}')^2}. \tag{7.16}$$

The spectra of the Lagrangian potentials Φ_1 and Φ_2 can be defined by

$$\langle \Phi_i(\boldsymbol{k})\Phi_i(\boldsymbol{k}') \rangle = (2\pi)^3 \delta_D(\boldsymbol{k} + \boldsymbol{k}')P_\Phi^{(i)}(k), \quad i = 1, 2, \tag{7.17}$$

with $P_\Phi^{(1)}(k) = P(k)/k^4$ as a consequence of the Poisson equation and with $P_\Phi^{(2)}(k)$ which can be derived to follow

$$P_\Phi^{(2)} = \frac{2}{k^4} \int \frac{d^3 k'}{(2\pi)^3} \left(\sum_{i>j} Q_{ij}(\boldsymbol{k}', \boldsymbol{k} - \boldsymbol{k}') \right)^2 P(|\boldsymbol{k}'|)P(|\boldsymbol{k} - \boldsymbol{k}'|) \tag{7.18}$$

by application of the Wick theorem (for a proof, see Durrer (2008)). The integration is most efficiently carried out using cylindrical coordinates aligned with k such that $d^3 k = 2\pi(k')^2 dk' d\cos\theta$ using azimuthal symmetry, with θ being the angle between $\boldsymbol{k}$ and $\boldsymbol{k}'$. Fig. 7.1 gives an impression of the spectrum $P_\Phi^{(1)}(k)$ and of the 2LPT corrections $P_\Phi^{(2)}(k)$ relative to 1LPT, where $k^4 P_\Phi^{(i)}(k), i = 1, 2$ is plotted, which is equal to the CDM spectrum $P(k)$ for the 1LPT result due to the Poisson equation. The 2LPT spectrum is smaller on almost all scales by up to an order of magnitude and is only similar in amplitude on spatial scales of about 1 Mpc h^{-1}.

7.3. Galaxy formation and ellipticities

7.3.1. Intrinsic ellipticity correlations from angular momenta of the host halos

In this work, it is assumed that the halo angular momentum axis and the symmetry axis of the galactic disk are parallel. The tilting of the disk relative to the line of sight determines the aspect ratio under which the galactic disk is viewed and therefore the galaxy's ellipticity. In this way, the angular momentum direction $\hat{L} = \boldsymbol{L}/L$ with $L = |\boldsymbol{L}|$ determines the ellipticity ϵ. In this picture, ellipticity correlations are derived from angular momentum direction correlations and ultimately from tidal shear correlations (Heavens et al. 2000, Crittenden et al. 2001, 2002, Mackey et al.

2002, Heymans & Heavens 2003). Specifically, the two components of the ellipticity field can be combined to form the complex ellipticity with ϵ_+ as the real and $\epsilon_\times$ as the complex part, and related to the angular momentum direction $\hat{L}$:

$$\epsilon = \epsilon_+ + \mathrm{i}\epsilon_\times \quad \text{with} \quad \epsilon_+ = \alpha\frac{\hat{L}_x^2 - \hat{L}_y^2}{1 + \hat{L}_z^2}, \quad \epsilon_\times = 2\alpha\frac{\hat{L}_x\hat{L}_y}{1 + \hat{L}_z^2}, \tag{7.19}$$

when the coordinate system is aligned with its *z*-axis parallel to the line of sight. Under a rotation of the coordinate frame by an angle φ the complex ellipticity transforms according to the relation $\epsilon \rightarrow \exp(2\mathrm{i}\varphi)\epsilon$, in accordance with the spin-2 property of the ellipticity field. α is the disk thickness parameter and can be used for describing a weaker dependence of ϵ on $\hat{L}$ if the galactic disk has a finite thickness. In this thesis, the numerical value $\alpha = 0.75$, which has been measured in the APM galaxy sample by Crittenden et al. (2001), is used.

Linking the ellipticity components ϵ_+ and $\epsilon_\times$ to the angular momentum direction $\hat{L}$ and ultimately to the tidal shear tensor by means of the conditional probability density $p(\boldsymbol{L}|\Phi_{,\alpha\beta})\mathrm{d}\boldsymbol{L}$ provides means to derive ellipticity correlations in terms of tidal shear correlations, and ultimately as functions of the CDM-spectrum. Because the ellipticity correlations of galaxies are of interest here, the CDM-spectrum is smoothed with a Gaussian filter on the mass-scale $3 \times 10^{11} M_\odot/h$. In this way, one can write down a 3-dimensional correlation function of the ellipticity field as a function of moments $\zeta_n(r)$ (see Crittenden et al. 2001) of the CDM-spectrum and finally to carry out a Limber projection for obtaining the angular correlation function of the ellipticity field.

7.3.2. Angular momentum from tidal shearing

Angular momentum generation in CDM-haloes is a Lagrangian perturbative process (Hoyle 1949, Sciama 1955, Peebles 1969, Doroshkevich 1970, White 1984): The variation of velocities displacing a protogalactic region acts as a torque which generates angular momentum L_α:

$$L_\alpha = a^3 H(a)\frac{\mathrm{d}D_+}{\mathrm{d}a}\epsilon_{\alpha\beta\gamma}I_{\beta\delta}\Phi_{,\delta\gamma}, \tag{7.20}$$

with the tidal shear being defined as the Hessian of the gravitational potential and the inertia tensor measuring the second moments of the mass distribution inside the protohalo,

$$\Phi_{,\delta\gamma} \equiv \frac{\partial^2\Phi}{\partial x_\delta\partial x_\gamma} \quad \text{and} \tag{7.21}$$

$$I_{\beta\delta} \equiv \Omega_\mathrm{m}\rho_\mathrm{crit}\int \mathrm{d}^3q\ \delta(\boldsymbol{q})(\boldsymbol{q} - \bar{\boldsymbol{q}})_\beta(\boldsymbol{q} - \bar{\boldsymbol{q}})_\delta, \tag{7.22}$$

respectively, with implicit summation over repeated indices. $\boldsymbol{q}$ are Lagrangian coordinates moving along with the halo's centre of gravity $\bar{\boldsymbol{q}}$.

This relation reflects the interesting requirement of misalignments between the shear and inertia eigensystems which is necessary for angular momentum generation: Only the antisymmetric tensor $X_{\beta\gamma}^- = \sum_\delta(I_{\beta\delta}\Phi_{,\delta\gamma} - \Phi_{,\beta\delta}I_{\delta\gamma})/2$ is relevant for the angular momentum (Merkel & Schäfer 2011), $L_\alpha \propto X_{\beta\gamma}^-$, because the contraction of the symmetric contribution $X_{\beta\gamma}^+$ with the antisymmetric $\epsilon_{\alpha\beta\delta}$ vanishes. The antisymmetric tensor X_- is equal to the commutator $[I_{\beta\delta}, \Phi_{,\delta\gamma}]$ which

suggests that the tidal shear and the inertia are not allowed to be simultaneously diagonalisable and must not have a common eigensystem, otherwise angular momentum can not arise.

In this work the angular momentum-based ellipticity correlation model proposed by Crittenden et al. (2001) is used. There, ellipticities are set into relation to tidal shear by means of a conditional probability distribution $p(L|\Phi_{,\alpha\beta})\mathrm{d}L$. Such a distribution has been proposed by Lee & Pen (2001) as being Gaussian with the covariance

$$\mathrm{cov}(L)_{\alpha\beta} \propto \frac{1}{3}\left(\frac{1+a}{3}\delta_{\alpha\beta} - a\,(\hat{\Phi}^2)_{\alpha\beta}\right), \tag{7.23}$$

which acquires a dependence on the tidal shear tensor, that has been normalised and made trace-free, $\mathrm{tr}(\hat{\Phi}) = 0$ and $\mathrm{tr}(\hat{\Phi}^2) = 1$. In this way, the variance of the angular momentum field varies with the tidal shear, and the randomness of the angular momentum field is controlled by the misalignment parameter a, which describes the average orientation of the protohalo's inertia to the tidal shear eigensystem. a has been measured in numerical simulation to be the value $\simeq 0.25$ for galactic halos.

This description is valid on scales where the correlations between inertia tensors are negligible and is sufficient because the focus of this thesis is on the angular momentum direction. Therefore, one does not need the variance $\langle L^2 \rangle$ of the angular momentum field as a parameter and it is possible to marginalise the distribution over the magnitude L,

$$p(\hat{L}|\Phi_{,\alpha\beta}) = \int L^2 \mathrm{d}L\; p(L|\Phi_{,\alpha\beta}). \tag{7.24}$$

In this picture correlations between angular momenta can be traced back to correlations between tidal shears that neighbouring galaxies experienced in building up their angular momenta.

7.3.3. Intrinsic galaxy ellipticity correlations

Ellipticity correlations between galaxies are traced back to correlated angular momenta of their host haloes. CDM haloes acquire their angular momentum by tidal shearing, and due to the fact that neighbouring galaxies experience correlated tidal fields, their angular momenta are correlated in consequence. The angular momentum, L, in turn determines the angle of inclination at which the galactic disc is viewed, and ultimately the ellipticity ϵ (Heavens et al. 2000, Crittenden et al. 2001, 2002, Mackey et al. 2002, Heymans & Heavens 2003). Specifically, the two components of the ellipticity field can be combined to form the complex ellipticity with ϵ_+ as the real and ϵ_x as the complex part, and related to the angular momentum direction $\hat{L}$:

$$\epsilon = \epsilon_+ + \mathrm{i}\epsilon_\times \quad \text{with} \quad \epsilon_+ = \alpha\frac{\hat{L}_x^2 - \hat{L}_y^2}{1 + \hat{L}_z^2}, \quad \epsilon_\times = 2\alpha\frac{\hat{L}_x\hat{L}_y}{1 + \hat{L}_z^2}, \tag{7.25}$$

with the angular momentum direction $\hat{L} = L/L$ and the coordinate system being aligned with its $z-axis$ chosen to be parallel to the line of sight. A rotation of the coordinate frame by *phi* cuases the complex ellipticity to rotate twice as fast, $\epsilon\exp(2i\phi)\epsilon$, in accordance with the spin-2 property of the ellipticity field. α is a free parameter weakening the dependence between inclination angle and ellipticity for thick galactic discs and has been determined to be $\alpha = 0.75$ in the Automatic Plate Measuring facility (APM) sample Crittenden et al. (2001).

In this work an angular momentum-based ellipticity correlation model is used which is proposed by Crittenden et al. (2001), who trace ellipticity correlations back to tidal shear correlations using the conditional probability distribution $p(\boldsymbol{L}|\Phi_{\alpha\beta})\mathrm{d}\boldsymbol{L}$ is assumed as being Gaussian which is then being marginalized over the magnitude of the angular momentum vector, retaining only its directional dependence. Writing down the ellipticity components as a function of the angular momentum direction and employing the covariance $\langle L_\alpha L_\beta \rangle$ as a function of the squared tidal shear tensor, as advocated by Lee and Pen, it is possible to relate the tidal shear correlations to the spectrum of the density field. With this relation, one can derive a correlation function of the ellipticity field as a function of moments $\zeta_n(r)$ (Crittenden et al. 2001) of the tidal shear field and finally to carry out a Limber projection for obtaining the angular correlation function.

Ellipticity correlations between two poinds $\boldsymbol{\theta}_1$ and $\boldsymbol{\theta}_2$, seperated by the distance θ are described in terms of two correlation functions $\xi_\pm(\theta)$,

$$\xi_+(\theta) = \langle \epsilon^*(\boldsymbol{\theta}_1)\epsilon(\boldsymbol{\theta}_2) \rangle = \langle \epsilon_+(\boldsymbol{\theta}_1)\epsilon_+(\boldsymbol{\theta}_2) \rangle + \langle \epsilon_x(\boldsymbol{\theta}_1)\epsilon_x(\boldsymbol{\theta}_2) \rangle \tag{7.26}$$

$$\xi_-(\theta) = \langle \epsilon(\boldsymbol{\theta}_1)\epsilon(\boldsymbol{\theta}_2) \rangle = \langle \epsilon_+(\boldsymbol{\theta}_1)\epsilon_+(\boldsymbol{\theta}_2) \rangle - \langle \epsilon_x(\boldsymbol{\theta}_1)\epsilon_x(\boldsymbol{\theta}_2) \rangle, \tag{7.27}$$

which are formed from the variances of the ellipticity components ϵ_+ and ϵ_x using $\langle \epsilon_+\epsilon_x \rangle = 0$. They can be transformed to the spectra $C_E^\epsilon(\ell)$ and $C_B^\epsilon(\ell)$ of the gradient and vorticity modes of the ellipticty field,

$$C_E^\epsilon(\ell) = \pi \int \theta \mathrm{d}\theta \left[\xi_+(\theta)J_0(\ell\theta) + \xi_-(\theta)J_4(\ell\theta) \right] \tag{7.28}$$

$$C_B^\epsilon(\ell) = \pi \int \theta \mathrm{d}\theta \left[\xi_+(\theta)J_0(\ell\theta) - \xi_-(\theta)J_4(\ell\theta) \right], \tag{7.29}$$

by Fourier transform (Kaiser 1992, Schneider et al. 2002, Schneider & Kilbinger 2007, Fu & Kilbinger 2010). Concerning the model parameters in this description of intrinsic alignments in spiral galaxies it should be noted that the model employed in this work relies on the disc thickness parameter α (for which the value 0.75 from the APM sample is used), and the misalignment parameter a for describing the variance of the angular momentum direction for a given tidal shear (with the value 0.25 derived from numerical simulations). In this thesis potential misalignments between the symmetry axis of the disc and the host halo angular momentum direction, which are likely to weaken ellipticity correlations, are not modelled. Being local processes, they will enter the ellipticity spectra as prefactors <1. Due to the fact that the formalism used for deriving changes to the ellipticity spectra due to peculiar motion is linear in the spectra, the basic conclusions such as relative changes in the spectra would be unaffected. Other quadratic alignment models, such as that proposed by Mackey et al. (2002), predict significantly smaller amplitudes for intrinsic alignments.

7.4. Angular displacement spectrum

By drawing analogies between the peculiar motion of galaxies causing displacements in the ellipticities, $\epsilon(\theta) \rightarrow \epsilon(\theta + \alpha)$, and the lensing of the polarization of the CMB, $P(\theta) \rightarrow P(\theta + \alpha)$, it
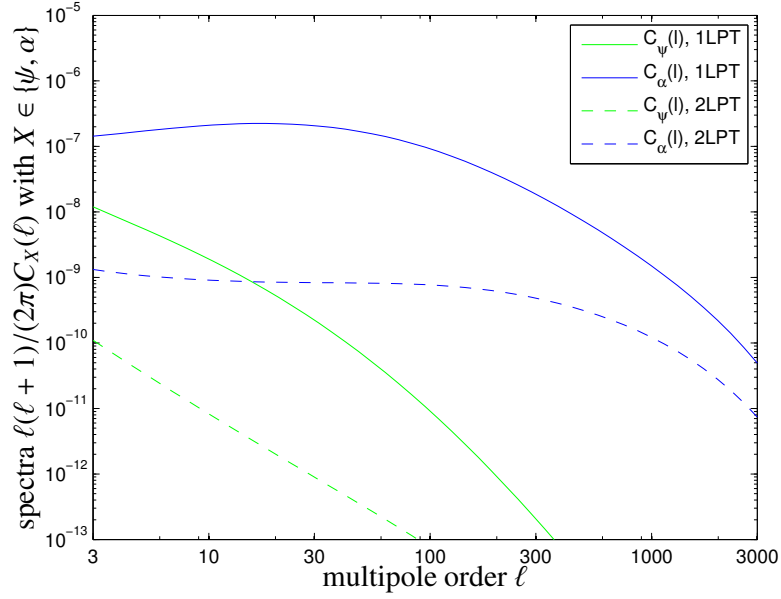
Figure 7.2.: Angular spectrum $C_\psi(\ell)$ (green line) of the displacement potential ψ and the spectrum $C_\alpha(\ell) \equiv l^2 C_\psi(\ell)$ (blue line) of the displacement field $\alpha = \nabla_\theta \psi$, for 1LPT (solid line) and 2LPT (dashed line).
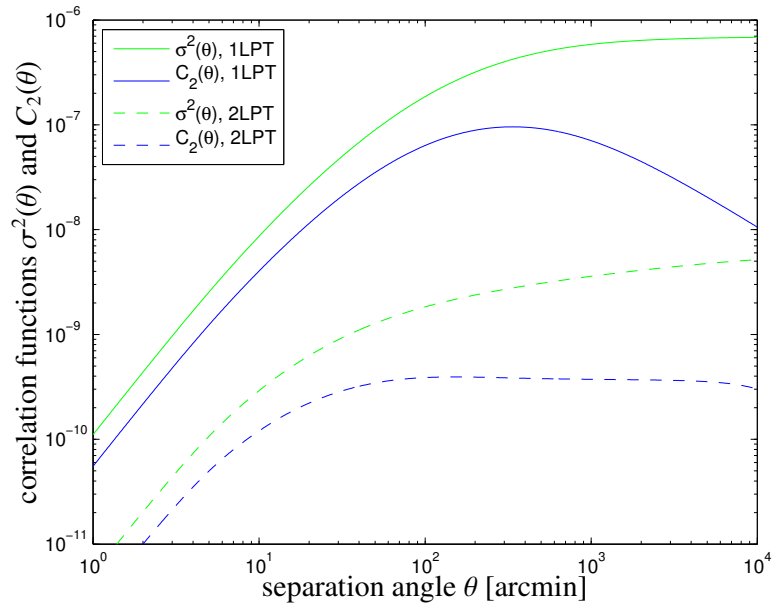

Figure 7.3.: Correlation functions $\sigma^2(\theta) = C_0(0) - C_0(\theta)$ (blue line) and $C_2(\theta)$ (green line) as a function of separation angle θ, for 1LPT (solid line) and 2LPT (dashed line).

becomes possible to derive spectra of the evolved ellipticity field. Peculiar motion by $D_+(a)\nabla\Phi$ changes the position of a galaxy by a shifting angle $\alpha = D_+\nabla\Phi/\chi$ if the galaxy is situated at a comoving distance χ. The angular displacement field α can be derived from a displacement potential $\Psi = D_+\Phi/\chi^2$ by angular derivation, such that $\alpha = \nabla_\theta\Psi$, because $\nabla_\theta = \chi\nabla$. Generalizing this argument to a galaxy population which is described by a normalized distribution $n(\chi)\mathrm{d}\chi$ in comoving distance χ one obtains an expression for the angular displacement potential,

$$\Psi(\theta) = \int_0^{\chi_H} \mathrm{d}\chi\, W_\Psi(\chi)\Phi(\theta_\chi,\chi) \quad \text{with} \quad W_\Psi(\chi) = \frac{n(\chi)D_+}{\chi^2}, \tag{7.30}$$

which replaces the lensing potential in the case of gravitational lensing of the CMB. The statistical properties of Ψ, which is a Gaussian random field, are described by the spectrum $C_\Psi(\ell)$,

$$C_\Psi(\ell) = \int \frac{\mathrm{d}\chi}{\chi^2} W_\Psi^2(\chi)P_\Phi(k = \ell/\chi), \tag{7.31}$$

which results from carrying out a Limber projection of Ψ. The spectrum $C_\alpha(\ell)$ is related to $C_\Psi(\ell)$ by $C_\alpha(\ell) = \ell^2 C_\Psi(\ell)$ as a consequence of the relation $\alpha = \nabla_\theta\Psi$. Statistical isotropy of the gradient field $\nabla\Phi$ and correct the variance of α by a factor of 2/3 because motion of galaxies along gradients parallel to the line of sight does not affect the angular position on the sky.

The angular spectrum $C_\Psi(\ell)$ of the displacement potential Ψ resulting from the Limber projection of $P_\Phi(k)$ is depicted in Fig. 7.2 along with the spectrum $C_\alpha(\ell) = \ell^2 C_\Psi(\ell)$ of the displacement angle α. Clearly, the 1LPT result dominates the 2LPT result by more than one order of magnitude, as already suggested by Fig. 7.2. The similarity of the plot to the analogous quantities in CMB lensing is striking (compare with fig. 4 of Lewis & Challinor (2006)).

As shown by Seljak (1996a), correlations between the components of the shifting angle α at two positions $\boldsymbol{\theta}_1$ and $\boldsymbol{\theta}_2$ are described by

$$\langle\alpha_i(\boldsymbol{\theta}_1)\alpha_j(\boldsymbol{\theta}_2)\rangle = \frac{1}{2}C_0(\theta) - C_2(\theta)\hat{\theta}_{\langle i}\hat{\theta}_{j\rangle} \tag{7.32}$$

with $\boldsymbol{\theta} = \boldsymbol{\theta}_2 - \boldsymbol{\theta}_1$, and correlation functions of the displacement angle which are defined as

$$C_0(\theta) = \int \frac{\ell^3\mathrm{d}\ell}{2\pi}C_\Psi(\ell)J_0(\ell\theta) \tag{7.33}$$

and

$$C_2(\theta) = \int \frac{\ell^3\mathrm{d}\ell}{2\pi}C_\Psi(\ell)J_2(\ell\theta). \tag{7.34}$$

In complete analogy to the lensing of the CMB the abbreviation $\sigma^2(\theta) - C_0(\theta)$ is introduced for describing uncorrelated displacements. The characteristic function of a Gaussian displacement field α would then be

$$\langle\exp(\iota\ell[\alpha(\boldsymbol{\theta}_1) - \alpha(\boldsymbol{\theta}_2)])\rangle = \exp\left(\frac{\ell^2}{2}\left[-\sigma^2(\theta) + \cos 2\phi_\ell C_2(\theta)\right]\right). \tag{7.35}$$

The characteristic function can be Taylor-expanded because $\ell C_2(\theta) \ll 1$,

$$\langle\exp(\iota\ell[\alpha(\boldsymbol{\theta}_1) - \alpha(\boldsymbol{\theta}_2)])\rangle \simeq \exp\left(-\frac{\ell^2\sigma^2(\theta)}{2}\right)\left(1 - \frac{\ell^2}{2}\cos 2\phi_\ell C_2(\theta)\right). \tag{7.36}$$

In the case of CMB lensing, non-Gaussian contributions have been shown to have negligible effect on the deflection angle statistic Carbone et al. (2009), Schäfer & Merkel (2012), and in the case of weak cosmic shear, analogous arguments about the sparsity of strong deflections apply equally Hamana et al. (2005).

Fig. 7.3 shows the quantities $\sigma^2(\theta) = C_0(0) - C_0(\theta)$ and $C_2(\theta)$ used in this formalism, for both 1LPT and 2LPT. The similarity between the obtained results and the formally equivalent result in CMB lensing is striking. Compared to the 2LPT corrections the 1LPT contributions to the spectrum are dominating.

The CMB-lensing formalism has been worked out for full and flat-sky applications (Seljak 1996b, Hu 2000, Challinor & Lewis 2005, Lewis & Challinor 2006). For this work the flat-sky approximation is sufficient as ellipticity correlations and their displacements due to peculiar motion are a small-scale phenomenon.

Following Seljak (1996b), the correlation properties of the shifted ellipticity field can be described using the two correlation functions $\xi_\pm(\theta)$,

$$\xi'_+(\theta) = \langle \epsilon^*(x + \alpha)\, \epsilon(x' + \alpha') \rangle \tag{7.37}$$

$$\xi'_-(\theta) = \langle \exp(-4\iota\phi_\ell)\epsilon^*(x + \alpha)\, \epsilon(x' + \alpha') \rangle, \tag{7.38}$$

where the points at which the ellipticities are observed are shifted by exactly the angle α. The complex field $\epsilon(\theta)$ can be synthesized from the Fourier modes $\epsilon(\ell)$ including the lensing shift $\theta \to \theta + \alpha$,

$$\epsilon(\theta) = \int \frac{d^2\ell}{(2\pi)^2}\, \epsilon(\ell) \exp(\iota\ell(x + \alpha)). \tag{7.39}$$

The correlation function $\xi'_+(\theta)$ of the shifted ellipticity field is then given in terms of the ellipticity spectra C_E^ϵ and $C_E^\epsilon(\ell)$,

$$\xi'_+ = \int \frac{d^2\ell}{(2\pi)^2}\, (C_E^\epsilon(\ell) + C_B^\epsilon(\ell)) \langle \exp(\iota\ell[\alpha(\theta_1) - \alpha(\theta_2)]) \rangle, \tag{7.40}$$

which can be written using equation 7.36 as

$$\xi'_+ = \int \frac{d^2\ell}{(2\pi)^2}\, (C_E^\epsilon(\ell) + C_B^\epsilon(\ell)) \exp\left(-\frac{\ell^2\sigma^2}{2}\right)\left[J_4(\ell\theta) + \frac{\ell^2}{2}J_s(\ell\theta)\right], \tag{7.41}$$

with the abbreviation $J_s(x) = J_2(x) + J_6(x)$. These two correlation functions can be converted to E-mode and B-mode spectra and expressed very concisely in a matrix notation:

$$\begin{pmatrix} C'_E(\ell) \\ C'_B(\ell) \end{pmatrix} = \int \ell' d\ell' \begin{pmatrix} W_+(\ell, \ell') & W_-(\ell, \ell') \\ W_-(\ell, \ell') & W_+(\ell, \ell') \end{pmatrix} \begin{pmatrix} C_E^\epsilon(\ell') \\ C_B^\epsilon(\ell') \end{pmatrix}. \tag{7.42}$$

This notation shows explicitly the mixing between scales due to the convolution integral and the conversion between $C_E^\epsilon(\ell)$ and $C_B^\epsilon(\ell)$ under the influence of $W_-(\ell, \ell')$, which is the non0diagonal entry of the mixing matrix. The kernels $W_\pm(\ell, \ell')$ are given by

$$W_+(\ell, \ell') = \frac{1}{2}\int \theta d\theta \left[J_0(\ell\theta)A(\ell', \theta) + J_4(\ell\theta)B(\ell', \theta)\right], \tag{7.43}$$

$$W_-(\ell, \ell') = \frac{1}{2}\int \theta d\theta \left[J_0(\ell\theta)A(\ell', \theta) - J_4(\ell\theta)B(\ell', \theta)\right], \tag{7.44}$$

with the functions

$$A(\ell, \theta) = \exp\left(-\frac{\ell^2 \sigma^2(\theta)}{2}\right)\left[J_0(\ell, \theta) + \frac{\ell^2}{2}C_2(\theta)J_4(\ell\theta)\right], \tag{7.45}$$

$$B(\ell, \theta) = \exp\left(-\frac{\ell^2 \sigma^2(\theta)}{2}\right)\left[J_4(\ell, \theta) + \frac{\ell^2}{2}C_2(\theta)J_s(\ell\theta)\right], \tag{7.46}$$

which describe uncorrelated shifting due to $\sigma^2(\theta)$ and correlated displacements due to $C_2(\theta)$. In the limit of no shifting, $C_0(\theta) = C_2(\theta) = 0$ such that $W_+(\ell, \ell') = \delta(\ell - \ell')/\ell$ and $W_-(\ell, \ell') = 0$, due to the orthogonality relations of the cylindrical Bessel functions,

$$\int \theta \mathrm{d}\theta\, J_n(\ell\theta)J_n(\ell'\theta) = \ell^{-1}\delta(\ell - \ell). \tag{7.47}$$

In this case, the convolution is reduced to a Dirac δ_D-function and the mixing matrix is the unit matrix, so that the E-mode and B-mode amplitudes are conserved. In this work, I verified that higher order corrections arising in the transformation of correlation functions do have a negligible effect for the evolved ellipticity correlations Challinor & Lewis (2005), Lewis & Challinor (2006).

The applicability of the formalism is limited to the validity of LPT for describing the motion of galaxies. At low redshifts, the large-scale structure is evolving in a nonlinear way, galaxy trajectories can intersect and merging can take place such that extrapolation galaxy positions from their initial positions with a velocity potential are no longer valid.

7.4.1. E/B-mode conversion

Figs. 7.4 and 7.5 show the mode coupling kernels $W_+(\ell, \ell')$ and $W_-(\ell, \ell')$ where for simplicity the focus is on 1LPT because the contributions due to 2LPT are comparatively small. From Fig. 7.4 it can be seen that the power of the W_+ kernel is mainly distributed along the diagonal and increasing with multipole number, with maximum contribution from $\ell \approx 300$ to 3000. The off-diagonal contribution creates a convolution (equation 35) between the spectra at different multipoles, mediated by $W_+(\ell, \ell')$. In contrast, the mode coupling kernel W_- (Fig. 7.5), which is responsible for the E/B conversion, shows a lateral pattern which is three orders of magnitude smaller in amplitude and decreasing with higher multipole numbers (ℓ, ℓ'). Fig. 6 shows cuts through the absolute value of the otherwise rapidly oscillating functions $W_\pm(\ell, \ell')$. The diagonality of $W_+(\ell, \ell')$ is clearly visible. The structure of $W_-(\ell, \ell')$ at high multipoles is caused by the exponential cut-off of the displacement spectrum due to the imposed mass filtering and I verified the absence of such a feature for spectra with asymptotical power-law behaviour.

7.5. Effect of peculiar velocities on intrinsic ellipticity correlations

7.5.1. Ellipticity spectra

Fig. 7.6 shows the intrinsic ellipticity spectra $C_E^\epsilon(\ell)$ and $C_B^\epsilon(\ell)$ for the Euclid galaxy sample with its median redshift at $z_{\mathrm{med}} = 0.9$. The spectra are constant and equal in amplitude up to multi-
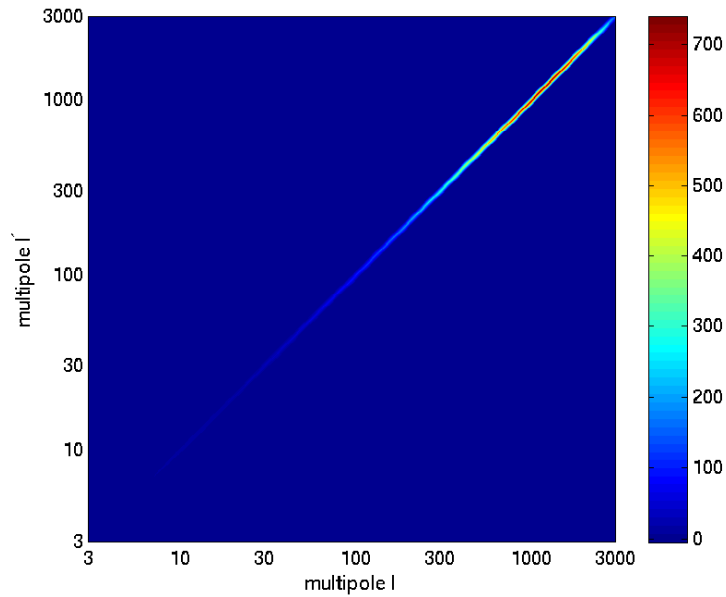
Figure 7.4.: Mode coupling kernel $(\ell\ell') \times W_+(\ell, \ell')$ used in the transformation of the ellipticity spectra. For simplicity, I focus on 1LPT because the contributions due to 2LPT are small.
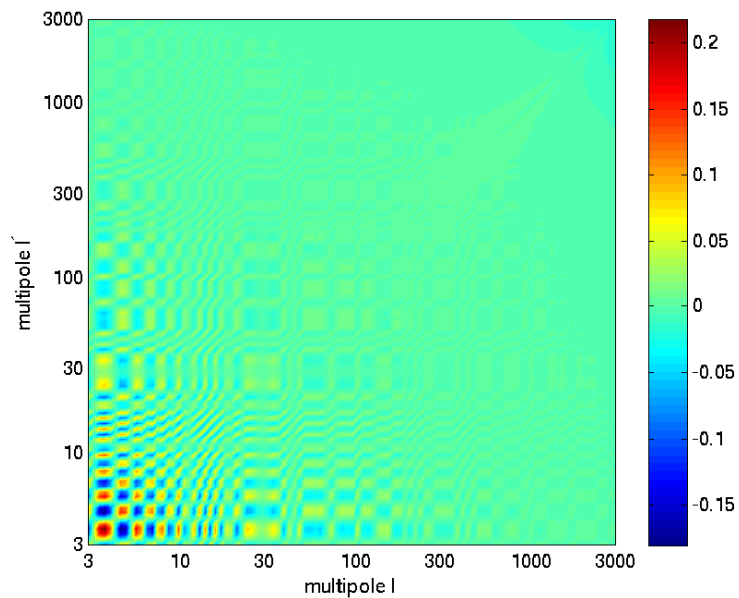

Figure 7.5.: Mode coupling kernel $(\ell\ell') \times W_-(\ell, \ell')$ responsible for the $E \leftrightarrows B$-mode conversion in the ellipticity field. Again, the results for 1LPT are shown because the contributions from 2LPT are small.

poles of $\ell \simeq 100$, indicating the absence of correlations such that on each scale one measures the variance of the uncorrelated ellipticity field. Correlations become important on angular scales $\ell \geq 300$ where the spectra level off and decrease from multipoles of $\ell \geq 3000$ on very rapidly. In the peak region, the ellipticity E-modes have an amplitude larger than the B-modes by about an order of magnitude. The effect of peculiar motion is illustrated by the same figure and for comparison with weak lensing, the weak convergence spectrum $C_\kappa(\ell)$ is plotted according to the Euclid galaxy sample resulting from a nonlinear CDM spectrum (using the parametrization by Smith et al. (2003). The first observation is that ellipticity correlations reach amplitudes similar to those of the weak lensing convergence in the nonlinear part corresponding to amplitudes $\ell \leq 300$, and that the intrinsic E-mode spectrum $C_E^\epsilon(\ell)$ is larger than the B-mode spectrum $C_B^\epsilon(\ell)$ by about an order of magnitude in this regime. On larger angular scales, there are no appreciable ellipticity correlations and one effectively observes the variance of the ellipticity field for uncorrelated objects. Consequently, the spectra have identical amplitudes and are effectively constant. In this regime, the shifting effect is not able to affect the galaxies, which is a well-known result in CMB lensing, where scale-free spectra are invariant (Lewis & Challinor 2006): the mode-conversion mechanism is uneffective if the spectra are equal, $C_E^\epsilon(\ell) = C_B^\epsilon(\ell)$, and the convolution with $W_+(\ell, \ell')$ is not able to redistribute amplitudes. In contrast, both spectra are affected on multipoles $\ell > 1000$, where in particular $C_B'(\ell)$ has decreased relative to $C_B^\epsilon(\ell)$. The loss in amplitude of the ellipticity spectra $C_E^\epsilon(\ell)$ and $C_B^\epsilon(\ell)$ can be explained in a very pictorial way: the functions $W_\pm(\ell, \ell')$ used for transforming the ellipticity spectra are proportional to a Gaussian $\exp(-\ell^2 \sigma^2(\theta))$ which smoothes the spectra and cuts off on a scale $\ell\theta \lesssim 1$. Physically, the galaxies are reordered in an uncorrelated way by peculiar motion which leads to a randomization of the ellipticity field and therefore to a decreased ellipticity spectrum. Fig. 7.7 compares the relative magnitude of all spectra as a function of multipole ℓ. The plot shows the relative ratio of the evolved and initial E-mode and B-mode spectra. As already indicated by Fig. 7.6, a significant decrease for $\ell > 1000$ of up to 10 per cent for the E- and 60 per cent for the B-modes at $\ell \simeq 3000$ can be seen. The ratios $C_B'(\ell)/C_E'(\ell)$ and $C_B^\epsilon(\ell)/C_E^\epsilon(\ell)$ of intrinsic and evolved spectra are similar up to multipoles of $\ell \simeq 1000$, where they separate and indicate that the newly generated B-modes are small and that the B-mode spectra are more strongly affected. For Euclid's weak lensing application, changes in the ellipticity spectra are affecting scales where the shape noise starts dominating, but for shallower surveys, lower multipoles would be affected by the peculiar motion effect. Finally, Fig. 7.8 gives an impression of the mode conversion mechanism, where the evolved spectra $C_E'(\ell)$ and $C_B'(\ell)$ are plotted with the E-mode or the B-mode in the initial spectra deliberately set to zero, i.e. $C_E^\epsilon(\ell) = 0$ in the first and $C_B^\epsilon(\ell) = 0$ in the second case. Even in the absence of a particular initial mode no power is observed in the corresponding evolved spectrum, as a consequence of E/B-coupling introduced by peculiar motion.

7.6. Summary

Topic of this paper is the evolution of intrinsic ellipticity correlation between galaxies due to peculiar motion. Intrinsic ellipticity correlations are derived in the framework of angular momentum models, which explain these correlations by correlated tidal shears experienced by the protohaloes in acquiring their angular momenta. Because the symmetry axis of the galactic disk is related to the angular momentum direction of the host halo, correlated angular momenta give
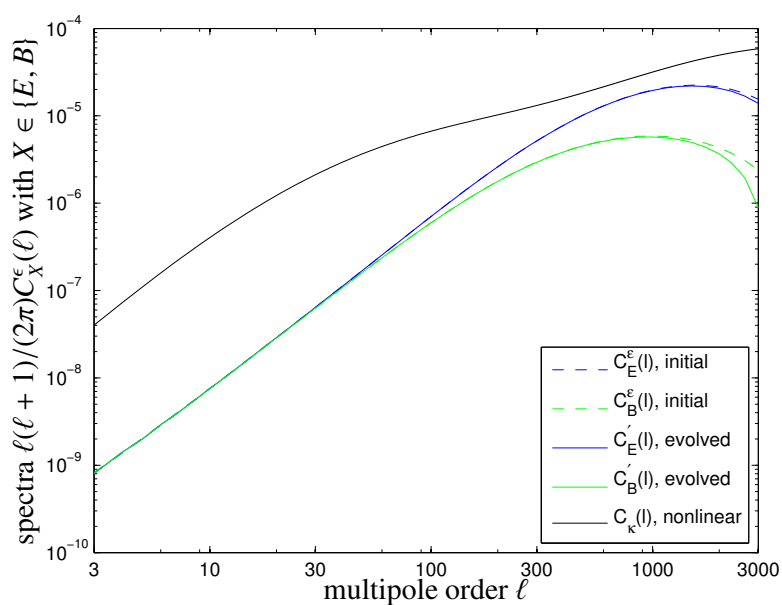
Figure 7.6.: Ellipticity spectra $C_E^\epsilon(\ell)$ (blue line) and $C_B^\epsilon(\ell)$ (green line) as predicted by the angular momentum model with $a = 0.25$ and the disk thickness parameter set to $\alpha = 1$ (dashed line), and the evolved ellipticity spectra (solid line) where the displacements were computed by 1LPT. For comparison, the spectrum $C_\kappa(\ell)$ of the weak lensing convergence is plotted for a linear (black dashed line) and nonlinear (black solid line) CDM spectrum.
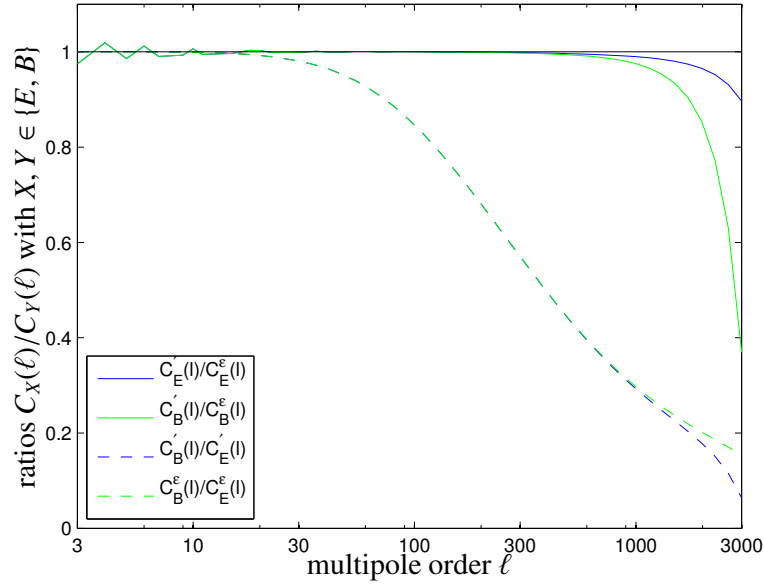
Figure 7.7.: Ratios $C'_E(\ell)/C^\epsilon_E(\ell)$ (blue solid line), $C'_B(\ell)/C^\epsilon_B(\ell)$ (green solid line), $C'_B(\ell)/C'_E(\ell)$ (blue dashed line) and $C^\epsilon_B(\ell)/C^\epsilon_E(\ell)$ (green dashed line) with all displacements following from 1LPT.
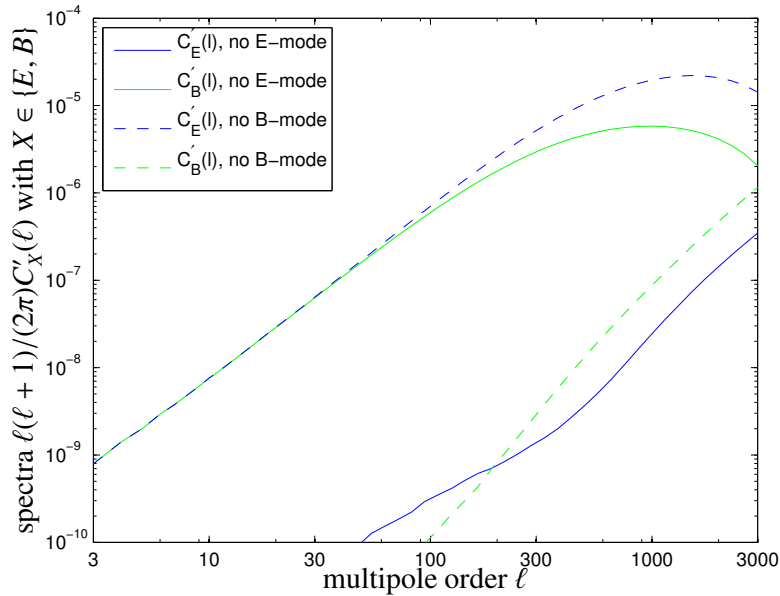

Figure 7.8.: Contributions to the evolved ellipticity spectra $C'_E(\ell)$ (blue lines) and $C'_B(\ell)$ (green lines): no initial B-mode spectrum, $C^\epsilon_B(\ell) = 0$ (dashed lines) and no initial E-mode spectrum, $C^\epsilon_E(\ell) = 0$ (solid lines).

rise to correlated angles of inclination and hence correlated ellipticities.

(i) Peculiar motion of galaxies changes the correlation properties of the ellipticity field by displacing the galaxies and distorting the ellipticity field. The peculiar motion by LPT is described and the corresponding displacement angles along with their statistical properties for the Euclid galaxy sample are derived. The formalism for evolving the ellipticity spectra uses an analogy to the formalism describing lensing of the CMB polarization spectra. Both quantities, the ellipticity field as well as the polarization field, have the same symmetry properties, being of spin 2. The loci at which ellipticities and polarizations are measured are displaced by peculiar motion in the first and by gravitational lensing in the second case. Because the peculiar motion field in the quasi-linear regime is a flow resulting from a velocity potential in the same way as the lensing displacements follow as gradients from the lensing potential, it is possible to derive all necessary quantities in complete analogy.

(ii) Peculiar motion has two effects on the ellipticity spectra: There is a convolution of the spectra and a conversion between E-modes and B-modes of the ellipticity field. Both effects become important on angular scales $\ell > 1000$, because on smaller multipoles, the spectra are effectively constant and equally large. In particular, the spectrum $C_B^\epsilon(\ell)$ is strongly affected and loses amplitude: for the Euclid galaxy sample decrements by about 10 per cent for $C_E^\epsilon(\ell)$ and 60 per cent for $C_B^\epsilon(\ell)$ are observed. The mode-conversion mechanism is comparatively weak and it was tested by deliberately setting the initial spectra $C_E^\epsilon(\ell)$ and $C_B^\epsilon(\ell)$ to zero.

(iii) Second-order corrections in the dynamical model were found to be negligibly small in comparison to first-order LPT. Likewise, it was verified that higher order corrections in the transformation of the ellipticity spectra had a minor effect on the evolved ellipticity spectra.

(iv) The formalism for time-evolving ellipticity spectra can be used for predicting intrinsic ellipticity contaminations in tomographic weak lensing surveys: one would need to derive $W_\pm(\ell, \ell')$-functions for every redshift slice and transform the ellipticity spectra $C_{E,B}^\epsilon(\ell)$ accordingly. Interesting phenomena occur at low redshift, where the magnitude of intrinsic alignments exceeds that of weak lensing, but it was checked that even at low redshifts of $z = 0.3$, changes in the ellipticity spectrum occur only on multipoles $\gtrsim 300$, which is likely to be noise dominated even in future surveys.

It can be concluded that in principle the dispersing effect of peculiar motion weakens intrinsic ellipticity correlations and make them less troublesome for analysing weak lensing data. For the case of Euclid changes in the spectra can be seen on scales where the shape noise is already dominating. A natural extension to this investigation would comprise the shifting and distorting effect of weak gravitational lensing, and ultimately the usage of analysis methods conceived for the polarization of the CMB for investigating intrinsic ellipticity correlations.

Note

The results of this chapter are the basis of Giahi & Schäfer (2012) and have been accepted for publication.

8. Non-Gaussianity model comparison

8.1. Introduction

Model specific (Parkinson et al. 2006, Mukherjee et al. 2006) and general methodological papers (Trotta 2008) have been published on Bayesian model selection, indicating a growing interest in this kind of statistics which fundamentally differs from the established frequentist philosophy. In this work, different models are compared for the configuration dependence of inflationary non-Gaussianities, which due to their fundamental importance in cosmology and the recent progress in observations (Bartolo et al. 2004, Komatsu 2010) are of great interest both for theorists and observers. An interesting application is the family of non-Gaussian inflationary models with linear dependence on the non-linearity parameter f_{NL} which represent the different bispectral configurations local, equilateral, and orthogonal. While of great interest from a physical point of view, these models offer a transparent and intuitive way to study the principles of Bayesian model selection at comparatively low computational cost. Therefore, the focus of this article is on both the comparison of non-Gaussianity models and an instructive Bayesian analysis of this class of models. In this study the applicability of weak lensing bispectra in view of comparing different inflationary models is investigated. Bispectra for each type of model are calculated and analyzed with the Fisher formalism to compute the corresponding weak lensing standard deviations on f_{NL}, σ_{local}, σ_{ortho}, and σ_{equil} (Schäfer et al. 2012), which are then employed in the Bayesian model selection formalism. In this work, it will be shown that weak lensing tomography, enhance the precision of the weak lensing bispectra significantly, allowing for the applicability of Bayesian inference. For structure formation non-Gaussianities, it was shown by Takada & Jain (2004), that weak lensing tomography with 3 redshift bins yields an increase in information content by a factor of $\approx 3-4$. In order to provide an estimate of the full potential of weak lensing tomography, this work considers 2 redshift bins in order to derive significant constraints for the three inflationary non-Gaussianity models considered in this thesis. By focussing on weak lensing bispectra this work complements CMB studies on inflationary non-Gaussianities using the angular bispectrum of CMB temperature anisotropy obtained the Wilkinson Microwave Anisitropy Probe (WMAP) (Komatsu 2010, Komatsu et al. 2011). Bayesian model analysis is very different in nature from the Frequentist philosophy. These differences may cause surprising results if both methods are being compared with prominent examples, such as Lindley's paradox. Since the Frequentist p-value statistics is widely used in cosmology, inflationary models are compared both from a frequentist and Bayesian perspective. The intention of this study is to give an estimate of the applicability of weak lensing methods for non-Gaussian inflationary model selection. It is also comparing the methodology of model selection with regard to Bayesian and Frequentist statistics. The following calculations include cosmic variance and shape noise but neglect systematical errors. Other sources of non-Gaussianities, such as those arising from structure formation are not considered here, since they can be separated from the primordial

non-Gaussities arising from inflation with high precision if a strong prior on the cosmological parameter set is available, as shown by Schäfer et al. (2012). Furthermore, the Bayesian analysis given in this work is prior-dominated due to the lack of highly conclusive weak lensing data. This is plausible considering the Gaussianizing effect predicted by the central limit theorem due to the line of sight integration (Limber projection). This is an important difference to observations of the CMB bispectrum, which makes non-tomographic weak lensing data less sensitive to non-Gaussianities. On the other hand, weak lensing is more sensitive to smaller scales than the CMB and hence provide an additional constraint on inflationary non-Gaussianity models.

Section 8.2 gives an overview of the cosmology used in this study. Statistics of non-Gaussianities by means of weak lensing bispectra are discussed in Section 8.3 with a description of the inflationary non-Gaussinianity models considered in this work. Weak lensing principles are introduced in Section 8.4. The Fisher formalism and χ^2 optimization for the estimators employed in this study are describedin Section 8.5. The technique of weak lensing tomography and results from calculations for up to 5 redshift bins are contained in Section 8.6. Frequentist and Bayesian inference are introduced in Section 8.7 and 8.8, respectively. Bayesian and Frequentist results are complemented in Section 8.9. A summary and outlook is given in Section 8.10.

As reference model a spatially flat wCDM model with Gaussian adiabatic initial perturbations in the cold dark matter density is chosen. Specifically, parameters are $\Omega_m = 0.25$, $n_s = 1$, $\sigma_8 = 0.8$, $\Omega_b = 0.04$ and finally $H_0 = 10^5\, h$ m/s/Mpc, with $h = 0.72$. The dark energy equation of state is set to $w = -0.9$.

8.2. Cosmology

8.2.1. Dark energy cosmologies

The time evolution of isotropic Friedmann-universe with homogeneous dark matter and dark energy is described by the Hubble function $H(a) = \mathrm{d}\ln a/\mathrm{d}t$, which is given by

$$\frac{H^2(a)}{H_0^2} = \frac{\Omega_m}{a^3} + (1 - \Omega_m)\exp\left(3\int_a^1 \mathrm{d}\ln a\,(1 + w(a))\right),\tag{8.1}$$

with the matter density parameter Ω_m and the dark energy equation of state function $w(a)$. Spatial flatness requires the dark energy density to be $1 - \Omega_m$. The comoving distance χ can be computed from the scale factor a,

$$\chi = c\int_a^1 \frac{\mathrm{d}a}{a^2 H(a)}.\tag{8.2}$$

For the galaxy redshift distribution $n(z)\mathrm{d}z$, a standard shape,

$$n(z) = n_0\left(\frac{z}{z_0}\right)^2 \exp\left(-\left(\frac{z}{z_0}\right)^\beta\right)\mathrm{d}z \quad \text{with} \quad \frac{1}{n_0} = \frac{z_0}{\beta}\Gamma\left(\frac{3}{\beta}\right),\tag{8.3}$$

is used, with $\beta = 3/2$. z_0 is chosen such that the distribution has a median redshift of 0.9 corresponding to EUCLID which will be contrasted with a galaxy distribution of identical shape but with a much lower median of 0.3. This work refers to the two application cases as the high and low redshift galaxy sample, respectively. The distribution can be rewritten in terms of comoving distance using the relation $p(z)\mathrm{d}z = p(\chi)\mathrm{d}\chi$ with $\mathrm{d}z/\mathrm{d}\chi = H(\chi)/c$.

8.2.2. CDM power spectrum

The CDM power spectrum P_δ describes the wavelength dependence of the density correlations. For the statistically homogeneous Gaussian density field δ the power spectrum is defined in Fourier space as

$$\langle \delta(\boldsymbol{k})\delta(\boldsymbol{k}')\rangle = (2\pi)^3 \delta_D(\boldsymbol{k} + \boldsymbol{k}')P_\delta(k), \tag{8.4}$$

in a sufficiently flat space. For the shape of the power spectrum the following Ansatz is used (Bardeen et al. 1986):

$$P_\delta(k) \propto k^{n_s} T^2(k), \tag{8.5}$$

with $T(k)$ being a transfer function approximated by

$$T(q) = \frac{\ln(1 + 2.34q)}{2.34q}\left(1 + 3.89q + (16.1q)^2 + (5.46q)^3 + (6.71q)^4\right)^{-\frac{1}{4}}, \tag{8.6}$$

and $k = q\Gamma$ measured in units of the shape parameter (Sugiyama 1995)

$$\Gamma = \Omega_m h \exp\left[-\Omega_b\left(1 + \frac{\sqrt{2h}}{\Omega_m}\right)\right]. \tag{8.7}$$

The amplitude of P_δ is normalized on the scale $R = 8$ Mpc/h to the variance σ_8,

$$\sigma_R^2 = \int \frac{k^2 \mathrm{d}k}{2\pi^2} P_\delta(k) W^2(kR), \tag{8.8}$$

with a Fourier transformed spherical top hat filter function $W(x) = 3j_1(x)/x$, and j_1 denoting the spherical Bessel function of the first kind of order ℓ (Abramowitz M. 1972).

8.3. Statistics of non-Gaussianities

Any Gaussian distribution is described by its first two moments and is thus determined by two-point correlation functions. Non-Gaussian statistics, however, require higher order spectral estimates in order to be characterized. The bispectrum is an important observable since it is the lowest order statistics sensitive to non-Gaussian signatures in a given statistical distribution. The bispectrum is the equivalent of the three-point correlation function in Fourier space (see Chapter 5).

8.3.1. Primordial bispectrum

The primordial bispectra is written here in terms of the Bardeen curvature perturbation Φ (Bardeen 1980, Bardeen et al. 1983). The bispectrum of Φ is given by

$$\langle \Phi(\boldsymbol{k}_1)\Phi(\boldsymbol{k}_2)\Phi(\boldsymbol{k}_3)\rangle = (2\pi)^3 \delta_D(\boldsymbol{k}_1 + \boldsymbol{k}_2 + \boldsymbol{k}_3)B_\Phi(k_1, k_2, k_3). \tag{8.9}$$

The potential fluctuations are transformed to those of the density field by the Newtonian Poisson equation

$$\Delta\Phi = \frac{3}{2}\frac{\Omega_m}{\chi_H^2}\delta, \tag{8.10}$$

or in Fourier space

$$\delta(k, a) = \frac{2}{3\Omega_m} D_+(\chi_H k)^2 T(k)\Phi(k). \tag{8.11}$$

Each mode has a horizon passing which is governed by $T(k)$ and grows by D_+ in the linear regime, giving a bispectrum,

$$B_\delta(k_1, k_2, k_3, a) = \prod_{i=1}^{3} \left(\frac{2}{3\Omega_m} D_+(\chi_H k_i)^2 T(k_i)\right) B_\Phi(k_1, k_2, k_3), \tag{8.12}$$

which is proportional to D_+^3 (Munshi et al. 2011). The normalisation factor A is chosen to be consistent with σ_8 for each linearly evolving mode.

8.3.2. Inflationary non-Gaussianity models

In this work three different bispectral shapes are considered which cover a wide range of inflationary models (Komatsu 2010):

(i) The **local form** is defined by

$$B_\Phi^{\text{local}}(k_1, k_2, k_3) = 2A^2 f_{\text{NL}}^{\text{local}}\left(k_1^{n_S-4} k_2^{n_S-4} + (2\,\text{perm})\right), \tag{8.13}$$

where A is the normalization factor for the CDM power spectrum and $P_\Phi = A k^{n_S-4}$. This form is called the local form since it can be obtained through a Taylor expansion $\Phi = \Phi_L + f_{\text{NL}}^{\text{local}}\Phi_L^2$, where both sides are evaluated at the same location in space, with Φ_L being a linear Gaussian fluctuation). The local form peaks for $k_3 \ll k_2 \approx k_1$.

(ii) The **equilateral form**

$$
\begin{aligned}
B_\Phi^{\text{equil}}(k_1, k_2, k_3) &= 6A^2 f_{\text{NL}}^{\text{equil}}\Big(-2(k_1 k_2 k_3)^{2(n_S-4)/3} \\
&\quad - \left[(k_1 k_2)^{n_S-4} + (2\,\text{perm})\right] \\
&\quad + \left[k_1^{(n_S-4)/3} + k_2^{2(n_S-4)/3} + k_3^{n_S-4} + (5\,\text{perm})\right]\Big)
\end{aligned} \tag{8.14}
$$

arises in models with non-canonical kinetic terms, such as the Dirac-Born-Infeld inflation (Silverstein & Tong 2004, Alishahiha et al. 2004). There are, though, other models from which this form can be produced (Arkani-Hamed et al. 2004, Seery & Lidsey 2005, Chen et al. 2007, Cheung et al. 2008, Li et al. 2008).

(iii) The **orthogonal form**

$$
\begin{aligned}
B_\Phi^{\text{ortho}}(k_1, k_2, k_3) &= 6A^2 f_{\text{NL}}^{\text{ortho}}\Big(-8(k_1 k_2 k_3)^{2(n_S-4)/3} \\
&\quad - \left[(k_1 k_2)^{n_S-4} + (2\,\text{perm})\right] \\
&\quad + 3\left[k_1^{(n_S-4)/3} + k_2^{2(n_S-4)/3} + k_3^{n_S-4} + (5\,\text{perm})\right]\Big)
\end{aligned} \tag{8.15}
$$

is both orthogonal to the equilateral and local shape (Senatore et al. 2010). This form arise from a linear combination of higher-derivative scalar-field interaction terms. It receives contributions from a broad range of triangles and has a positive peak for equilateral configurations.

Even though these forms cover many classes of non-Gaussianity models, not all shapes can be represented as a a superposition of the three shapes. Such kind of classes include the localised and oscillating bispectra, which may be caused by a feature in the inflaton potential (Chen et al. 2007, Arroja et al. 2011), particle production while observable modes are crossing the horizon, or an inflaton potential with superimposed oscillations (Chen et al. 2008, Chen 2012).

8.4. Weak lensing convergence spectra

8.4.1. Convergence power spectrum

The line-of-sight integration for the weak lensing convergence κ is weighted with the lensing efficiency $W_\kappa(\chi)$ (for a review, see Bartelmann & Schneider 2001, Bartelmann 2010), such that

$$\kappa = \int_0^{\chi_H} \mathrm{d}\chi \, W_\kappa(\chi)\delta. \tag{8.16}$$

Since this is a linear superposition, all statistical properties of the density field δ are preserved. The weight function is given by

$$W_\kappa(\chi) = \frac{3\Omega_m}{2a} \frac{1}{\chi_H^2} G(\chi)\chi, \tag{8.17}$$

with the lensing efficiency and matter density weighted distribution,

$$G(\chi) = \int_\chi^{\chi_H} \mathrm{d}\chi' n(z) \frac{\mathrm{d}z}{\mathrm{d}\chi'} \frac{\chi' - \chi}{\chi'}, \tag{8.18}$$

and redshift-dependent galaxy distribution $n(z)$. The projection for the spectrum $C_\kappa(\ell)$ is then given by Limber's equation (Limber 1954) which projects a homogeneous isotropic random field in three dimensions onto two dimensions,

$$C_\kappa(\ell) = \int_0^{\chi_H} \frac{\mathrm{d}\chi}{\chi^2} W_\kappa^2(\chi) P_\delta(k = \ell/\chi, a), \tag{8.19}$$

where for linear structure formation $C_\kappa(\ell) \propto D_+^2$.

8.4.2. Convergence bispectrum

The Limber projection for the convergence bispectrum in the flat-sky approximation is given by (Schneider et al. 1998, Hu 2000, Takada & Jain 2003a,b, 2004, Dodelson & Zhang 2005)

$$B_\kappa(\boldsymbol{\ell}_1, \boldsymbol{\ell}_2, \boldsymbol{\ell}_3) = \int_0^{\chi_H} \frac{\mathrm{d}\chi}{\chi^4} W_\kappa^3(\chi) B_\delta(\boldsymbol{k}_1/\chi, \boldsymbol{k}_2/\chi, \boldsymbol{k}_3/\chi, a). \tag{8.20}$$

The full-sky (spherical) bispectrum $B_{\ell_1\ell_2\ell_3}$ is related to the flat-sky bispectrum $B_\kappa(\boldsymbol{\ell}_1, \boldsymbol{\ell}_2, \boldsymbol{\ell}_3)$ by (Miralda-Escude 1991, Kaiser 1992)

$$B_{\ell_1\ell_2\ell_3} \simeq \begin{pmatrix} \ell_1 & \ell_2 & \ell_3 \\ 0 & 0 & 0 \end{pmatrix} \sqrt{\frac{\prod_{p=1}^3 (2\ell_p + 1)}{4\pi}} B_\kappa(\boldsymbol{\ell}_1, \boldsymbol{\ell}_2, \boldsymbol{\ell}_3) \tag{8.21}$$

71

with the Wigner 3-j symbol

$$\begin{pmatrix} \ell_1 & \ell_2 & \ell_3 \\ 0 & 0 & 0 \end{pmatrix}^2 = \frac{1}{2} \int_{-1}^{+1} dx \, P_{\ell_1}(x) P_{\ell_2}(x) P_{\ell_3}(x), \tag{8.22}$$

and Legendre polynomials $P_\ell(x)$ ($x = \cos\theta$). The factorials in the Wigner 3-j symbol are evaluated using the Stirling approximation for the Γ-function, $\Gamma(n+1) = n!$ ($n \in \mathbb{N}_+$), with

$$\Gamma(n) \approx \sqrt{2\pi} \exp(-n) n^{n-1/2}, \tag{8.23}$$

for $n \gg 1$ (Abramowitz M. (1972)). The Wigner 3-j symbol ensures the triangle condition $|\ell_i - \ell_j| \le \ell_k \le |\ell_i + \ell_j|$ and vanishes if $\sum_p \ell_p$ is an odd number.

As a consequence of the central limit theorem the line-of-sight integration of the uncorrelated lensing contributions results in a strong suppression of non-Gaussianities when the projection reaches over several correlation lengths of the density field (Jeong et al. 2011). Since the length scale of the Limber projection for the weak lensing bispectra considered in this paper is large compared to the correlation length of the density field, the resulting projection is a superposition of independent random processes for which the central limit theorem applies and thus the non-Gaussianities in the convergence field will be weaker then those in δ.

8.5. Fisher formalism and χ^2 optimization

The likelihood is quantified by the χ^2-value of a fit to the data with a certain fixed model, here a primordial non-Gaussianity model with bispectra $B_{\ell_1\ell_2\ell_3}^M$ and parameter f_{NL}^M, to a fiducial model, with B^T and f_{NL}^T, where the superscript T denotes the underlying true model from which the observed data are simulated:

$$\chi^2 = \sum_{\ell_{\min} \le \ell_1 \le \ell_2 \le \ell_3 \le \ell_{\max}} \frac{\left(B_{\ell_1\ell_2\ell_3}^M - B_{\ell_1\ell_2\ell_3}^T\right)^2}{\text{cov}(\ell_1, \ell_2, \ell_3)}, \tag{8.24}$$

with covariance

$$\text{cov}(\ell_1, \ell_2, \ell_3) = \frac{\Delta(\ell_1, \ell_2, \ell_3)}{f_{\text{sky}}} \tilde{C}_\kappa(\ell_1) \tilde{C}_\kappa(\ell_2) \tilde{C}_\kappa(\ell_3), \tag{8.25}$$

where the function $\Delta(\ell_1, \ell_2, \ell_3)$ counts the multiplicity of triangle configurations, allowing for carrying out the summation with the condition $\ell_1 \le \ell_2 \le \ell_3$ (Takada & Jain 2004). The fraction of the observed sky, f_{sky}, is set to 1/2, corresponding to Euclid. The intrinsic ellipticity of the galaxies adds white noise to the cosmic signal, thus it follows for the observed spectra

$$\tilde{C}_\kappa(\ell) = C_\kappa(\ell) + \frac{\sigma_\epsilon^2}{n}, \tag{8.26}$$

with the number density n of ellipticity measurements per steradian, which is set to 40 galaxies per squared arcminute, corresponding to the projected Euclid performance. Since non-Gaussian contributions to the covariance are strongly supressed by the central limit theorem the covariance only depends on the spectra $\tilde{C}_\kappa$, and is thus independent of the respective non-Gaussianity

model (Kaiser 1992, Takada & Jain 2004, Jeong et al. 2011). For the following calculations multipole numbers are considered in the range of $\ell_{\min} = 10$ to $\ell_{\max} = 3000$. It is worth to mention that on small scales baryonic physics and intrinsic alignments can lead to a contamination of the bispectral data of about 15 per cent, which stems from the correlation between a galaxies ellipticity and its surrounding density field. The systematic error estimates were obtained by numerical simulations for three-point intrinsic ellipticity correlations (III) and the three-point coupling between the weak lensing shear experienced by distant galaxies and the shape of foreground galaxies (GGI and GII) (Semboloni et al. 2008). To correct for this effect accurate photometric redshifts are necessary. A three-dimensional Monte-Carlo integration was used for the evaluation of equation (8.25) as provided by the publicly available CUBA-library (Hahn 2005).

With the likehood,

$$\mathcal{L} \propto \exp\left(-\frac{\chi^2}{2}\right),\tag{8.27}$$

which, due to the central limit theorem, derives from Gaussian-distributed fluctuations of each multipole of the measured bispectra around the true value and thus provides an unbiased estimate for f_{NL} (Section 5). Since the primordial non-Gaussian bispectrum depends linearly on f_{NL}, the likelihood is Gaussian-distributed with respect to the non-Gaussianity parameter f_{NL}. Due to the single parameter dependence on f_{NL}, the Fisher matrix (Section 5) consists of one element given by

$$F = \sum_{\ell_{\min} \leq \ell_1 \leq \ell_2 \leq \ell_3 \leq \ell_{\max}} \frac{\partial B_{\ell_1\ell_2\ell_3}}{\partial f_{\mathrm{NL}}} \frac{1}{\mathrm{cov}(\ell_1,\ell_2,\ell_3)} \frac{\partial B_{\ell_1\ell_2\ell_3}}{\partial f_{\mathrm{NL}}} = \frac{1}{f_{\mathrm{NL}}^2} \Sigma^2,\tag{8.28}$$

where Σ denotes the signal to noise ratio. The Cramer-Rao bounds, revealing the smallest possible errors in case of a Gaussian likelihood, are given by

$$\sigma = \sqrt{F^{-1}},\tag{8.29}$$

yielding $\sigma_{\mathrm{local}} = 75$ for the local, $\sigma_{\mathrm{ortho}} = 352$ for the orthogonal, and $\sigma_{\mathrm{equil}} = 1048$ for the equilateral model. The linear relationship between the bispectra and f_{NL}, together with eqns. (8.28) and (8.29) then allows to write equation (5.1) as

$$\chi^2 = \frac{\left(f_{\mathrm{NL}}^M - \alpha_{TM} f_{\mathrm{NL}}^T\right)^2}{\sigma_M^2} + \frac{f_{\mathrm{NL}}^{T\,2}}{\sigma_T^2} - \frac{\alpha_{TM}^2 f_{\mathrm{NL}}^{T\,2}}{\sigma_M^2},\tag{8.30}$$

where the first term on the right hand side yields the normalized likelihood

$$\mathcal{L} = \frac{1}{\sqrt{2\pi\sigma_M^2}} \exp\left[-\frac{\left(f_{\mathrm{NL}}^M - \alpha_{TM} f_{\mathrm{NL}}^T\right)^2}{2\sigma_M^2}\right],\tag{8.31}$$

with the multiplicative bias

$$\alpha_{TM} = \sum_{\ell_{\min} \leq \ell_1 \leq \ell_2 \leq \ell_3 \leq \ell_{\max}} \frac{B_{\ell_1\ell_2\ell_3}^M B_{\ell_1\ell_2\ell_3}^M}{\mathrm{cov}(\ell_1,\ell_2,\ell_3)} \left(\sum_{\ell_{\min} \leq \ell_1 \leq \ell_2 \leq \ell_3 \leq \ell_{\max}} \frac{B_{\ell_1\ell_2\ell_3}^M B_{\ell_1\ell_2\ell_3}^T}{\mathrm{cov}(\ell_1,\ell_2,\ell_3)}\right)^{-1}.$$

Since the value $f_{\mathrm{NL}}^M = \alpha_{TM} f_{\mathrm{NL}}^T$ is ensuring a minimum in χ^2 (a maximum in the likelihood), the best fit (optimal) f_{NL} value of the assumed model to the true model is defined as $f_{\mathrm{NL}}^{\mathrm{opt}} \equiv \alpha_{TM} f_{\mathrm{NL}}^T$, which, applied to equation (8.30), yields

$$\chi^2\left(f_{\mathrm{NL}}^T\right) = f_{\mathrm{NL}}^{T\,2}\left(\frac{1}{\sigma_T^2} - \frac{\alpha_{TM}^2}{\sigma_M^{\,2}}\right). \tag{8.32}$$

This equation indicates a minimum value for the residual value of χ^2 which depends on f_{NL}^T. As expected, χ^2 vanishes if the two models coincide. The residual value can then be interpreted as an upper limit of the fit of the assumed to the true model. Hence, for small values of f_{NL}^T the deviation in χ^2 between true and assumed model is small as well, making model selection difficult.

8.6. Weak lensing tomography

A means of optimization of the information content from weak lensing studies is given by weak lensing tomography, where all the auto- and cross-power spectra that are constructed from source galaxies divided into redshift bins are employed to derive a signal. The spectra from different bins are given by (Hu 1999, Takada & Jain 2004)

$$C_\kappa^{(ij)}(\ell) = \int_0^{\chi_H} \frac{\mathrm{d}\chi}{\chi^2} W_{(i)}(\chi) W_{(j)}(\chi) P_\delta(k = \ell/\chi, a), \tag{8.33}$$

with

$$\tilde{C}_\kappa^{(ij)}(\ell) = C_\kappa^{(ij)}(\ell) + \delta_{ij} \frac{\sigma_\epsilon^2}{n_{(i)}}, \tag{8.34}$$

where the indices i and j denote the respective redshift bin and the Kronecker delta enforces shot noise only within the same bin (uncorrelated ellipticities between different redshift bins). The average number density of galaxies $n_{(i)}$ in redshift bin i is given by

$$n_{(i)} = \int_{\chi_{(i)}}^{\chi_{(i+1)}} \mathrm{d}\chi_s \, p_s(z) \frac{\mathrm{d}z}{\mathrm{d}\chi_s}, \tag{8.35}$$

and the weight function becomes

$$W_{(i)}(\chi) = \begin{cases} \frac{W_0}{n_{(i)}} a^{-1}(\chi)\chi \int_{\max\{\chi,\chi_{(i)}\}}^{\chi_{(i+1)}} \mathrm{d}\chi' n_{(i)}(z) \frac{\mathrm{d}z}{\mathrm{d}\chi'} \frac{\chi'-\chi}{\chi'}, & \chi \le \chi_{(i+1)} \\ 0 & , \quad \chi > \chi_{(i+1)}, \end{cases} \tag{8.36}$$

where $W_0 = 3/2\Omega_m(H_0/c)^2$.

In analogy, the bispectra are given by

$$B_\kappa^{(ijk)}(\boldsymbol{\ell}_1, \boldsymbol{\ell}_2, \boldsymbol{\ell}_3) = \int_0^{\chi_H} \frac{\mathrm{d}\chi}{\chi^4} W_{(i)}(\chi) W_{(j)}(\chi) W_{(k)}(\chi) B_\delta(\boldsymbol{k}_1/\chi, \boldsymbol{k}_2/\chi, \boldsymbol{k}_3/\chi, a), \tag{8.37}$$

which are unbiased estimators for symmetric ellipticity distributions with zero mean (Takada & Jain 2004):

$$\tilde{B}_\kappa^{(ijk)}(\boldsymbol{\ell}_1, \boldsymbol{\ell}_2, \boldsymbol{\ell}_3) \approx B_\kappa^{(ijk)}(\boldsymbol{\ell}_1, \boldsymbol{\ell}_2, \boldsymbol{\ell}_3). \tag{8.38}$$
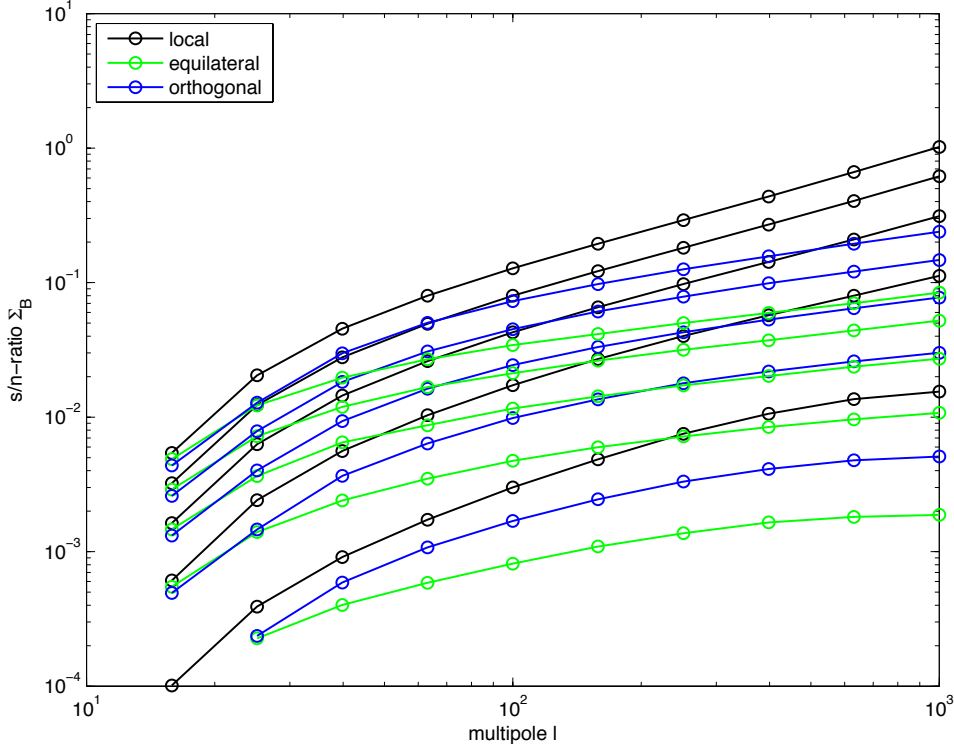
Figure 8.1.: Signal to noise ratios calculated for $f_{NL} = 1$ for weak lensing tomography with bin numbers from $n_{bin} = 1$ to $n_{bin} = 5$.

The bispectrum covariance is given by

$$\mathrm{cov}[B^{(abc)}_{\ell_1\ell_2\ell_3}, B^{(ijk)}_{\ell'_1\ell'_2\ell'_3}] \approx \Delta(\ell_1, \ell_2, \ell_3)\, \delta_{\ell_1\ell'_1}\delta_{\ell_2\ell'_2}\delta_{\ell_3\ell'_3}\, f^{-1}_{\mathrm{sky}}\, \tilde{C}^{(ai)}_\kappa\, \tilde{C}^{(bj)}_\kappa\, \tilde{C}^{(ck)}_\kappa, \tag{8.39}$$

which implies $B^{(112)}_\kappa = B^{(121)}_\kappa = B^{(211)}_\kappa$ etc.

For the tomography bispectra the Fisher matrix then reads

$$F = \sum_{\ell_{\min}\le\ell_1\le\ell_2\le\ell_3\le\ell_{\max}} \sum_{(i,j,k),(a,b,c)} \frac{\partial B^{(ijk)}_{\ell_1\ell_2\ell_3}}{\partial f_{\mathrm{NL}}} \left[\mathrm{cov}[B^{(abc)}_{\ell_1\ell_2\ell_3}, B^{(ijk)}_{\ell'_1\ell'_2\ell'_3}]\right]^{-1} \frac{\partial B^{(abc)}_{\ell_1\ell_2\ell_3}}{\partial f_{\mathrm{NL}}}. \tag{8.40}$$

Figure 8.1 shows the signal to noise ratio for $f_{NL} = 1$ as a function of ℓ_{max} and bin number n_{bin}. The corresponding Cramer-Rao bounds for $n_{bin} = 2$ and $\ell_{max} = 10^3$ yield $\sigma_{local} \approx 10$, $\sigma_{ortho} \approx 50$, and $\sigma_{equil} \approx 200$, as depicted in Table 8.1. Since these bounds do only comprise statistical limits, and no systematics, they represent ideal limits. Therefore, they will be used in the following instead of the even tighter bounds obtained by tomography with 5 redshift bins.

8.7. Frequentist statistics

Frequentist statistics focusses on the accuracy of the results as the leading measure. In terms of the parameters f_{NL}^T and f_{NL}^M, the frequentist measure of the likelihood can be expressed by the probability $p(f_{NL}^T \geq f_{NL}^{obs})$ referring to the likelihood of the value f_{NL}^M of a given model to be greater or equal than the observed value f_{NL}^{obs},

$$p(f_{NL}^M \geq f_{NL}^{obs}) = \int_{f_{NL}^{obs}}^{\infty} p(f_{NL}|M) \, df_{NL}, \tag{8.41}$$

and thus defines an estimate of the likelihood of obtaining more extreme fits. The null hypothesis is accepted with a significance level α (Lampton et al. 1976, Trotta 2007),

$$\alpha \leq 2 \, p\left(f_{NL}^M \geq f_{NL}^{obs}\right),$$

i.e. rejected with a confidence level of $1 - \alpha$. The probability function, $p(f_{NL}^M \geq f_{NL}^{obs})$, is derived from the likelihood described in Section 5.1. Due to the symmetry of the Gaussian distribution there is a factor of 2 for a two-tailed p-value statistics. In contrast to the Bayesian philosophy, p-value statistics is not taking into account the information content of data.

8.8. Bayesian statistics

One of the major problems in Bayesian model comparison is the choice of the prior, since it seems to be arbitrary and subjective. For theoretical considerations a wide prior volume is desirable, so that the posteriors are likelihood-driven. This would also allow for weakly conclusive data to have an impact on the posterior, whereas an experimental prior demands for significantly more conclusive data to show effect in the Bayesian analysis (Mukherjee et al. 2006). Nevertheless, the experimental prior is a compelling choice in view of the Bayesian philosophy of probability (Trotta 2007). Both approaches, though, are in line with the Bayesian spirit of data-driven likelihoods and converge for highly conclusive data. However, in case of comparatively small (e.g. experimental) priors, weakly conclusive data will only lead to prior driven likelihoods. A way to quantify the information content of new data is given by the Kullback-Leibler divergence, which relates the prior volume to the posterior volume. In order to compare the two choices, both a theoretically and experimentally motivated prior is employed. In the Bayesian sense, the likelihood $\mathcal{L} \equiv P(D|\theta, M)$ is the conditional probability of obtaining a set of data D, given a point θ, here $\theta = (f_{NL}^M, f_{NL}^T)$, in parameter space corresponding to the parameters of the assumed model M and underlying model T. In the calculations the data are given by the values of the underlying (true) model at the corresponding points in parameter space. Bayesian statistics is based on the principles of Bayes law,

$$P(\theta|M, D) = \frac{P(D|\theta, M)P(\theta|M)}{P(D|M)}, \tag{8.42}$$

where for model comparison the likelihood is marginalized over parameter space, resulting in the Bayesian evidence $E_M \equiv P(D|M)$ and corresponding to a likelihood-weighted prior probability,

$$E_M = \int d\theta \, P(D|\theta, M)P(\theta|M) = \int df_{NL}^M \, \mathcal{L} \pi(f_{NL}^M), \tag{8.43}$$

where $\pi(f_{\mathrm{NL}}^M) \equiv P(\theta|M)$. With the priors from Komatsu et al. (2011) with standard deviation π_M and mean $\hat{f}_{\mathrm{NL}}^M$ (Table 8.1), one can write the normalized Gaussian prior distribution as

$$\pi(f_{\mathrm{NL}}^M) = \frac{1}{\sqrt{2\pi\pi_M^2}} \exp\left[-\frac{\left(f_{\mathrm{NL}}^M - \hat{f}_{\mathrm{NL}}^M\right)^2}{2\pi_M^2}\right]. \tag{8.44}$$

This allows to compute the Bayes ratios B_{AB} for two given models A and B,

$$B_{AB} \equiv \frac{P(D|A)}{P(D|B)} = \frac{P(A)P(A|D)}{P(B)P(B|D)} = \frac{P(A)}{P(B)}\frac{E_A}{E_B}, \tag{8.45}$$

where the prior probabilities $P(A)$ and $P(B)$ assigned to the Models themselves are non-committal and taken to be equal (Trotta 2008). Both the likelihood and evidence are Gaussian. This allows to derive the analytical expression for the Bayes factor,

$$B_{AB,T} = \sqrt{\frac{\pi_B^2 + \sigma_B^2}{\pi_A^2 + \sigma_A^2}} \exp\left[-\frac{\left(\alpha_{TA}f_{\mathrm{NL}}^T - \hat{f}_{\mathrm{NL}}^A\right)^2}{2\left(\sigma_A^2 + \pi_A^2\right)} + \frac{\left(\alpha_{TB}f_{\mathrm{NL}}^T - \hat{f}_{\mathrm{NL}}^B\right)^2}{2\left(\sigma_B^2 + \pi_B^2\right)}\right],$$

with α_{TA} and α_{TB} representing the best fit f_{NL}-conversion factor to model T for model A and B, respectively. The case $B = T$ implies, of course, $\alpha_{TB} = \alpha_{TT} = 1$. The indexing $B_{AB,T}$, denotes the Bayes factor B_{AB} if the true model T is generating the bispectra. A measure for the information content of the data is given by

$$I \sim \ln\frac{\sigma_M}{\pi_M}. \tag{8.46}$$

The index values of M and T are 0 (local), 1 (orthogonal), and 2 (equilateral). In the following, the Bayes factors will be computed for all combinations of competing and fiducial (true) models. The Bayes factor B serves as a statistical measure for model selection. Obviously, a Bayes factor close to unity leads to an undecisive result.

8.9. Bayesian vs. frequentist inference

Given the fundamentally different nature of the frequentist p-value statistics the results are expected to be complementary to the Bayesian analysis. This is known as Lindley's paradox (Lindley 1957). For a systematic comparison the probabilities for all combinations of assumed models M and underlying (true) models T are calculated with priors according to Table 8.1.

Indeed, the expected differences between frequentist and Bayesian statistics can be observed in Fig. 8.2, which depicts p-values and Bayes factors for different combinations of the competing inflationary non-Gaussianity models. A fit of the orthogonal model to an underlying local non-Gaussianity is accepted by frequentist statistics with a p-value > 0.95 for $-26 < f_{\mathrm{NL}}^T < 26$. Bayesian inference, however, favors the local model in the range of $-50 < f_{\mathrm{NL}}^T < 50$ for the experimental prior and for all f_{NL}^T for the theoretical prior. If the orthogonal model is true, frequentist statistics yields a p-value > 95 per cent for the local model for $-148 < f_{\mathrm{NL}}^T < 148$, whereas Bayesian inference prefers the local model for the entire f_{NL}^T regime. For a true orthogonal model Bayesian inference is in favor of the local model with respect to the equilateral

Table 8.1.: Priors for the primordial non-Gaussianity models

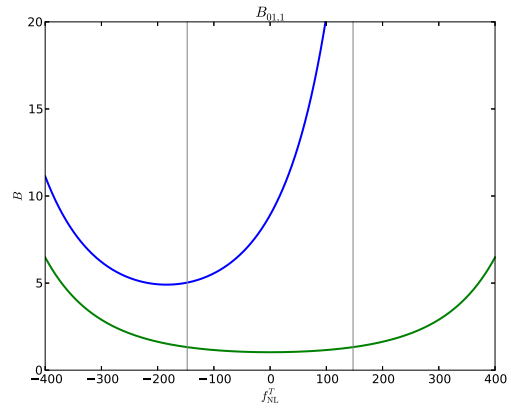| model	local	orthogonal	equilateral
Δf_{NL}	-10...74	-410...6	-214...266
$\hat{f}_{\mathrm{NL}}^{M}$	32	-202	26
π_M	21	104	120
σ_2	10	50	100

Prior parameter space for the different models as derived by Komatsu et al. (2011) from observations of the CMB bispectrum (WMAP) and constraints obtained by weak lensing tomography for 2 redshift bins. The table shows the 2σ confidence interval Δf_{NL} for each model, the corresponding mean $\hat{f}_{\mathrm{NL}}^{M}$, and standard deviation π_M of the resulting Gaussian prior distribution. σ denotes the Cramer-Rao bounds as obtained by calculations for weak lensing tomography with up to 5 redshift bins.

model for $-400 < f_{\mathrm{NL}}^{T} < 100$ for the experimental prior and for all f_{NL}^{T} for the theoretical prior. The comparatively large prior volume of the orthogonal with respect to the local model explains the Bayesian preference of the local model for most values of f_{NL}^{T}. A underlying local inflationary non-Gaussianity provides p-values > 0.95 for the equilateral model in the regime of $-22 < f_{\mathrm{NL}}^{T} < 22$. Bayesian inference favors the local model for $-10 < f_{\mathrm{NL}}^{T} < 100$ for the experimental prior and for all f_{NL}^{T} for the theoretical prior. An underlying equilateral model yields a p-value > 0.95 for the local model for $-204 < f_{\mathrm{NL}}^{T} < 204$. Bayesian inference favors the local model over the entire f_{NL}^{T} range. $p > 0.95$ for $-200 < f_{\mathrm{NL}}^{T} < 200$ for the orthogonal model when fitted to the equilateral model. For the experimental prior Bayes factors are in favor of the equilateral model for $-225 < f_{\mathrm{NL}}^{T} < 260$, whereas employing the theoretical prior yields preference for the orthogonal model for the entire f_{NL}^{T} range.

In order to provide an estimate of future weak lensing data the results are set in the context of an information space showing isocurves for the Bayes factors. Figure 8.4 shows the dependency of the values of the Bayes factors on the information content π_M/σ_M and π_T/σ_T of the data for the competing models M and T, where M denotes the assumed model and T the underlying true model. The red dot in this space denotes the position as obtained by the weak lensing calculations. In order to find an instructive representation of the $B_{MT,T}$ isocurves, it is assumed that α_{TM} is converging close to the values calculated for $\ell_{\max} = 3000$ (Figure 8.3). This allows the calculation of Bayes factor isocurves in a 2-dimensional information space. It should be mentioned, however, that this assumption is only a rough approximation since the covariance depends non-trivially on the redshift bin configuration. The two red points in Figure 8.4 depict the information content of conventional weak lensing and weak lensing tomography, respectively. It can be seen that weak lensing tomography clearly improves the information content of the signal, as indicated by the arrow pointing into the regime for informative data depicted by the box in the lower left corner. From the plots it can be concluded that only weak lensing tomography is provides the required precision for the applicability of Bayesian methods. The plots also allow to estimate the dominance of the local model for Bayesian inference. The Bayes factor isocurves
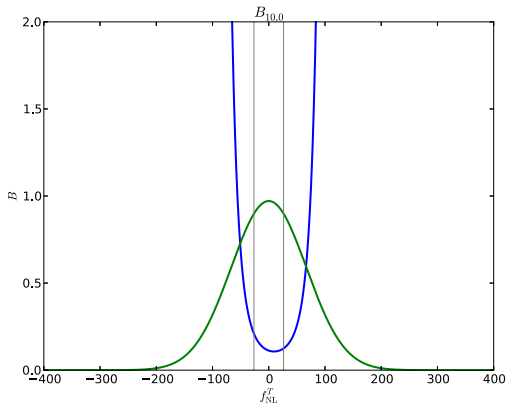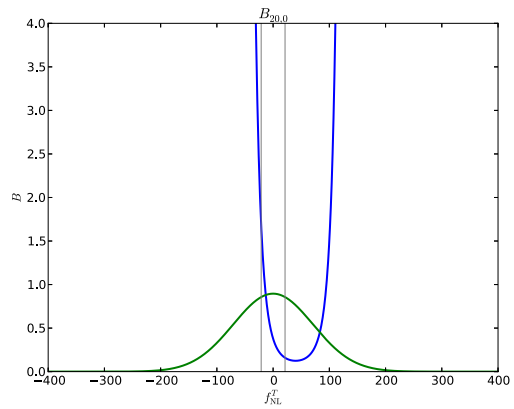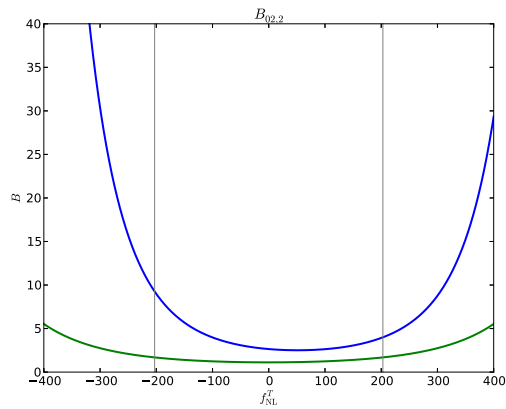
(a) T: local, M: orthogonal
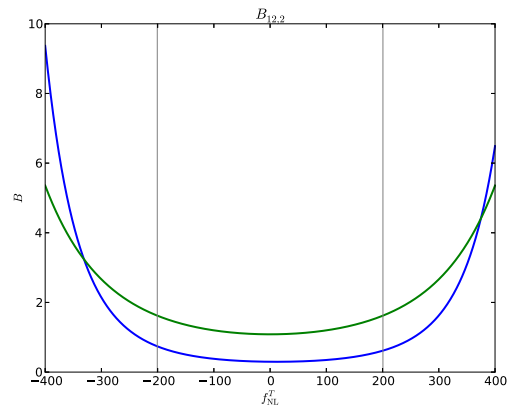
(b) T: orthogonal, M: local
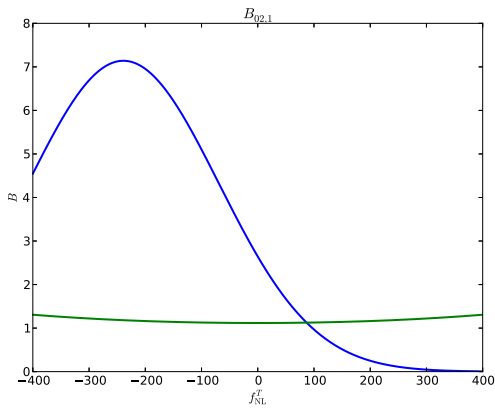
(c) T: orthogonal, M: local, equilateral

(d) T: local, M: equilateral

(e) T: equilateral, M: local

(f) T: equilateral, M: orthogonal

Figure 8.2.: Diagrams for the p-values (red line), with vertical grey lines indicating the 2σ confidence interval, and Bayes factors, with the experimental priors (blue line), and Bayes factors for theoretical priors (green line) as a function of the parameter value of f_{NL}^{T} of the underlying model.
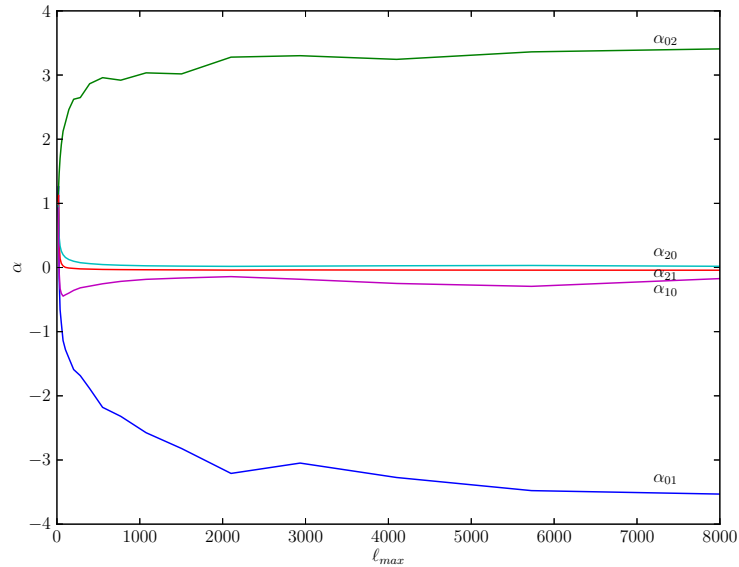
Figure 8.3.: Conversion factors α_{01}, α_{10}, α_{02}, α_{02}, and α_{21} for various values of $\ell_{\max}$.

indicate preference for $B_{10,0}$, $B_{01,1}$, and $B_{20,0}$ for future weak lensing surveys. Only for $B_{02,2}$, i.e. an underlying equilateral configuration and assumed local model, future data may favor the equilateral model. The large covariance of the equilateral model has its origin in the convention that all models are normalized such, that they show the same amplitudes for an equilateral configuration, thus leading to larger normalization factors for the local and orthogonal models. A method to avoid this bias can be achieved by a standardized normalization for f_{NL} based on the shape autocorrelator as proposed by Fergusson & Shellard (2009).

8.10. Summary

In this analysis the focus is on the comparison of Bayesian and frequentist methods with regard to inflationary non-Gaussianity models with three different bispectrum configurations (local, orthogonal, and equilateral), covering a wide range of bispectra. The methodology and statistical formalism employed in this work can be applied to all models with linear parameter dependence. The linearity of the models provides an instructive and general view on the differences between Bayesian and frequentist statistics. In this context, Lindley's paradox could be shown to apply. In order to obtain significant constraints on the respective models, weak lensing tomography has been applied and shown to be far superior to conventional weak lensing data. Only weak lensing tomography provides sufficiently informative signals in order to be employed in Bayesian inference. However, due to the normalization of f_{NL} there is a systematic bias for the local model from a Bayesian point of view arising from the comparatively large covariances of the orthogonal and equilateral models. These have their origin in the convention that all models
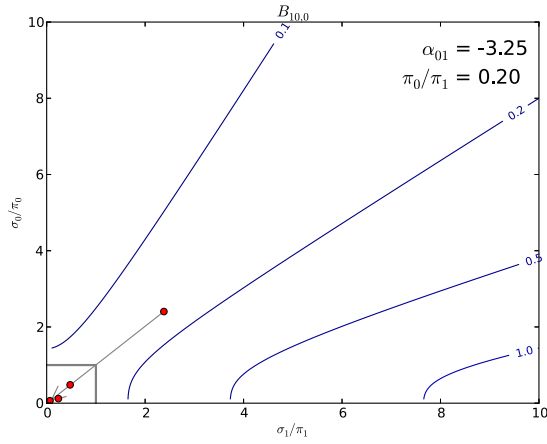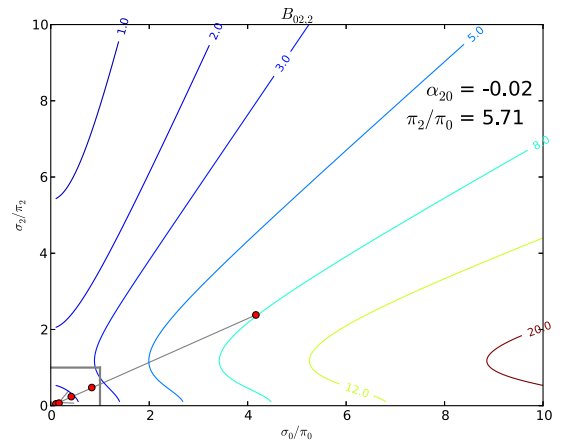
(a) true: local, assumed: orthogonal
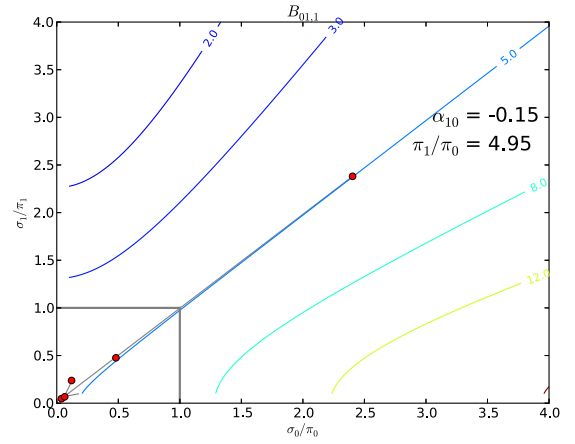
(b) true: orthogonal, assumed: local
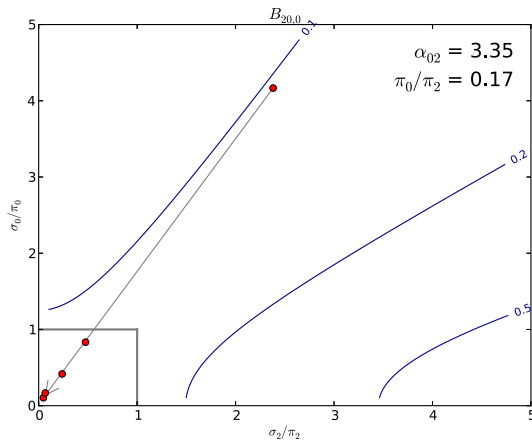
(c) true: local, assumed: equilateral

(d) true: equilateral, assumed: local

Figure 8.4.: Shown are the isocurves of the Bayes factors for the models local (0), orthogonal (1), and equilateral (2), in information space with the grey box in the lower left corner indicating the regime of informative data. The positions of the red dots refer to the respective non-tomographic and tomographic weak lensing data. The change in information content due to weak lensing tomography using 5 bins is illustrated by the grey connecting arrow. A converging value of α implies that the changes in σ due to more informative data would be proportional to each other, i.e. the data point is moving approximately on a line to the origin. (a) $B_{10,0}$ isocurves indicate preference for the local model also in case of more informative data, which is due to the comparatively small prior volume of the local model. (b) Even with more informative data the values of $B_{01,1} \approx 5$ favour the local model. (c) Values for $B_{20,0}$ clearly favour the local model. (d) Shown are the $B_{02,2}$ isocurves. The local model is favoured also with weak lensing tomography due to the large prior volume of the equilateral model.

are normalized such that they show the same amplitudes for an equilateral configuration, thus leading to larger normalization factors for the local and orthogonal models. Methods to avoid this bias by a standardized normalization for f_{NL}, which is based on the shape autocorrelator, have been proposed by Fergusson & Shellard (2009). Nevertheless, by the sensitivity of weak lensing on small scales and the technique of weak lensing tomography provide complementary constraints on inflationary non-Gaussianity models.

Systematic errors are negelected which, for instance, arise from uncertainties in the cosmological parameter set. Furthermore, other sources of non-Gaussianities are not considered, such as those arising from structure formation, which are shown to be separable (Schäfer et al. 2012) in case of a strong prior on the cosmological parameter or reduced complexity of the cosmological model (e.g., if the wCDM dark energy cosmology is replaced by the simpler ΛCDM cosmology). If the knowledge of the cosmology is not precise it is very difficult to assign a primordial origin to a residual bispectrum for the range of the relevant parameter regime. Another source of physical systematics originates from the influence of baryonic physics and intrinsic alignments on small scales, caused by correlations of galaxy ellipticities with the surrounding density field, leading to a contamination of the bispectral data at a 10 per cent level (Semboloni et al. 2008), which can be corrected for by accurate photometric redshifts, which also allow for weak lensing tomography. Systematics of statistical nature is introduced by the Gaussian approximation of the weak lensing covariance, which is justified in the range of multipole numbers considered in this work (Kaiser 1992, Takada & Jain 2004, Jeong et al. 2011). Furthermore, the Bayesian analysis given in this paper is prior-dominated due to the lack of highly conclusive weak lensing data. This is not surprising considering the strong Gaussianizing effect by virtue of the central limit theorem due to the line of sight integration (Jeong et al. 2011), making the weak lensing bispectra less sensitive to non-Gaussianities than CMB data. Nevertheless, weak lensing probes smaller scales than the CMB, hence complementing CMB observations and placing useful independent constraints on non-Gaussianities, in particular on smaller scales where CMB bounds might not apply (Schäfer et al. 2012). Furthermore, weak lensing maps the density field linearly and is thus less prone to systematics than other large-scale structure probes. Therefore an estimation of future data by more sophisticated methods such as weak lensing tomography was given in order to explore the full potential of weak lensing as a probe for non-Gaussian inflationary model comparison. Additionally, weak lensing tomography would help to correct for the systematics induced by Gaussianization and intrinsic alignments. Thus, the results serve rather as an estimate of the potential applicability of weak lensing data and study of the fundamental differences between the Bayesian and Frequentist philosophy.

The impact of future weak lensing surveys has been estimated. The analysis reveals that even for highly informative data the local model is preferred, except when compared to an underlying equilateral model. Further, Lindley's paradox can be observed, showing that a model favored by Bayesian statistics can be rejected by Frequentist statistics in the same regime of parameter space, for all combinations of models, demonstrating the fundamental differences between Frequentist and Bayesian philosophy. This class of models with linear parameter dependence allows to express the Bayes factors in an analytical form, making it possible to gain a more intuitive view on the mechanisms of model selection. This work demonstrates the dominance of the local model from a Bayesian point of view. Statistical effects, such as the suppression of non-Gaussianities by virtue of the central limit theorem, and the contamination of weak lensing bispectra by intrinsic alignments can be reduced by weak lensing tomography (Jeong et al.

2011, Semboloni et al. 2008). In this analysis, weak lensing tomography has been shown to be a powerful method for enhancing the information content of non-Gaussian signals.

Note

The Bayesian inference and statistical analysis described in this chapter is currently in preparation for publication.

9. Summary and outlook

Angular alignments of neighbouring galaxies, as predicted by tidal shear models, give rise to short-ranged non-zero angular momentum alignment correlations of neighbouring galaxies subject to similar tidal gravitational fields during their formation process. Ellipticity correlations between galaxies are correlated angular momenta of their host haloes in the context of quadratic alignment models allows to analyze these models by observations of galaxy ellipticity fields. Future surveys will be sensitive to scales similar to the predicted correlation length of intrinsic ellipticity alignments of ~ 1 Mpc/h, and thus allowing for observing and discerning intrinsic alignment models. At the same time intrinsic alignment will be a significant source of contaminations of future weak lensing data in the convergence spectrum. In Chapter 6 of this work the effect of intrinsic ellipcity correlations on the weak lensing convergence spectrum is contrasted to the commonly assumed case of intrinscally uncorrelated galaxy ellipticities. At low redshift intrinsic alignments dominate the galaxy ellipticity correlations and deflection is the major mechanism whereas for deep surveys such as EUCLID, weak lensing shear mainly determines the ellipticity correlations. Thus, the conclusion is drawn that for deep surveys intrinsic alignments are neglibible whereas they can become detectable for closeby galaxies. During their formation process galaxies do not only acquire angular momentum but also peculiar velocities through the local gravitational field. The displacements introduced by the peculiar galactic motions are comparable in scale to the correlation length of intrinsic alignments. Chapter 7 provides an analysis of the evolution of galaxy ellipticity correlations under the influence of peculiar galactic motions. Peculiar galactic velocities have been related to the gravitational potential by the Zeldovich approximation. The accumulated effect of the projected peculiar galactic motions has been derived in terms of an angular displacement potential in analogy to the weak gravitational lensing formalism. It could be shown that the effects peculiar motions and weak gravitational shear are comparable in magnitude, whereas the efficiency of weak lensing increases with redshift in contrast to the accumulated effect of the angular projection of peculiar motions.

Galaxy ellipticity fields display mathematical analogies to spin-2 tensor fields and have thus been described in the framework of the CMB polarization formalism in terms of basis-independent ellipticity E- and B-modes. The intrinsic ellipticity $E-$ and $B-$mode spectra have been derived from a given quadratic alignment model. The randomized galactic motions supress the ellipticity E- and B-mode power significantly at small angular scales by 10 and by 60 per cent, respectively. In comparison, the ellipticity correlations are altered by lensing by 5 per cent for the ellipticity E-modes and by 30 per cent for the B-modes. Furthermore, both the weak gravitational lensing of galaxy ellipticities and the effect of peculiar galactic motions break the homogeneity of the galaxy ellipticity field as indicated by the off-diagonality of the coupling kernels responsible for the mixing between $E-$ and B-modes. Correlations between adjacent multipoles at largest multipoles should be strongest and were estimated to be at most 10 per cent and proportional to ℓ for weak lensing. By comparing the mode coupling functions $W_+(\ell, \ell')$ and $W_-(\ell, \ell')$ for both peculiar motions and weak gravitational lensing, it can be inferred that convolution is a minor

effect with regard to the mixing of multipoles.

Another application of weak gravitational lensing statistics is given in Chapter 8, in which the fundamental fundamental differences between Bayesian and frequentist model selection are analyzed in the context of inflationary non-Gaussianity models with linear parameter dependence in f_{NL}. The linearity of this class of models provides analytical expressions for the statistical estimators representing the likelihood of the respective competing model. In the framework of Bayesian statistics the Bayes factor given by the ratio of the model evidences and prior probabilities, quantifies the preference for a given model compared to another competing model. Both prior and posterior determine the Bayesian result, providing a more comprehensive view on model probabilities but also imposing a problem if model selection becomes prior dominated. As a consequence of the specific normalization of the parameter f_{NL} with respect to the equilateral model, Bayesian model selection for the inflationary non-Gaussianity models as considered in this thesis is prior-driven due to the comparatively small prior volume of the local model. As a result the local non-Gaussianity model clearly dominates the equilateral and orthogonal non-Gaussianity models for most values of f_{NL}. Furthermore, non-tomographic weak gravitational lensing of galaxy ellipticities does not yield sufficiently informative data when applied to priors constrained by observations of the CMB, even though weak gravitational lensing provides complementary information on small scales with regard to CMB observations. Therefore an outlook to future tomographic weak lensing data is given by extrapolating the information content in information space resulting in the conclusion that even for weak lensing tomography it may prove difficult to extract more information in the framework of Bayesian model selection. Lindley's paradox has been shown to apply which reflects the fundamental differences between the Bayesian and frequentist view.

High precision observations such as EUCLID require a comprehensive understanding of potential physical processes influencing the statistics of observed galaxy ellipticities. In order to derive constraints on the cosmological parameter set or to analyze intrinsic angular alignments of galaxies these processes need to be quantified. Two significant effects of this kind have been described in Chapter 6 and 7. From this work, for the effect of peculiar motions it can be concluded that in principle the dispersing effect of peculiar motion suppresses intrinsic ellipticity correlations reducing the bias due to the assumption of intrinsically uncorrelated ellipticities in the analysis of weak lensing data. Changes in the spectra occur on scales where the shape noise is already dominating. With regard to the influence of intrinsic ellipticity correlations on weak lensing observations it could be shown that for deep surveys intrinsic alignments are subdominant in comparison to the correlations induced by gravitational shear. At low redshifts, however, intrinsic alignments dominate and the most important lensing effect is deflection. Bayesian model selection with respect to inflationary non-Gaussianities, however, imposes challenges on the applicability of weak gravitational lensing surveys, even for tomographic methods, as shown in Chapter 8. However, some of the implications on weak lensing statistics described in this thesis may be well be within the reach of future surveys.

Bibliography

Abramowitz M., Stegun I. A., 1972, Handbook of Mathematical Functions. Handbook of Mathematical Functions, New York: Dover, 1972

Abramowitz M. S. I. A., 1972, Handbook of Mathematical Functions.. New York: Dover

Ade P., et al., 2013

Albrecht A., Steinhardt P. J., 1982, Physical Review Letters, 48, 1220

Alishahiha M., Silverstein E., Tong D., 2004, Phys. Rev. D, 70, 123505

Andrae R., Jahnke K., 2011, MNRAS, p. 1665

Arfken G. B., Weber H. J., 2005, Materials and Manufacturing Processes

Arkani-Hamed N., Creminelli P., Mukohyama S., Zaldarriaga M., 2004, Journal of Cosmology and Astroparticle Physics, 2004, 001

Arroja F., Romano A. E., Sasaki M., 2011, Phys. Rev. D, 84, 123503

Bailin J., Kawata D., Gibson B. K., Steinmetz M., Navarro J. F., Brook C. B., Gill S. P. D., Ibata R. A., Knebe A., Lewis G. F., Okamoto T., 2005, ApJL, 627, L17

Bardeen J. M., 1980, Phys. Rev. D, 22, 1882

Bardeen J. M., Bond J. R., Kaiser N., Szalay A. S., 1986, ApJ, 304, 15

Bardeen J. M., Steinhardt P. J., Turner M. S., 1983, Phys. Rev. D, 28, 679

Bartelmann M., 2010, Classical and Quantum Gravity, 27, 233001

Bartelmann M., 2010, Classical and Quantum Gravity, 27, 233001

Bartelmann M., Schneider P., 2001, Physics Reports, 340, 291

Bartelmann M., Schneider P., 2001, Physics Reports, 340, 291

Bartolo N., Komatsu E., Matarrese S., Riotto A., 2004, Physics Reports, 402, 103

Bernardeau F., 1998, arXiv preprint astro-ph/9802243

Bernardeau F., Bonvin C., Vernizzi F., 2010, Phys. Rev. D, 81, 083002

Bernardeau F., Colombi S., Gaztañaga E., Scoccimarro R., 2002, Physics Reports, 367, 1

Bernstein G. M., 2009, ApJ, 695, 652

Blazek J., McQuinn M., Seljak U., 2011, Journal of Cosmology and Astroparticle Physics, 2011, 010

Bouchet F. R., Juszkiewicz R., Colombi S., Pellat R., 1992, ApJL, 394, L5

Bridle S., King L., 2007, New Journal of Physics, 9, 444

Buchert T., 1989, Astronomy and Astrophysics, 223, 9

Bullock J. S., Dekel A., Kolatt T. S., Kravtsov A. V., Klypin A. A., Porciani C., Primack J. R., 2001, ApJ, 555, 240

Capranico F., Merkel P., Schaefer B. M., 2012, ArXiv e-prints 1207.5939

Carbone C., Baccigalupi C., Bartelmann M., Matarrese S., Springel V., 2009, MNRAS, 396, 668

Carroll S. M., Press W. H., Turner E. L., 1992, ARA&A, 30, 499

Catelan P., 1995, MNRAS, 276, 115

Catelan P., Kamionkowski M., Blandford R. D., 2001, MNRAS, 320, L7

Catelan P., Lucchin F., Matarrese S., Moscardini L., 1995, MNRAS, 276, 39

Catelan P., Porciani C., 2001, MNRAS, 323, 713

Catelan P., Theuns T., 1996a, MNRAS, 282, 436

Catelan P., Theuns T., 1996b, MNRAS, 282, 455

Challinor A., Lewis A., 2005, Phys. Rev. D, 71, 103010

Chen X., 2012, Journal of Cosmology and Astroparticle Physics, 2012, 038

Chen X., Easther R., Lim E. A., 2007, Journal of Cosmology and Astroparticle Physics, 2007, 023

Chen X., Easther R., Lim E. A., 2008, Journal of Cosmology and Astroparticle Physics, 2008, 010

Chen X., xin Huang M., Kachru S., Shiu G., 2007, Journal of Cosmology and Astroparticle Physics, 2007, 002

Cheung C., Fitzpatrick A. L., Kaplan J., Senatore L., Creminelli P., 2008, Journal of High Energy Physics, 2008, 014

Codis S., Pichon C., Devriendt J., Slyz A., Pogosyan D., Dubois Y., Sousbie T., 2012, ArXiv e-prints 1201.5794

Coleman S., 1977, Physical Review D, 15, 2929

Cooray A., Hu W., 2002, ApJ, 574, 19

Crittenden R. G., Natarajan P., Pen U.-L., Theuns T., 2001, ApJ, 559, 552

Crittenden R. G., Natarajan P., Pen U.-L., Theuns T., 2002, ApJ, 568, 20

Croft R. A. C., Metzler C. A., 2000, ApJ, 545, 561

Dodelson S., Zhang P., 2005, Phys. Rev. D, 72, 083001

Doroshkevich A. G., 1970, Astrofizika, 6, 581

Durrer R., 2008, The Cosmic Microwave Background

Fergusson J. R., Shellard E. P. S., 2009, Physical Review D, 80, 043510

Friedmann A., 1922, Z. Phys., 10, 377

Friedmann A., 1924, Z. Phys., 32, 326

Fu L., Kilbinger M., 2010, MNRAS, 401, 1264

Giahi A., Schäfer B. M., 2012, Monthly Notices of the Royal Astronomical Society, 428, 1312

Giahi-Saravani A., Schaefer B. M., 2013, arXiv preprint arXiv:1302.2607

Guth A. H., 1981, Physical Review D, 23, 347

Hahn O., Carollo C. M., Porciani C., Dekel A., 2007, MNRAS, 381, 41

Hahn O., Porciani C., Carollo C. M., Dekel A., 2007, MNRAS, 375, 489

Hahn T., 2005, Computer Physics Communications, 168, 78

Hamana T., Bartelmann M., Yoshida N., Pfrommer C., 2005, MNRAS, 356, 829

Heavens A., Refregier A., Heymans C., 2000, MNRAS, 319, 649

Heymans C., Brown M., Heavens A., Meisenheimer K., Taylor A., Wolf C., 2004, MNRAS, 347, 895

Heymans C., Heavens A., 2003, MNRAS, 339, 711

Heymans C., White M., Heavens A., Vale C., van Waerbeke L., 2006, MNRAS, 371, 750

Hirata C. M., Mandelbaum R., Ishak M., Seljak U., Nichol R., Pimbblet K. A., Ross N. P., Wake D., 2007, MNRAS, 381, 1197

Hirata C. M., Seljak U., 2004, Phys. Rev. D, 70, 063526

Hoyle F., 1949, MNRAS, 109, 365

Hu W., 1999, The Astrophysical Journal Letters, 522, L21

Hu W., 2000, Phys. Rev. D, 62, 43007

Hu W., 2001, The Astrophysical Journal Letters, 557, L79

Hu W., Okamoto T., 2002, The Astrophysical Journal, 574, 566

Hu W., White M., 2001, ApJ, 554, 67

Jeffreys H., 1998, Theory of Probability. International series of monographs on physics, Oxford University Press, USA

Jeong D., Schmidt F., Sefusatti E., 2011, Physical Review D, 83, 123005

Joachimi B., Bridle S. L., 2010, A&A, 523, A1

Joachimi B., Mandelbaum R., Abdalla F. B., Bridle S. L., 2011, A&A, 527, A26

Joachimi B., Schneider P., 2008, ArXiv e-prints 0804.2292, 804

Joachimi B., Schneider P., 2010, A&A, 517, A4

Kaiser N., 1992, ApJ, 388, 272

Kaiser N., 1992, ApJ, 388, 272

King L., Schneider P., 2002, A&A, 396, 411

King L. J., 2005, A&A, 441, 47

King L. J., Schneider P., 2003, A&A, 398, 23

Kirk D., Bridle S., Schneider M., 2010, MNRAS, 408, 1502

Kirk D., Laszlo I., Bridle S., Bean R., 2013, Monthly Notices of the Royal Astronomical Society

Kirk D., Rassat A., Host O., Bridle S., 2012, MNRAS, 424, 1647

Kitching T. D., Taylor A. N., 2011, MNRAS, 410, 1677

Komatsu E., 2010, Classical and Quantum Gravity, 27, 124010

Komatsu E., Smith K. M., Dunkley J., Bennett C. L., Gold B., Hinshaw G., Jarosik N., Larson D., Nolta M. R., Page L., Spergel D. N., Halpern M., Hill R. S., Kogut A., Limon M., Meyer S. S., Odegard N., Tucker G. S., Weiland J. L., Wollack E., Wright E. L., 2011, The Astrophysical Journal Supplement Series, 192, 18

Krause E., Hirata C., 2010, Astronomy & Astrophysics, 523

Lampton M., Margon B., Bowyer S., 1976, ApJ, 208, 177

Landau L. D., Lifshitz E. M., 1975, The classical theory of fields. Course of theoretical physics - Pergamon International Library of Science, Technology, Engineering and Social Studies, Oxford: Pergamon Press, 1975, 4th rev.engl.ed.

Lee J., Pen U., 2000, ApJL, 532, L5

Lee J., Pen U.-L., 2001, ApJ, 555, 106

Lee J., Pen U.-L., 2002, ApJL, 567, L111

Lee J., Pen U.-L., 2007, ApJL, 670, L1

Lee J., Pen U.-L., 2008, ApJ, 681, 798

Lee J., Springel V., Pen U.-L., Lemson G., 2007, ArXiv 0709.1106, 709

Lewis A., Challinor A., 2006, Physics Reports, 429, 1

Li M., Wang T., Wang Y., 2008, Journal of Cosmology and Astroparticle Physics, 2008, 028

Limber D., 1954, ApJ, 119, 655

Linde A. D., 1982, Physics Letters B, 108, 389

Linder E., Jenkins A., 2003, MNRAS, 346, 573

Mackey J., White M., Kamionkowski M., 2002, MNRAS, 332, 788

Mandelbaum R., Blake C., Bridle S., Abdalla F. B., Brough S., Colless M., Couch W., Croom S., Davis T., Drinkwater M. J., et al., 2011, Monthly Notices of the Royal Astronomical Society, 410, 844

Mandelbaum R., Hirata C. M., Ishak M., Seljak U., Brinkmann J., 2006, MNRAS, 367, 611

Melott A. L., Buchert T., Weiß A. G., 1994, arXiv preprint astro-ph/9404018

Merkel P. M., Schäfer B. M., 2011, MNRAS, 411, 1067

Miralda-Escude J., 1991, ApJ, 380, 1

Moutarde F., Alimi J.-M., Bouchet F. R., Pellat R., Ramani A., 1991, ApJ, 382, 377

Mukherjee P., Parkinson D., Corasaniti P. S., Liddle A. R., Kunz M., 2006, MNRAS, 369, 1725

Munshi D., Coles P., Kilbinger M., 2011, ArXiv e-prints

Natarajan P., Crittenden R. G., Pen U.-L., Theuns T., 2001, Publications of the Astronomical Society of Australia, 18, 198

Okumura T., Jing Y. P., 2009, ApJL, 694, L83

Parkinson D., Mukherjee P., Liddle A. R., 2006, Phys. Rev. D, 73, 123523

Peebles P. J. E., 1969, ApJ, 155, 393

Pen U.-L., Lee J., Seljak U., 2000, ApJL, 543, L107

Porciani C., Dekel A., Hoffman Y., 2002a, MNRAS, 332, 325

Porciani C., Dekel A., Hoffman Y., 2002b, MNRAS, 332, 339

Schäfer B. M., 2009, International Journal of Modern Physics D, 18, 173

Schäfer B. M., Grassi A., Gerstenlauer M., Byrnes C. T., 2012, MNRAS, 421, 797

Schäfer B. M., Merkel P. M., 2012, MNRAS, 421, 2751

Schäfer B. M., Merkel P. M., 2012, MNRAS

Schneider M. D., Bridle S., 2010, MNRAS, 402, 2127

Schneider P., Kilbinger M., 2007, A&A, 462, 841

Schneider P., van Waerbeke L., Jain B., Kruse G., 1998, MNRAS, 296, 873

Schneider P., van Waerbeke L., Mellier Y., 2002, A&A, 389, 729

Sciama D. W., 1955, MNRAS, 115, 2

Seery D., Lidsey J. E., 2005, Journal of Cosmology and Astroparticle Physics, 2005, 011

Seljak U., 1996a, ApJ, 463, 1

Seljak U., 1996b, ApJ, 460, 549

Semboloni E., Heymans C., van Waerbeke L., Schneider P., 2008, MNRAS, 388, 991

Semboloni E., Heymans C., van Waerbeke L., Schneider P., 2008, ArXiv 0802.3978, 802

Senatore L., Smith K. M., Zaldarriaga M., 2010, Journal of Cosmology and Astroparticle Physics, 2010, 028

Shapiro C., Cooray A., 2006, Journal of Cosmology and Astro-Particle Physics, 3, 7

Silverstein E., Tong D., 2004, Phys. Rev. D, 70, 103505

Smith R. E., Peacock J. A., Jenkins A., White S. D. M., Frenk C. S., Pearce F. R., Thomas P. A., Efstathiou G., Couchman H. M. P., 2003, MNRAS, 341, 1311

Smoot G. F., 1999, in Maiani L., Melchiorri F., Vittorio N., eds, 3K cosmology Vol. 476 of American Institute of Physics Conference Series, COBE observations and results. pp 1–10

Sugiyama N., 1995, ApJ Supplement, 100, 281

Takada M., Jain B., 2003a, MNRAS, 340, 580

Takada M., Jain B., 2003b, MNRAS, 344, 857

Takada M., Jain B., 2004, MNRAS, 348, 897

Trotta R., 2007, MNRAS, 378, 72

Trotta R., 2008, Contemporary Physics, 49, 71

Turner M. S., White M., 1997, Phys. Rev. D, 56, R4439

Wang L., Steinhardt P., 1998, ApJ, 508, 483

White S. D. M., 1984, ApJ, 286, 38

Zel'Dovich Y. B., 1970, A&A, 5, 84

Zhang P., 2010, ApJ, 720, 1090

Acknowledgements

Publications

1. A. Giahi and B.M. Schäfer:
   Evolution of intrinsic ellipticity correlations due to peculiar motion
   Monthly Notices of the Royal Astronomical Society 428.2 (2012): 1312-1320.

2. A. Giahi-Saravani and B.M. Schäfer:
   Weak gravitational lensing of intrinsically aligned galaxies.
   preprint arXiv:1302.2607 (2013) submitted to MNRAS

3. A. Giahi and B.M. Schäfer:
   Signatures of inflationary non-Gaussianities in weak lensing bispectra from a Bayesian
   perspective:
   in preparation

Curriculum Vitae

personal data

name: Aram Giahi Saravani

sex: male

birth: 18.12.1980 in Gronau (Westf.), Germany

nationality: German citizenship

marital status: unwed

address: Alter Postweg 147, 48599 Gronau, Germany

education

Eilermark Grundschule (1986 - 1990)

Werner-von-Siemens-Gymnasium Gronau (1991 - 2000)

Abitur at Werner-von-Siemens Gymnasium (26.5.2000)

academic record

study of physics at Universität Osnabrück (2001-2003), Universität Göttingen (2004-2007)

Vordiplom in physics, Universität Osnabrück (July 2003)

diploma thesis at Institut für Röntgenphysik, Göttingen/Germany (2006 - 2007)

Diplom in physics, Universität Göttingen (8.11.2006)

research Assistant at the Max-Planck-Institute for Biophysical Chemistry, Göttingen (2007-2008)

guest at the Institute of Astronomy, University of Cambridge (PhD offer) (October 2008-December 2008)

stay at Imperial College London (October 2009 - May 2009)

PhD student at Centre for Astronomy, University of Heidelberg (Sep.2009 - 2013)